

AD \_\_\_\_\_

Award Number:

**W81XWH-07-1-0629**

TITLE:

**Nanoparticle Contrast Agents for Enhanced Microwave Imaging and Thermal Treatment of Breast Cancer**

PRINCIPAL INVESTIGATOR:

**PI: Xu Li, PhD; Co-I: Alan V. Sahakian, PhD; Co-I: P. Messersmith, PhD; Co-PI: Susan C. Hagness, PhD; Co-I: John H. Booske, PhD; Co-I: Irena Knezevic, PhD.**

CONTRACTING ORGANIZATION:

**Northwestern University  
Evanston, IL 60208**

REPORT DATE:

**October 2010**

TYPE OF REPORT:

**Final**

PREPARED FOR: U.S. Army Medical Research and Materiel Command  
Fort Detrick, Maryland 21702-5012

DISTRIBUTION STATEMENT:

**x** Approved for public release; distribution unlimited

The views, opinions and/or findings contained in this report are those of the author(s) and should not be construed as an official Department of the Army position, policy or decision unless so designated by other documentation.

REPORT DOCUMENTATION PAGE			Form Approved OMB No. 0704-0188		
Public reporting burden for this collection of information is estimated to average 1 hour per response, including the time for reviewing instructions, searching existing data sources, gathering and maintaining the data needed, and completing and reviewing this collection of information. Send comments regarding this burden estimate or any other aspect of this collection of information, including suggestions for reducing this burden to Department of Defense, Washington Headquarters Services, Directorate for Information Operations and Reports (0704-0188), 1215 Jefferson Davis Highway, Suite 1204, Arlington, VA 22202-4302. Respondents should be aware that notwithstanding any other provision of law, no person shall be subject to any penalty for failing to comply with a collection of information if it does not display a currently valid OMB control number. <b>PLEASE DO NOT RETURN YOUR FORM TO THE ABOVE ADDRESS.</b>					
1. REPORT DATE (DD-MM-YYYY) 01-10-2010		2. REPORT TYPE Final		3. DATES COVERED (From - To) 15 Sep 2007 - 14 Sep 2010	
4. TITLE AND SUBTITLE Nanoparticle Contrast Agents for Enhanced Microwave Imaging and Thermal Treatment of Breast Cancer			5a. CONTRACT NUMBER		
			5b. GRANT NUMBER W81XWH-07-1-0629		
			5c. PROGRAM ELEMENT NUMBER		
6. AUTHOR(S) X. Li, A. Sahakian, P. Messersmith (Northwestern Univ.)  S. Hagness, J. Booske, I. Knezevic (University of Wisconsin-Madison)			5d. PROJECT NUMBER		
			5e. TASK NUMBER		
			5f. WORK UNIT NUMBER		
7. PERFORMING ORGANIZATION NAME(S) AND ADDRESS(ES)  Northwestern University  Evanston, IL 60208-1110			8. PERFORMING ORGANIZATION REPORT NUMBER		
9. SPONSORING / MONITORING AGENCY NAME(S) AND ADDRESS(ES) US Army Medical Research And Materiel Command  Fort Detrick, MD 21702-5014			10. SPONSOR/MONITOR'S ACRONYM(S)		
			11. SPONSOR/MONITOR'S REPORT NUMBER(S)		
12. DISTRIBUTION / AVAILABILITY STATEMENT  Approved for public release, distribution unlimited.					
13. SUPPLEMENTARY NOTES					
14. ABSTRACT The goal of this project was to investigate the microwave-frequency response of microparticle and nanoparticle contrast agents for the purpose of enhancing the sensitivity of microwave detection of breast cancer. We experimentally characterized the effective electromagnetic properties of a variety of micro/nanoparticle dispersions at microwave frequencies, developed theoretical and numerical tools to model microwave interactions with micro/nanoparticles, and conducted experimental investigations of the microwave scattering and absorption properties of the contrast agents in tissue-mimicking phantoms. We demonstrated that microbubbles and single-wall carbon nanotubes induce significant changes in the effective dielectric properties, heating efficiency, and thermoacoustic response of mixtures containing either of those particles. To the best of our knowledge, these accomplishments represent the first experimental laboratory demonstrations of contrast enhancement in a context relevant to microwave breast cancer detection.					
15. SUBJECT TERMS breast cancer, microwave imaging, contrast agents, nanoparticles, microbubbles, single-walled carbon nanotubes					
16. SECURITY CLASSIFICATION OF:			17. LIMITATION OF ABSTRACT  UU	18. NUMBER OF PAGES  65	19a. NAME OF RESPONSIBLE PERSON USAMRMC
a. REPORT U	b. ABSTRACT U	c. THIS PAGE U			19b. TELEPHONE NUMBER (include area code)

## Table of Contents

	<u>Page</u>
Introduction.....	4
Body.....	4
Key Research Accomplishments.....	14
Reportable Outcomes.....	16
Conclusion.....	18
References.....	19
Appendices.....	21

## Introduction

The expected long-term outcome of this research is the enhancement of microwave breast cancer detection sensitivity through the use of extrinsic contrast mechanisms, namely biocompatible micro- or nano-particles systemically delivered to the site of a malignancy via passive or active means. Such particles may impact the malignant-to-normal contrast of breast tissue at microwave frequencies, thereby altering the microwave scattering, absorption, and thermoacoustic response of breast tumors and enhancing the overall efficacy of microwave breast cancer detection. The goal of this project was to conduct a series of experimental and numerical investigations to elucidate and optimize the microwave-frequency response of microparticle and nanoparticle contrast agents. The specific aims were as follows: (1) Experimentally characterize the effective electromagnetic properties of a variety of micro/nanoparticle dispersions at microwave frequencies; (2) Develop theoretical/numerical tools to model microwave interactions with micro/nanoparticles and utilize these tools to design micro/nanoparticles that optimize the microwave contrast of malignant breast tumors; and (3) Conduct experimental investigations of the microwave scattering and absorption properties of the micro/nanoparticle contrast agents in tissue-mimicking phantoms. These three aims were addressed as three major tasks described below. The discussion below refers to results in published papers and abstracts included in the Appendices. Any figure that is available in an appendix is not duplicated in the body of this report.

## Body

**Task 1.** Experimentally characterize the effective electromagnetic properties of a variety of micro/nanoparticle dispersions at microwave frequencies.

*Task 1.1.* Our studies focused on the subset of candidate micro- and nano-particles that are the most promising for altering the scattering and absorption of microwave energy by a malignant lesion. Namely, we have investigated air-filled microbubbles, metallic nanoparticles, and carbon nanotubes. The goal of the experimental studies of Task 1 was to characterize the extent to which the dielectric properties of particles-in-liquid mixtures differed from that of the background liquid alone, without the particles. Since there was no biocompatibility requirement for these laboratory studies, we had some flexibility in choosing the tissue-mimicking background liquid. The liquid dispersions that we acquired or created involved either ethylene glycol (EG) or water as the background liquid. These were chosen as inexpensive, readily available reference liquids with well characterized dielectric properties at microwave frequencies.

- *Microbubbles:* We acquired air-filled, glass spheres from 3M (iM30K, average diameter of 18 microns) and dispersed them in EG to create mixtures of various concentrations.
- *Metallic nanoparticles:* We acquired monodispersions of metallic nanoparticles from a) Meliorum (copper nanoparticles dispersed in EG, with an average diameter of 384 nm and an overall volume fraction of 30%) and b) the Messersmith laboratory at Northwestern University (spherical and rod-shaped gold nanoparticles synthesized using an aqueous seeded growth method and coated with CTAB surfactant, with an average diameter of 20 nm and in concentrations ranging from 0.1 to 20 mM).

- Carbon nanotubes:** We acquired monodispersions of single-walled carbon nanotubes (SWCNTs) dispersed in aqueous solutions of 1% Pluronic (F127) surfactant from Prof. Balaji Sitharaman in the Department of Biomedical Engineering at Stony Brook University. We also acquired SWCNTs synthesized by commercial HiPCO (Unidym) and functionalized with a biocompatible and stable surfactant (polyethylene-glycol(PEG)-ylated phospholipids (PL)).

*Task 1.2.* Prior to characterizing the dielectric properties of the micro/nanoparticle dispersions and the corresponding particle-free liquids, we conducted microwave-frequency measurements of the dielectric properties of well-known homogeneous reference liquids (without particles) as a validation step. We performed the measurements using two complementary techniques: a wideband (0.5-20 GHz) open-ended coaxial probe technique that we previously perfected and used in a large-scale study of breast tissue [1-4], and a narrowband cavity perturbation technique [5] conducted at 2.2, 5.05, and 8 GHz. Figure 1 shows a comparison of the measured dielectric properties of water, methanol, ethanol, and EG obtained using these two characterization techniques. The excellent agreement observed between the narrowband and wideband results, as well as the agreement with reported values in the literature, validates our approach and illustrates the consistency check offered by the two complementary techniques.

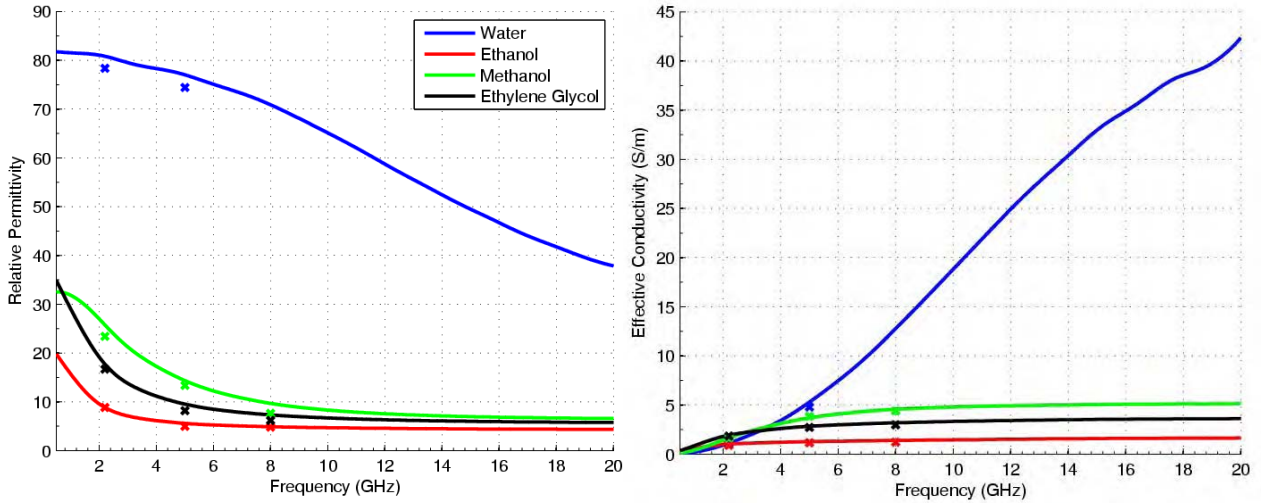


Figure 1. Dielectric properties (relative permittivity, left, and effective conductivity, right) of four reference liquids measured using a wideband technique (solid lines) and a narrowband technique (data markers).

*Task 1.3.* We used the wideband and narrowband microwave-frequency measurement techniques described above to characterize the effective dielectric properties of the three classes of micro/nanoparticle dispersions. We also analyzed the measured data to assess changes in the electromagnetic properties of the dispersion liquid due to the presence of the micro/nanoparticles. A summary of our findings from this task is provided below; further details about the experimental studies are provided in Appendices A and E.

*Task 1.3a: Microbubbles.* The reprint provided in Appendix A (Figure 2 therein) reports the relative permittivity and effective conductivity of pure EG (Solution 1) and four different

microbubble-EG dispersions (Solutions 2-5). The microbubble concentrations, ranging from 20% (Solution 2) up to 40% by weight (Solution 5), are within the typical  $10^9$  microbubbles/mL dosage administered in human ultrasound procedures [6]. We found that the dielectric properties decrease with increasing microbubble concentration, as expected. In particular, the relative permittivity and effective conductivity at 3 GHz of the highest-concentration dispersion decreased by factors of approximately two and three, respectively. Thus, the measured change in dielectric properties is significant for clinically relevant concentrations.

*Task 1.3b: Metallic nanoparticles.* Figure 2 below shows the relative permittivity and effective conductivity of the commercial dispersion consisting of a 30% volume fraction of the copper nanoparticles in EG. We found reasonable agreement between the wideband (solid and dotted lines) and narrowband measurements (symbols). For both the probe and cavity measurements above 2 GHz, the relative permittivity (dielectric constant) of the dispersion is approximately 20% higher than that of pure EG. However, we observed no significant change in the conductivity due to the presence of the nanoparticles. We also characterized the dielectric properties of the Northwestern University samples of gold nanoparticles in an aqueous solution and found no statistically significant change relative to the particle-free background medium. These negative findings motivated our investigation of SWCNTs as high-aspect-ratio alternative particles to compact metallic nanoparticles, as discussed further below.

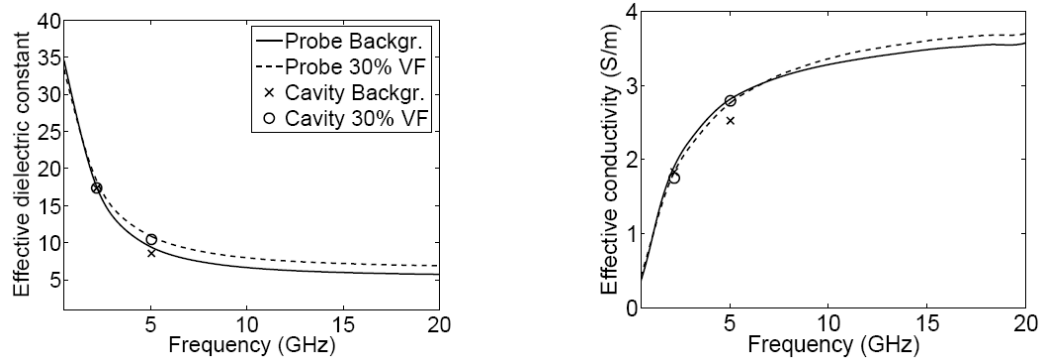


Figure 2. Dielectric properties of a commercially prepared dispersion of 384-nm copper particles in EG (30% volume fraction) compared with those of pure EG (the background medium). The measurements were conducted using both a wideband open-ended coaxial probe technique ("Probe") and a narrowband cavity perturbation technique ("Cavity").

*Task 1.3c: SWCNTs.* We characterized the dielectric properties of the Stony Brook CNTs dispersed in Pluronic and water. First, we compared the properties of monodispersions consisting of two concentrations (0.5 and 1.0 mg/mL) of 0.5-micron-long single-walled CNTs with the properties of the pure aqueous background. We found that the relative permittivity and effective conductivity of the CNT mixtures are significantly higher than the background medium. Second, we compared the properties of monodispersions consisting of two concentrations (0.5 and 1.0 mg/mL) of buckyballs with the properties of the pure aqueous background. In contrast to the large change observed with the CNTs, we found that the buckyballs did not change the effective properties of the medium. This finding is consistent with our measurement results for the metallic nanoparticles, which are similar to the buckyballs in that they are compact in shape with small aspect ratios. Thus our results indicate that for relatively small volume fractions of

nanoparticles, large aspect ratios are required in the metallic or semi-metal particles in order to significantly alter the macroscopic effective dielectric properties of the medium.

We also characterized the dielectric properties of dispersions created from the biocompatible (PL-PEG) functionalized SWCNTs in water (see Appendix E). Key results of this study are summarized in Figure 3. For a concentration of 2 mg/mL of SWCNTs, we observed at 1 GHz an increase in relative permittivity of approximately 10% and an increase in effective conductivity of approximately 90% relative to the properties of PL-PEG-water only (no SWCNTs).

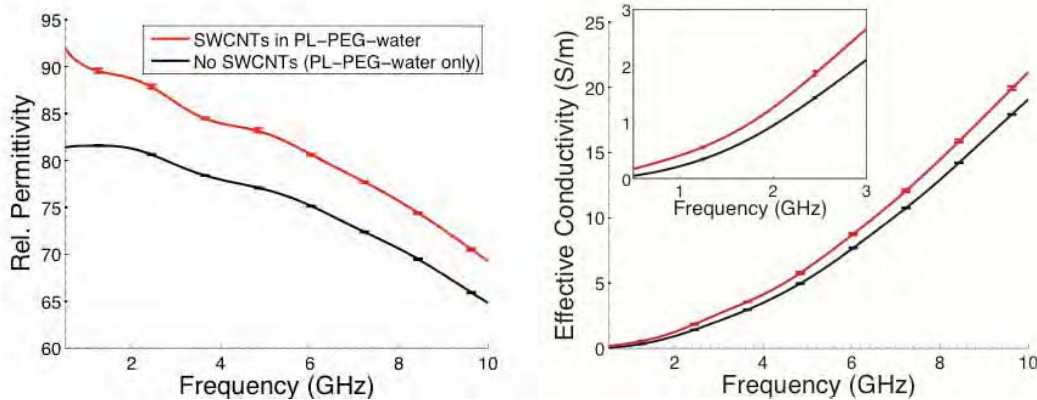


Figure 3. Frequency-dependent relative permittivity and effective conductivity of a mixture of water and phospholipid (PL)-polyethylene-glycol (PEG) with and without SWCNTs at a concentration of 2 mg/mL. The measurements were conducted using a precision open-ended coaxial probe technique.

**Task 2.** Develop theoretical/numerical tools to model microwave interactions with micro/nanoparticles and utilize these tools to design micro/nanoparticles that optimize the microwave contrast of malignant breast tumors.

*Task 2.1.* We adapted two types of 2D classical electromagnetic simulation tools and conducted a comprehensive theoretical investigation of the effects of moderate volume fractions of a variety of micro/nanoparticles on the effective electromagnetic properties of binary mixtures with a background medium representative of malignant breast tissue. Since 2D simulations require only a fraction of the computational resources of 3D simulations, we used 2D methods to perform a large number (1000's) of simulations with systematically varying particle sizes and randomized particle distributions. One of the 2D simulation tools was based on a full-wave technique for solving Maxwell's equations of electrodynamics, namely the finite-difference time-domain (FDTD) method, while the other tool was based on a quasi-static finite-element method (QS-FEM). The computational burden of the latter technique is lower, but its accuracy is limited in the case of lossy particles as it does not account for physical size effects such as skin depth.

We focused on lossless air-filled microbubbles and conducting metallic spheres as the candidate contrast agent particles in this study. We modeled particles that ranged in size from 500 nm to 200 microns. We expect clinically relevant microbubble contrast agents to be 1-7 microns in diameter, and metallic spheres to range in size from 200 to 250 nm. While the smallest metallic particles considered in this numerical study exceed the predicted size range for practical applications, we limited the scope of this 2D classical electromagnetics study to a size regime that poses the least uncertainty about the physical properties of the metallic particles.

Furthermore, we chose the largest particle size to be approximately an order of magnitude larger than the skin depth at microwave frequencies in order to investigate the effects of inclusion size on the effective dielectric properties of the mixture. For both the QS-FEM and FDTD simulations, we considered 5%, 10%, and 20% volume fractions, which we estimate to be reasonable for clinical applications. For each volume fraction, we simulated 100 spatial arrangements of particles and computed ensemble averages of the effective dielectric properties. We summarize our findings below; further details about the 2D numerical studies of microbubbles and metallic nanoparticle dispersions are provided in Appendix D.

We found excellent agreement between the QS-FEM-computed and FDTD-computed effective dielectric properties of mixtures containing microbubbles, as expected for the case of lossless particles where the simplifying assumptions of the QS-FEM are valid. We also found excellent agreement between the numerical results obtained here for the microbubbles and the experimental results obtained under Task 1.3 that suggested that small-to-moderate volume fractions of microbubbles can substantially lower the effective dielectric properties of the mixture.

For the metallic particle simulations, we found great discrepancies between the QS-FEM and FDTD values, and considered this to be evidence that the quasi-static assumption was breaking down for the lossy particles. Therefore we relied upon the FDTD predictions for analyzing the effects of the metallic particles. We investigated the effect of particle spatial distribution (e.g. contacting versus non-contacting) and particle size on the effective dielectric properties of the mixtures. We found that contacting lossy particles lead to a larger increase in the effective properties than non-contacting inclusions. We observed an interesting size-dependent trend in the effective properties as the inclusion diameter increased from one-tenth to ten times the skin depth at the microwave frequency assumed in the simulations (5 GHz). Specifically, we found that when the inclusion size is approximately one to ten times the skin depth, the relative permittivity of the mixture decreases rapidly while the effective conductivity reaches a maximum.

We also developed efficient 3-D algorithms to calculate the microwave electromagnetic properties of binary mixtures of micro/nanoparticles. Our algorithm development was based on the generalized Mie (GMM) solution [7], which is capable of solving Maxwell's equations for the scattering problem of a particle ensemble composed of a large number of spherical particles. Our original plan was to benchmark the GMM simulation results against a 3-D FDTD model for a small number ( $N < 10$ ) of particles and then use it to extend the 2-D theoretical investigation described above to 3-D. However, once our experimental results revealed a negligible dielectric-properties enhancement associated with compact metallic nanoparticles, we shifted our focus carbon nanotube dispersions.

*Task 2.2.* The key first step towards developing a first-principles simulation tool for modeling microwave interactions with metallic nanoparticles was to create a hybrid solver that couples a computational electromagnetics model with a diffusive carrier transport model. Accordingly, we developed a multi-physics simulation tool that combines FDTD for solving the time-varying Maxwell's equations with an ensemble Monte Carlo (EMC) approach for stochastically solving the Boltzman transport equation. We characterized the EMC-FDTD solver in terms of grid spacing and carrier ensemble size (see Appendix F). We rigorously validated this state-of-the-art simulation tool, as described in Appendix B, by simulating the terahertz-



frequency skin effect in doped silicon. We obtained excellent agreement between our EMC-FDTD-computed effective conductivity of silicon at low doping densities and the measured effective conductivity reported by Jeon and Grischkowsky [8]. The promising nature of this multi-physics simulation tool led to more extensive development of the EMC-FDTD solver pursued under a separate project for characterizing the THz-frequency conductivity of silicon at higher doping densities. The second step of extending this work to metal nanoparticles was no longer needed once our focus shifted to CNTs, as microwave interactions with CNTs can be analyzed rigorously using classical/semi-classical electromagnetic models.

*Task 2.3.* As noted above, the microwave response of compact metallic nanoparticles is simply too weak to be of practical value for enhancing the microwave scattering and absorption cross-sections of malignant tumors. The fortuitous experimental discovery of the strong microwave response of CNTs changed the nature of this task from one of designing the optimum size and shape of compact metallic nanoparticles via simulation to one of identifying the range of CNT lengths that optimize the potential microwave contrast of malignant tumors. We found that the significant microwave contrast enhancement provided by large-aspect-ratio SWCNTs does not depend greatly on the specific lengths of the particles, which is affected by sonication duration. For example, we compared the properties of monodispersions consisting of either 1.0-micron-long CNTs or 0.5-micron-long CNTs, both at the same concentration of 1.0 mg/mL, and found no significant difference in the effective dielectric properties.

**Task 3.** Conduct experimental investigations of the microwave scattering and absorption properties of the micro/nanoparticle contrast agents in tissue-mimicking phantoms.

*Task 3.1.* We constructed tissue-mimicking (TM) materials from oil-in-gelatin dispersions following the procedure outlined in [9]. The dielectric properties of these materials can be customized to mimic the properties of a variety of human soft tissues by controlling the concentrations of the constituents. The results reported in [4] show that a 10%-oil mixture adequately replicates the microwave properties of malignant breast tissue over our frequency range of interest. Furthermore, these materials are relatively inexpensive to fabricate and possess long-term stability. Therefore, we constructed 10%-oil TM materials with various concentrations of SWCNTs as “tumor” phantoms. We mixed 1, 2, and 3 mg/mL of SWCNTs into a 1%-by-weight mixture of Pluronic (F127) and deionized water. Then we substituted these mixtures for the pure deionized water in the TM recipe described in [9]. The resulting percent-by-weight concentrations of SWCNTs in the TM samples were 0.07%, 0.15%, and 0.22%, respectively. For reference, we also constructed a pure TM mixture with the same amount of Pluronic as the other samples, but with no SWCNTs. The dielectric properties of each of the TM samples were characterized using the open-ended coaxial probe technique. At 3 GHz, we found that SWCNT concentrations as small as 0.22% by weight increased the relative permittivity of the TM material by 37% and the effective conductivity by 81%. Further details are provided in Appendix C and G.

*Task 3.2.* The SWCNTs used in the investigations conducted under this task were synthesized by a commercial vendor using a chemical vapor deposition technique and acid treated for purification. However, we briefly describe here the state-of-the-art synthesis protocols we developed for two other types of nanoparticles: isotropic (spherical) gold and silver

nanoparticles and anisotropic gold nanorods. These protocols include modifying the nanoparticle surface properties to stably suspend them in saline solutions representing realistic physiological conditions.

*Task 3.2a: Spherical nanoparticles.* We exploited the strong binding properties of DOPA peptides to anchor polymers onto material surfaces to form spherical gold and silver nanoparticles. We used self-assembling polymers to exert control of particle shape, size and properties. First, we synthesized a DOPA4 peptide in its solid phase, and linked it to a PEG2000 chain. The DOPA4 sequence was designed as a multifunctional molecule. The first function was to mediate formation of self-assembled nanoaggregates through hydrophobic DOPA aggregation, in order to yield DOPA-core/PEG-shell micelles that act as templates for mineralizing metallic nanoparticles. 10 nm structures were identified in both cryo-TEM and dynamic light scattering (DLS) techniques – strong evidence for micellular formation. The second function of the repeating DOPA peptide was the reduction of gold and silver ions to form metal nanoparticles. Control over the size of the gold nanoparticles was achieved through PEG-DOPA4 and metallic salt concentration. We have characterized the synthesized nanoparticles with transmission electron microscopy (TEM) and dynamic light scattering. Figure 4 shows TEM micrographs of 10 nm gold (525 nm plasmon) and 17 nm silver (415 nm plasmon) nanoparticles.

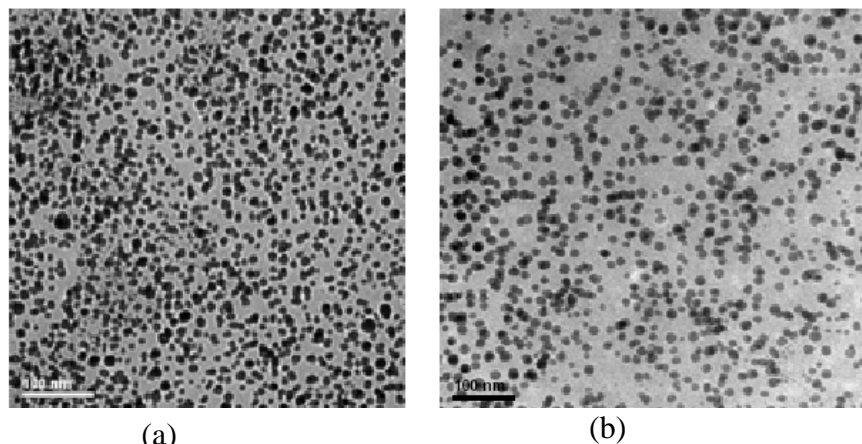


Figure 4. TEM micrographs of (a) 10 nm gold and (b) 17 nm silver nanoparticles formed with PEG-DOPA4 polymers. Scale bar = 100nm.

Further experimental characterization of the synthesized nanoparticles demonstrated that these polymers not only induced metallic nanoparticle formation, but also stably anchored PEG to the surface in saline conditions, the third vital function of the DOPA peptide. For example, after four centrifuge and washing steps, x-ray photoelectron spectroscopy (XPS) was performed on gold nanoparticles formed with the PEG-DOPA4 polymer and signal from both the metal and the polymer were detected, implying stable linkage of polymer on the nanoparticle surface. Further, PEG-DOPA4-synthesized gold nanoparticles were tested in saline to determine their stability against aggregation in physiological conditions, an important requirement for clinical use as well as further experimental measurements with phantom materials. No change in the dynamic light scattering properties of the nanoparticle dispersions was detected even up to 500 mM salt content, implying successful particle dispersion, while the conventional citrate-stabilized gold NPs aggregated at concentrations as low as 10 mM.

*Task 3.2b: Nanorods.* Using an alternative synthesis route, we fabricated gold nanorods with controlled aspect ratios. In this case, we used a two-step synthesis/coating strategy. First, we

used the surfactant CTAB as a reducing agent and template to form CTAB-coated nanorods and tuned the aspect ratio of the structures with control over gold salt and seed concentrations. In a second step, we replaced the CTAB coating with biocompatible surface-stabilizing molecules with anti-fouling PEG5000-thiol. Briefly, CTAB-gold nanorod suspensions were centrifuged, and excess CTAB-containing supernatant solution was discarded. A PEG-SH solution was added to the gold nanorod pellet, and mixed for 24 hours. The solution was centrifuged and supernatant solution was discarded; this process was repeated twice. We characterized the synthesized nanorods using both TEM and optical extinction spectroscopy. A TEM micrograph and optical extinction spectra of synthesized gold nanorods can be seen in Figure 5. The second step of coating replacement was demonstrated to be an essential step toward particle stability. Surface plasma analysis indicated that PEG-coated nanorods remained more stable towards aggregation in saline than either the conventional citrate or CTAB stabilized nanorods.

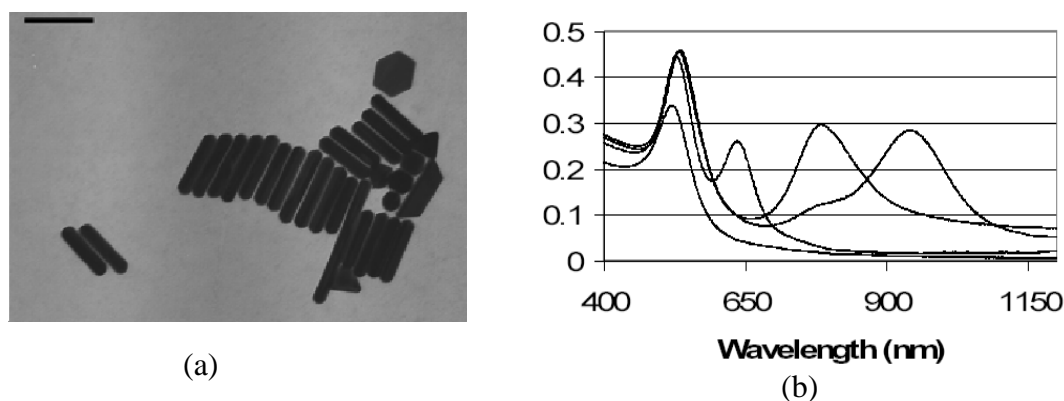


Figure 5. (a) TEM micrograph of gold nanorods synthesized with the CTAB-mediated method with an aspect ratio of  $\sim 6:1$ . (b) Optical extinction spectra of gold nanorods with various aspect ratios. The shift of the optical resonance peaks indicates that the nanorod aspect ratio can be tuned over a wide range.

*Task 3.3.* We complemented the use of simple experimental phantoms in Task 3.4 by the use of complex (anatomically realistic) numerical breast phantoms for the microwave scattering studies conducted here under Task 3.3. The results of the dielectric characterization experiments described in Task 3.1 were used in microwave imaging studies in order to determine the impact of the SWCNT-induced dielectric-properties changes on microwave breast cancer detection [10]. Briefly, we applied microwave inverse scattering techniques to reconstruct images of numerical breast phantoms with a compact malignant lesion. Two images were reconstructed: an image of a phantom with the endogenous dielectric properties of the tumor and another with elevated dielectric properties values due to the carbon nanotubes. A differential image was formed by subtracting the two images obtained from pre- and postcontrast measurements. Using this differential imaging technique, Shea et al. [10] reported detection of previously undetectable tumors in four different classes of numerical phantoms that ranged from “mostly fatty” to “extremely dense” in radiographic density. These results suggest that the changes in dielectric properties reported under Task 3.1 (and in Appendix C) are significant enough to dramatically improve the sensitivity of microwave imaging. We also created differential images for the case of microbubbles as the assumed contrast agent and obtained similarly promising results [10].

*Task 3.4a: Microbubbles.* We characterized the thermoacoustic response of simple “tumors” comprised of 6-mm-diameter plastic tubes filled with microbubble-EG dispersions. Appendix A reports the details of the experimental set-up and shows the thermoacoustic temporal waveforms measured for each of six targets. The amplitude of the response diminishes and the temporal width decreases with increasing concentration of microbubbles. We conducted an analysis of the effect of acoustic scattering to confirm that the observed reduction in the first peak of the thermoacoustic waveform is indeed due to the reduced effective conductivity (as shown in Figure 2 of Appendix A) rather than due to increased acoustic attenuation. With organic-shell microbubbles, we expect the same trend of reduced amplitude but a broadening of the temporal width.

*Task 3.4b: Metallic nanoparticles.* We conducted microwave heating experiments on the low-concentration aqueous solutions of metallic nanoparticles synthesized in Task 3.2 to characterize the absorption and thermal properties of these particles. The schematic diagram of the experimental setup is demonstrated in Figure 6. Briefly, a 4-GHz microwave signal was generated and amplified to 8W. The microwave source was matched to a section of waveguide to heat the nanoparticle solution (contained in a plastic vial) placed at the waveguide aperture. The voltage standing wave ratio (VSWR) at the waveguide input was carefully calibrated for all measurements. A computer was used to accurately control the microwave source and the heating/cooling phases of the sample. A Luxtron I652 fiber-optic temperature sensor was inserted to the sample vial to record temperature in real time. For each sample, the heating/cooling cycles were repeated for several times to confirm repeatability. Figure 7 shows the temperature trace of a 5mM gold nanorod solution compared to deionized (DI) water for three heating/cooling cycles. Initially, we assumed that the compact nanoparticles were responsible for the enhanced heating response. However, we conducted additional experiments with CTAB surfactant added to the DI water (e.g., no nanoparticles) and discovered that it was the CTAB surfactant – not the nanoparticles – that was responsible for the heating enhancement.

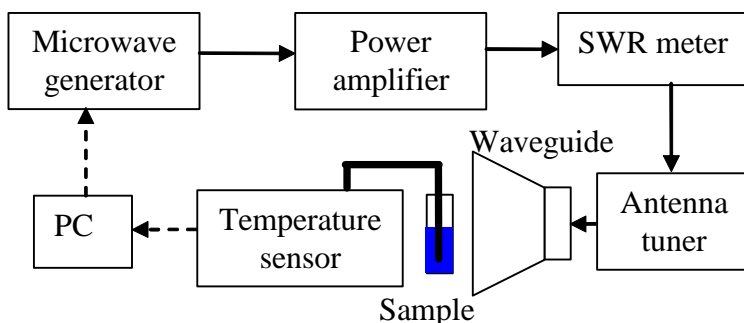


Figure 6. Experimental setup for characterizing the microwave heating efficiency of nanoparticle solutions.

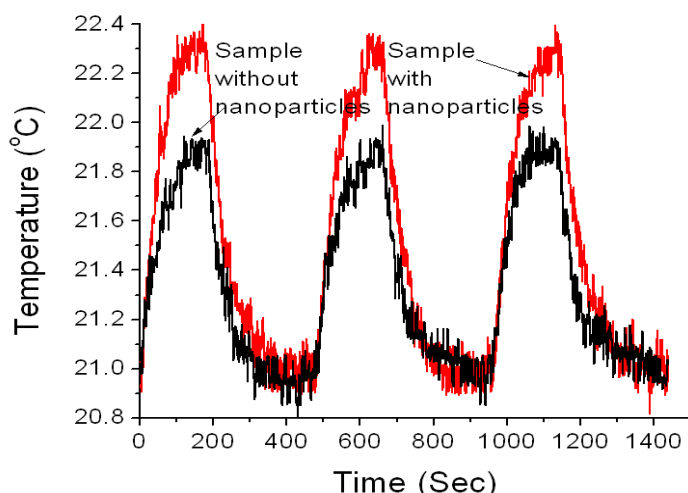


Figure 7. Temperature traces for three heating/cooling cycles of an aqueous solution of 5mM 6:1-aspect-ratio nanorods (red curve) compared to pure DI water (black curve). The sample was illuminated with microwave energy for three minutes for each cycle and turned off for four minutes for the sample to cool.

*Task 3.4c: SWCNTs.* We conducted heating efficiency experiments (at 3 GHz) using the TM materials described in Task 3.1, mixed with various concentrations of SWCNTs that have been identified to be non-toxic in mice. We chose 3 GHz because of its relevance to both microwave-induced thermoacoustic imaging and hyperthermia treatment. We prepared the samples for the heating experiments by pouring the liquid TM mixture into a 1.1-mm-inner-diameter glass capillary tube. The mixture was allowed to gel around a fiber-optic temperature probe connected to a calibrated fluoroptic thermometer. We note that the reference sample was constructed from a pure TM mixture with the same amount of Pluronic as the other samples, but with no SWCNTs. The capillary tube was inserted through a small hole drilled into the center of the broad wall of an S-band waveguide. A microwave synthesizer and amplifier generated 1 W of continuous microwave power at 3 GHz that was delivered to the sample via the waveguide. The fluoroptic thermometer recorded the time-varying temperature of each sample as it was heated. We heated each sample for 3 min, then turned off the microwave source and allowed it to cool for 5 min. The complete set of results from this study is reported in Appendix C (Figure 3 and Table II therein). We demonstrated measurement repeatability for each concentration. The measured data shows that as the concentration of SWCNTs increases, the maximum temperature also increases. The temperature increase scales roughly linearly with the increase in conductivity reported in Task 3.1 (and in Table I of Appendix C). SWCNT concentrations as small as 0.22% by weight led to an average steady-state temperature rise that was 6°C higher than the rise observed in the TM material without SWCNTs. Similarly promising results were obtained for the dispersions of SWCNTs in water and PL-PEG (Appendix E).

## Key Research Accomplishments

- Validated two complementary techniques for microwave-frequency dielectric properties measurements, namely a wideband (0.5-20 GHz) open-ended coaxial probe technique and a narrowband cavity perturbation technique.
- Conducted wideband and narrowband microwave-frequency measurements of the effective electromagnetic properties of liquid dispersions of candidate micro/nanoparticle contrast agents including air-filled microbubbles, metallic nanoparticles, and carbon nanotubes.
- Demonstrated that air-filled microbubbles with clinically relevant concentrations significantly decrease the microwave dielectric properties of the liquid dispersion relative to the pure liquid without microbubbles, and concluded that microbubbles are a promising contrast agent for contrast-enhanced microwave breast cancer detection.
- Demonstrated that compact metallic nanoparticles do not significantly alter the microwave dielectric properties of the liquid dispersion relative to the pure liquid without nanoparticles, and therefore are unlikely to be promising as contrast agents for contrast-enhanced microwave breast cancer detection.
- Demonstrated that single-wall carbon nanotubes (SWCNTs) significantly increase the microwave dielectric properties of the liquid dispersion relative to pure liquid without SWCNTs. Also demonstrated that SWCNTs at biologically relevant concentrations significantly increase the microwave dielectric properties of tumor-mimicking phantom materials, and concluded that SWCNTs are a promising contrast agent for contrast-enhanced microwave breast cancer detection.
- Developed 2D classical electromagnetics simulation tools for calculating the effective dielectric properties of micro/nanoparticle dispersions and used the tools to investigate a variety of micro/nanoparticle dispersions at microwave frequencies.
- Compared 2D numerical simulation results with experimental measurements of microbubble dispersions and obtained excellent agreement in the computed and measured effective dielectric properties.
- Compared 2D numerical simulation results with experimental measurements of dispersions containing compact (isotropic or low-aspect-ratio anisotropic) metallic nanoparticles and found discrepancies in the computed and measured values that may be attributed to interfacial effects and/or limitations of the 2D simulation.
- Developed a 2D numerical simulation tool that couples the full-wave FDTD method for solving Maxwell's equations with an ensemble Monte Carlo approach for solving the Boltzmann transport equation, and validated the tool by simulating electromagnetic wave interactions with low-doped silicon at THz frequencies.
- Characterized the dielectric properties of a variety of CNT-based particles in liquid dispersions and identified single-wall CNTs with large aspect ratios (e.g. length-to-diameter ratios on the order of  $\sim 1000:1$ ) to offer the greatest field enhancement and corresponding increase in effective dielectric properties.

- Developed a fabrication procedure for constructing tumor-mimicking phantoms with and without SWCNT mixtures at concentrations known to be non-toxic in mice.
- Developed state-of-the-art synthesis protocols of spherical nanoparticles and nanorods and modified their surface properties to stably suspend them in saline solutions representing realistic physiological conditions.
- Conducted microwave heating experiments on low-concentration dispersions of compact metallic nanoparticles and characterized their microwave heating efficiency relative to pure liquid samples without nanoparticles. Demonstrated that the observed increase in heating efficiency was due to the surfactant rather than the nanoparticles themselves.
- Conducted microwave heating experiments on low-concentration dispersions of SWCNTs and characterized their microwave heating efficiency relative to pure liquid samples with the surfactant but without nanotubes. Demonstrated that the observed increase in heating efficiency was indeed due to the CNTs.
- Demonstrated that microbubbles diminish the thermoacoustic response of simple “tumor” targets compared to the pre-contrast-agent response, indicating that such agents may enhance the sensitivity of cancer detection through the use of differential thermoacoustic imaging techniques.

## Reportable Outcomes

### Journal papers

A. Mashal, J. H. Booske, and S. C. Hagness, "Towards contrast-enhanced microwave-induced thermoacoustic imaging of breast cancer: An experimental study of the effects of microbubbles on simple thermoacoustic targets," *Physics in Medicine and Biology*, vol. 54, pp. 641-650, 2009. **Reprint included in Appendix A.**

K. Willis, J. Ayubi-Moak, S. C. Hagness, and I. Knezevic, "Global modeling of carrier-field dynamics in semiconductors using EMC-FDTD," *Journal of Computational Electronics*, DOI: 10.1007/s10825-009-0280-4, August 12, 2009. **Reprint included in Appendix B.**

A. Mashal, B. Sitharaman, X. Li, P. Avti, A. V. Sahakian, J. H. Booske, and S. C. Hagness, "Toward carbon-nanotube-based theranostic agents for microwave detection and treatment of breast cancer: Enhanced dielectric and heating response of tissue-mimicking materials," *IEEE Transactions on Biomedical Engineering*, vol. 57, no. 8, pp. 1831-1834, August 2010. **Reprint included in Appendix C.**

### Invited Keynote Presentations at Conferences

S. C. Hagness, "Microwave Imaging in Medicine: Promises and Future Challenges," Opening General Lecture, XXIX General Assembly of the International Union of Radio Science, Chicago, IL, August 2008.

### Invited conference papers

M. Lazebnik, S. C. Hagness, and J. H. Booske, "Dielectric-Properties Contrast Enhancement for Microwave Breast Cancer Detection: Numerical Investigations of Microbubble Contrast Agents," XXIX General Assembly of the International Union of Radio Science (URSI), Chicago, IL, August 2008 (4 pages). **Reprint included in Appendix D.**

A. Mashal, E. Zastrow, P. Avti, B. Sitharaman, J. H. Booske, and S. C. Hagness, "Characterization of the Dielectric and Heating Response of Carbon Nanotubes for Enhancing Microwave Detection and Treatment of Breast Cancer," IEEE Antennas and Propagation Society International Symposium and CNC/USNC/URSI Radio Science Meeting, Toronto, Canada, July 2010. **Reprint included in Appendix E.**

### Contributed conference papers

S. C. Hagness (presenter), P. Messersmith, A. Sahakian, J. Booske, I. Knezevic, and X. Li, "Nanoparticle Contrast Agents for Enhanced Microwave Imaging of Breast Cancer," Department of Defense Breast Cancer Research Program Era of Hope Meeting, Baltimore, MD, June 2008.

K. J. Willis, S. C. Hagness, and I. Knezevic, "A Global EMC-FDTD Simulation Tool for High-Frequency Carrier Transport in Semiconductors," Proceedings of the 13th International



Workshop on Computational Electronics (IWCE 2009), Beijing, China, May 27-29, 2009.  
**Reprint included in Appendix F.**

A. Mashal, B. Sitharaman, J. H. Booske, and S. C. Hagness, “Dielectric Characterization of Carbon Nanotube Contrast Agents for Microwave Breast Cancer Detection,” IEEE International Symposium on Antennas and Propagation, Charleston, SC, June 2009 (4 pages). ***Received an Honorable Mention in the Student Paper Competition. Reprint included in Appendix G.***

W. Yip, A.V. Sahakian and X. Li, “Numerical Investigation of Dielectric Properties of Metallic Nano/Microspheres in the Microwave Frequency Range,” Progress in Electromagnetic Research (PIERS) Conference, Cambridge, MA, July 5-8, 2010.

Degrees obtained with support of this award

Mariya Lazebnik, Ph.D. degree, Aug. 2008. Dissertation: “Ultrawideband spectroscopy and dielectric-properties contrast enhancement for microwave breast cancer detection and treatment.” Position after graduation (current position): Senior RF Scientist, Medtronic, Minneapolis, MN.

Keely Willis, Ph.D. degree, Dec. 2010 (expected). Dissertation: “EMC/FDTD/MD for multiphysics characterization of semiconductors at THz frequencies.”

Al Mashal, Ph.D. degree, Jan. 2011 (expected). Dissertation: “Influence of Intrinsic and Extrinsic Properties Contrast on Microwave-Induced Thermoacoustic Response of Breast Tissue.” Position after graduation (offer accepted): Senior Scientist, Actium Biosystems, Boulder, CO.

Wendy Yip, Ph.D. degree, June 2011 (expected). Dissertation: “Investigation of Electromagnetic Properties of Multi-particle Systems in the Optical and Microwave Regions.”

Funding applied for based on work supported by this award

“Tumor-targeting single-wall carbon nanotubes for microwave-based imaging and hyperthermia treatment of breast cancer: A small animal study.” Department of Defense Breast Cancer Research Program Synergistic Idea Award (W81XWH-10-1-0522), B. Sitharaman, Stony Brook University P.I. and S. C. Hagness, University of Wisconsin--Madison P.I., 8/1/10-8/31/12.

## Conclusions

During the course of this project, we achieved significant milestones in our contrast-enhanced microwave breast cancer detection research – the demonstration of *significant changes* in the microwave-frequency effective dielectric properties, heating efficiency, and thermoacoustic response of mixtures containing either microbubbles or single-wall carbon nanotubes. To the best of our knowledge, these accomplishments represent the first experimental laboratory demonstrations of contrast enhancement in a context relevant to microwave breast cancer detection. Our results have advanced our understanding of microwave interactions with microparticles and nanoparticles in dispersions and have revealed that a very large aspect ratio is required in order for metallic particles to enhance the microwave response.

In a complementary NIH-funded research project involving the development of microwave breast imaging techniques, we have investigated the impact of the level of dielectric-properties changes found in our contrast agent research (this project) on the sensitivity of detecting small (~1 cm) tumors in anatomically realistic numerical breast phantoms. We created 3D microwave images of each breast phantom by applying inverse scattering algorithms to the microwave scattered signals recorded for each phantom, both before and after the contrast agent injection. We are very encouraged by the fact that tumors were detected via differential imaging in phantoms representing a wide range of breast tissue densities, ranging from mostly fatty to extremely dense.

Thus our work to date strongly suggests that microwave imaging enhanced with microparticle or nanoparticle contrast agents systemically delivered to the tumor has the potential to overcome many of the limitations of conventional breast cancer screening modalities. The physical basis for our microwave imaging approach is the combined intrinsic and extrinsic microwave-frequency dielectric contrast between normal breast tissue and malignant tumors containing metal nanoparticles. Our proposed approach takes advantage of biophysical contrast mechanisms, such as water content, angiogenesis, blood-flow rate, and temperature, and dramatically augments them by the selective introduction of metallic nanoparticles into the tumor via passive or targeted delivery. Microwave imaging techniques that exploit the resultant unprecedented contrast should provide the sensitivity and resolution needed to reliably detect extremely small (less than 1 cm) malignant tumors even in challenging cases of radiographically dense breast tissue or tumors located in the upper outer breast quadrant near the chest wall where an estimated 50% of all breast tumors occur. Microwave imaging can also take advantage of enhanced backscatter due to vascularization and accumulation of contrast agent particles in malignant tumors, as well as morphology-dependent characteristics such as spectral and polarization signatures, for the purpose of lesion discrimination and characterization. The predicted safety, comfort (no breast compression), and ultra-low-cost features of contrast-enhanced microwave imaging means that this breast cancer screening technology could be made widely available to the general public, including medically under-served populations, and should improve public compliance with annual screening recommendations.

## References

- [1] D. Popovic, L. McCartney, C. Beasley, M. Lazebnik, M. Okoniewski, S. C. Hagness, and J. H. Booske, "Precision open-ended coaxial probes for in vivo and ex vivo dielectric spectroscopy of biological tissues at microwave frequencies," *IEEE Transactions on Microwave Theory and Techniques*, vol. 53, pp. 1713-1722, 2005.
- [2] D. M. Hagl, D. Popovic, S. C. Hagness, J. H. Booske, and M. Okoniewski, "Sensing volume of open-ended coaxial probes for dielectric characterization of breast tissue at microwave frequencies," *IEEE Transactions on Microwave Theory and Techniques*, vol. 51, pp. 1194-1206, 2003.
- [3] M. Lazebnik, L. McCartney, D. Popovic, C. B. Watkins, M. J. Lindstrom, J. Harter, S. Sewall, A. Magliocco, J. H. Booske, and M. Okoniewski, "A large-scale study of the ultrawideband microwave dielectric properties of normal breast tissue obtained from reduction surgeries," *Physics in Medicine and Biology*, vol. 52, pp. 2637--2656, 2007.
- [4] M. Lazebnik, D. Popovic, L. McCartney, C. B. Watkins, M. J. Lindstrom, J. Harter, S. Sewall, T. Ogilvie, A. Magliocco, and T. M. Breslin, "A large-scale study of the ultrawideband microwave dielectric properties of normal, benign and malignant breast tissues obtained from cancer surgeries," *Physics in Medicine and Biology*, vol. 52, pp. 6093--6115, 2007.
- [5] B. Meng, J. Booske, and R. Cooper, "Extended cavity perturbation technique to determine the complexpermittivity of dielectric materials," *IEEE Transactions on Microwave Theory and Techniques*, vol. 43, pp. 2633--2636, 1995.
- [6] E. Stride and N. Saffari, "Investigating the significance of multiple scattering in ultrasound contrast agent particle populations," *IEEE Transactions on Ultrasonics, Ferroelectrics and Frequency Control*, vol. 52, pp. 2332-2345, 2005.
- [7] Y. L. Xu, "Electromagnetic scattering by an aggregate of spheres," *Applied Optics*, vol. 34, pp. 4573-4573, 1995.
- [8] T. I. Jeon and D. Grischkowsky, *Phys. Rev. Lett.*, vol. 78, pp. 1106--1109, 1997.
- [9] M. Lazebnik, E. L. Madsen, G. R. Frank, and S. C. Hagness, "Tissue-mimicking phantom materials for narrowband and ultrawideband microwave applications," *Phys. Med. Biol.*, vol. 50, pp. 4245--4258, 2005.
- [10] J. D. Shea, P. Kosmas, S. C. Hagness, and B. D. Van Veen, "Contrast-enhanced microwave imaging of breast tumors: A computational study using 3D realistic numerical phantoms," *Inverse Problems*, vol. 26, 074009 (22 pages), 2010.

## **Personnel Receiving Pay from the Research Effort**

### Key Personnel – Northwestern University

Xu Li – Principal Investigator

Alan V. Sahakian – Co-Investigator

Phil Messersmith – Co-Investigator

### Personnel in Training Positions – Northwestern University

Wendy Yip – Graduate Student Research Assistant

Jianmin Gong – Graduate Student Research Assistant

### Key Personnel –University of Wisconsin-Madison

Susan C. Hagness – Co-Principal Investigator

John Booske – Co-Investigator

Irena Knezevic – Co-Investigator

### Personnel in Training Positions –University of Wisconsin-Madison

Mariya Lazebnik – Graduate Student Research Assistant

Keely Willis – Graduate Student Research Assistant

Al Mashal – Graduate Student Research Assistant

### Personnel in Support Positions –University of Wisconsin-Madison

Anthony Hammond – Academic Staff

## **Appendix A**

A. Mashal, J. H. Booske, and S. C. Hagness, "Towards contrast-enhanced microwave-induced thermoacoustic imaging of breast cancer: An experimental study of the effects of microbubbles on simple thermoacoustic targets," *Physics in Medicine and Biology*, vol. 54, pp. 641-650, 2009.

## **Appendix B**

K. Willis, J. Ayubi-Moak, S. C. Hagness, and I. Knezevic, "Global modeling of carrier-field dynamics in semiconductors using EMC-FDTD," *Journal of Computational Electronics*, DOI: 10.1007/s10825-009-0280-4, August 12, 2009.

## **Appendix C**

A. Mashal, B. Sitharaman, X. Li, P. Avti, A. V. Sahakian, J. H. Booske, and S. C. Hagness, "Toward carbon-nanotube-based theranostic agents for microwave detection and treatment of breast cancer: Enhanced dielectric and heating response of tissue-mimicking materials," *IEEE Transactions on Biomedical Engineering*, vol. 57, no. 8, pp. 1831-1834, August 2010.

## **Appendix D**

M. Lazebnik, S. C. Hagness, and J. H. Booske, "Dielectric-Properties Contrast Enhancement for Microwave Breast Cancer Detection: Numerical Investigations of Microbubble Contrast Agents," XXIX General Assembly of the International Union of Radio Science (URSI), Chicago, IL, August 2008 (4 pages).

## **Appendix E**

A. Mashal, E. Zastrow, P. Avti, B. Sitharaman, J. H. Booske, and S. C. Hagness, "Characterization of the Dielectric and Heating Response of Carbon Nanotubes for Enhancing Microwave Detection and Treatment of Breast Cancer," IEEE Antennas and Propagation Society International Symposium and CNC/USNC/URSI Radio Science Meeting, Toronto, Canada, July 2010.

## **Appendix F**

K. J. Willis, S. C. Hagness, and I. Knezevic, "A Global EMC-FDTD Simulation Tool for High-Frequency Carrier Transport in Semiconductors," Proceedings of the 13th International Workshop on Computational Electronics (IWCE 2009), Beijing, China, May 27-29, 2009.

## **Appendix G**

A. Mashal, B. Sitharaman, J. H. Booske, and S. C. Hagness, "Dielectric Characterization of Carbon Nanotube Contrast Agents for Microwave Breast Cancer Detection," IEEE International Symposium on Antennas and Propagation, Charleston, SC, June 2009 (4 pages).

# Toward contrast-enhanced microwave-induced thermoacoustic imaging of breast cancer: an experimental study of the effects of microbubbles on simple thermoacoustic targets

Alireza Mashal, John H Booske and Susan C Hagness

Department of Electrical and Computer Engineering, University of Wisconsin, Madison, WI, USA

E-mail: [amashal@wisc.edu](mailto:amashal@wisc.edu), [booske@engr.wisc.edu](mailto:booske@engr.wisc.edu) and [hagness@engr.wisc.edu](mailto:hagness@engr.wisc.edu)

Received 24 May 2008, in final form 4 December 2008

Published 6 January 2009

Online at [stacks.iop.org/PMB/54/641](http://stacks.iop.org/PMB/54/641)

## Abstract

Microwave-induced thermoacoustic tomography (MI-TAT) is an imaging technique that exploits dielectric contrast at microwave frequencies while creating images with ultrasound resolution. We propose the use of microbubbles as a dielectric contrast agent for enhancing the sensitivity of MI-TAT for breast cancer detection. As an initial investigation of this concept, we experimentally studied the extent to which the microwave-induced thermoacoustic response of a dielectric target is modified by the presence of air-filled glass microbubbles. We created mixtures of ethylene glycol with varying weight percentages of microbubbles and characterized both their microwave properties (0.5–6 GHz) and thermoacoustic response when irradiated with microwave energy at 3 GHz. Our data show that the microbubbles considerably lowered the relative permittivity, electrical conductivity and thermoacoustic response of the ethylene glycol mixtures. We hypothesize that the interstitial infusion of microbubbles to a tumor site will similarly create a smaller thermoacoustic response compared to the pre-contrast-agent response, thereby enhancing sensitivity through the use of differential imaging techniques.

(Some figures in this article are in colour only in the electronic version)

## 1. Introduction

Microwave-induced thermoacoustic tomography (MI-TAT) is a hybrid imaging modality that exploits dielectric-properties contrasts while creating images with ultrasound-quality resolution. In thermoacoustic imaging, the tissue is irradiated with sub-microsecond

electromagnetic pulses. This electromagnetic energy is selectively absorbed by the higher-conductivity tissues and induces acoustic waves by the means of thermoelastic expansion. These thermoacoustic signals are detected by ultrasound transducers and processed for image reconstruction. One promising application for microwave imaging techniques such as MI-TAT (as well as others) is early-stage breast cancer detection (Kruger *et al* 1999, 2002, Ku *et al* 2005, Xu *et al* 2005, Meaney *et al* 2000, Li *et al* 2005).

A recently published large-scale spectroscopy study conducted by the University of Wisconsin and the University of Calgary (Lazebnik *et al* 2007) has shown that the contrast in the microwave-frequency dielectric properties between malignant tissues and healthy adipose-dominated tissues in the breast is as large as 10:1, but the contrast between malignant and normal glandular/fibroconnective tissues in the breast is not more than about 10%. Nearly all breast cancers originate in the ducts or lobules of the breast, which are glandular tissues. The use of contrast agents, such as those that accumulate in tumors via passive mechanisms (Maeda *et al* 2000), may enhance the dielectric contrast between malignant and normal glandular tissue, thereby increasing the sensitivity of microwave imaging for breast cancer detection.

Here, we propose air-filled microbubbles as a contrast agent in MI-TAT. Because of their echo-enhancing properties, microbubbles have been studied for the past several decades as a contrast agent in ultrasound imaging (Calliada *et al* 1998, Cosgrove 2006, Wells 2006). Microbubbles may also be advantageous in MI-TAT modalities because of their low microwave absorption. We hypothesize that the thermoacoustic response of a tumor infused with microbubbles will be not only smaller than that of surrounding normal glandular tissue structures but also smaller than the response of the tumor in its pre-contrast-agent state. This extrinsic dielectric contrast mechanism could be exploited via differential imaging whereby the breast is imaged before and after the contrast agent is injected.

As an initial step toward evaluating the feasibility of microbubbles as a contrast agent in MI-TAT, we tested the extent to which the microwave-induced response of a simple dielectric target is modified by the presence of microbubbles. The remainder of this paper is organized as follows. Section 2 summarizes the theory of thermoacoustic phenomena. Section 3 describes the methods used to create the thermoacoustic targets and experimentally characterize both their dielectric properties and thermoacoustic response. Section 4 discusses the results of the study, and the conclusions are summarized in section 5.

## 2. Theory

Thermoacoustic theory has been detailed in a number of review papers (see, for example, Tam 1986 and Xu and Wang 2006). Here, we briefly summarize the fundamental concepts. The thermoacoustic differential equation given by equation (1) is derived from the equations of motion and thermal expansion assuming a homogeneous acoustic and thermal medium

$$\nabla^2 p(\mathbf{r}, t) - \frac{1}{c^2} \frac{\partial^2}{\partial t^2} p(\mathbf{r}, t) = -\beta_e \rho \frac{\partial^2}{\partial t^2} T(\mathbf{r}, t). \quad (1)$$

Here  $p(\mathbf{r}, t)$  is the acoustic pressure at position  $\mathbf{r}$  and time  $t$ ,  $\beta_e$  is the volume expansion coefficient,  $T(\mathbf{r}, t)$  is the temperature rise throughout the medium due to microwave absorption,  $\rho$  is the mass density and  $c$  is the speed of sound.

For the case in which microwave power dissipation in a region is uniform and so rapid that thermal diffusion can be neglected, the temperature rise in that region can be described as

$$\Delta T = \frac{\text{SAR} \cdot \tau}{C_p}. \quad (2)$$

Here  $\tau$  is the microwave pulse length,  $C_p$  is the specific heat and SAR is the specific absorption rate, defined as  $\sigma|E|^2/2\rho$ , where  $E$  is the electric field,  $\sigma$  is the effective electrical conductivity and  $\rho$  is the mass density.

These equations suggest that a lesion with lowered conductivity should have a smaller local temperature rise and a smaller thermoacoustic response.

### 3. Materials and methods

#### 3.1. Thermoacoustic targets

Our thermoacoustic targets were composed of mixtures of ethylene glycol (EG) with 0%, 5%, 10%, 20% and 30% by weight concentrations of microbubbles. These concentrations are within the typical  $10^9$  microbubbles/mL dosage administered in human ultrasound procedures (Stride and Saffari 2005). The microbubbles used were air-filled glass spheres (iM30K, 3M) with an average diameter of  $18\ \mu\text{m}$  and a density of  $0.6\ \text{g mL}^{-1}$ . Ethylene glycol was chosen because it is a relatively inexpensive and readily available liquid with dielectric properties that are approximately within the range of biological tissues at the microwave frequency of interest (3 GHz). In this study, we were concerned only with the role of the dielectric properties on the thermoacoustic response and did not consider or characterize the effect of the thermal, mechanical or acoustic properties of the mixtures or their constituents. Thus those other properties did not influence our choice of the background liquid.

The mixtures were prepared by vigorously mixing EG with the microbubbles for 2 min before taking any measurements. The thermoacoustic targets were constructed by pouring the mixtures into plastic tubes with an inner diameter of 6 mm. The use of a plastic tube for target construction has been used in experimental work reported by other groups (Ku *et al* 2005, Jin *et al* 2007, Paltauf *et al* 2007). Both ends of the tube were sealed with vinyl plastic putty. The tube was placed in a stand and immersed in an oil tank.

#### 3.2. Dielectric characterization of the targets

The dielectric properties of the mixtures were characterized using a well established open-ended coaxial probe technique described in Popovic *et al* (2005). Briefly, the tip of hermetically sealed, stainless-steel/borosilicate glass coaxial probe was immersed in the liquid under test. The complex reflection coefficient was recorded using a performance network analyzer and converted into the complex dielectric properties using the procedure described in Popovic *et al* (2005). As reported in Popovic *et al* (2005), the measurement uncertainty of this technique is no more than approximately 10%.

We conducted dielectric spectroscopy measurements on freshly mixed EG/microbubble mixtures contained within glass test tubes of the same height as the plastic tubes used in the thermoacoustic measurements. Five dielectric measurements were made at three different depths in the test tubes spanning the frequency range 0.5–6 GHz and the results at each frequency were averaged. The range of depths spanned the region of the target that was illuminated with the microwaves in the thermoacoustic experiments. The measurements were made at room temperature (approximately 22 °C).

Since the air-filled microbubbles are less dense than the EG, they separate from the mixture over time and rise to the top. To ensure that the state of the mixture was the same for both our dielectric measurements and thermoacoustic experiments, we made dielectric measurements 2.5 min after mixing the solution—the amount of time that elapsed in the subsequent



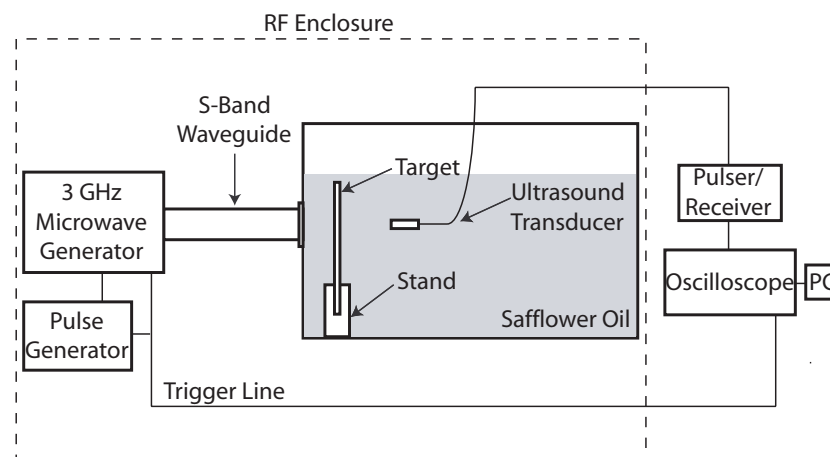


**Figure 1.** Thermoacoustic experimental setup.

thermoacoustic experiments between mixing the solution and recording the thermoacoustic response.

### 3.3. Thermoacoustic characterization of the targets

A schematic of the thermoacoustic experimental setup is shown in figure 1. Microwave pulses with a peak power of approximately 30 kW and a frequency of 3 GHz were delivered to the thermoacoustic target via an S-band rectangular waveguide (cross-sectional dimensions of 72 mm  $\times$  34 mm). A pulse generator (BNC 565, Berkeley Nucleonics) was used to set the pulse width to 0.9  $\mu$ s with a repetition frequency of 900 Hz. These settings correspond to an average power of 24 W. The ultrasound transducer was an unfocused piezoelectric transducer with a 2.25 MHz center frequency (60% 6 dB bandwidth) and 12.7 mm diameter (V306, Olympus). The transducer was fastened to a xyz-translation stage and was aligned to the target using the pulse echo mode of the ultrasound pulser/receiver (5800PR, Olympus). The ultrasound pulser/receiver was shielded from the microwave generator by an RF enclosure to eliminate microwave pickup.

Safflower oil was used as the acoustic coupling medium. The use of oil is advantageous because it has both low relative permittivity and conductivity and therefore provides a good dielectric contrast with the thermoacoustic target and good penetration depth into the tank. The stand and walls of the tank were constructed out of acrylic, which has similar dielectric properties as oil.

The thermoacoustic signal detected by the transducer during an experimental trial with a specific target was amplified by 60 dB using the pulser/receiver and averaged 200 times by the oscilloscope (Infiniium 54854A, Agilent). Both the microwave generator and oscilloscope were triggered by the pulse generator. The transducer and stand were kept stationary between different thermoacoustic measurements.

### 3.4. Speed of sound characterization of the targets

We made speed of sound measurements using the well accepted substitution technique described in Kremkau *et al* (1981) at 2.25 MHz. Mixtures of EG with specific microbubble

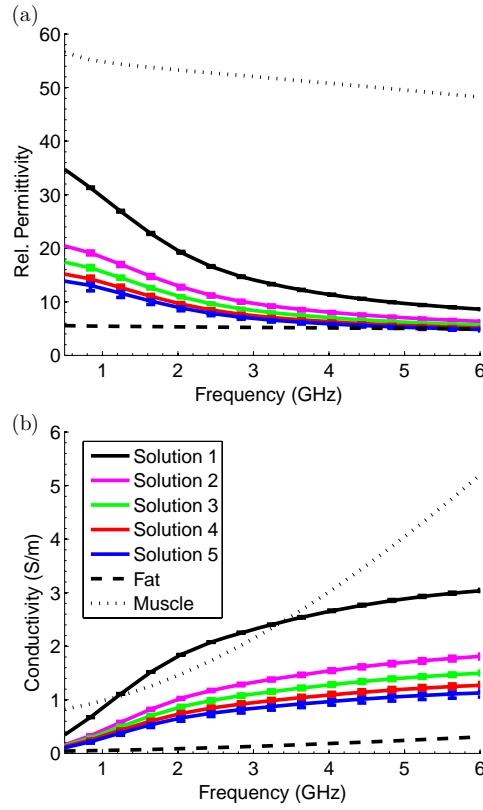


**Figure 2.** (a) Relative permittivity and (b) effective conductivity of EG solutions with varying concentrations of microbubbles along with the properties of non-infiltrated fat and muscle described by the four-pole Cole–Cole model (Gabriel *et al* 1996).

concentrations were poured into a cylindrical acrylic tube with a 7.6 cm diameter and a 25  $\mu\text{m}$  polyvinylidene chloride (Saran Wrap) window. The sample was then placed in a water tank and illuminated with an ultrasound beam. The propagation time was recorded with and without the sample. The speed of sound was then calculated from the relation (Kremkau *et al* 1981):

$$c = \frac{c_w d}{d - c_w \Delta t}. \quad (3)$$

Here  $d$  is the length of the cylindrical sample,  $c_w$  is the speed of sound in water at 22 °C and  $\Delta t$  is the change in propagation time with and without the sample. The speed of sound measurements were made 2.5 min after mixing the solutions, for the reasons described in section 3.2.

## 4. Results and discussion

### 4.1. Dielectric properties

Figures 2(a) and (b) show the relative permittivity and effective conductivity of EG and the four different microbubble solutions over a frequency range of 0.5–6 GHz at the time that corresponded to when the thermoacoustic response was recorded. The curves depict the

**Table 1.** Summary of data presented in figure 2.

Solution	Initial microbubble concentration (% by weight)	Estimated actual concentration (% by weight)	Average $\epsilon_r$ (3 GHz)	Average $\sigma$ (3 GHz) (S/m)
1	0	0	14.03	2.32
2	5	20	9.66	1.33
3	10	30	8.34	1.11
4	20	35	7.38	0.95
5	30	40	6.86	0.84
6	100	100	NA <sup>a</sup>	NA <sup>a</sup>

<sup>a</sup> NA: not available.

average of the different measurements and the vertical bars represent the deviation of the individual measurements from the average value. Table 1 summarizes the relative permittivity and conductivity of these solutions at 3 GHz. Figure 2 shows that the relative permittivity and conductivity of the solutions decrease with increasing microbubble concentration, as expected. In addition to the microwave properties of the solutions investigated, the microwave properties of non-infiltrated fat and muscle are plotted using the four-pole Cole–Cole models reported by Gabriel *et al* (1996) for comparison.

Since the microbubbles tend to float to the top of the mixture over time, the actual concentration of microbubbles seen by the microwaves is higher than that of the original mixture. In order to estimate the actual concentration of microbubbles at the time the thermoacoustic response was recorded, additional higher concentration microbubble mixtures were made. The dielectric properties of these additional mixtures were measured *immediately* after the solution was created. These instantaneous dielectric measurements of the higher concentration mixtures (not shown) were then compared to those of figure 2 to determine the actual weight concentration of the mixtures at the time of the thermoacoustic measurements. The estimated concentrations are summarized in table 1. These measurements establish that the dielectric properties of a solution that was created by using 5% by weight concentration of microbubbles, at two and a half minutes, are equivalent to a 20% by weight concentration of microbubbles. Similarly, mixtures created by using 10%, 20% and 30% by weight concentration of microbubbles, at two and a half minutes, have dielectric properties of solutions with 30%, 35% and 40% by weight microbubbles, respectively.

#### 4.2. Thermoacoustic response

Figure 3 shows the temporal thermoacoustic waveform as detected by the ultrasound transducer for Solution 1 (pure EG solution), for five different trials, where each trial involved a fresh mixture of the same concentration. The microwave pulse illuminates the target at  $t = 0 \mu\text{s}$ . Since the electromagnetic energy is delivered to the target at the speed of light, the acoustic waves are induced at  $t \approx 0 \mu\text{s}$ . The approximately  $34 \mu\text{s}$  delay corresponds to the propagation time of the induced acoustic waves to reach the transducer in oil. Each thermoacoustic temporal waveform shown in figure 3 is composed of mainly three lobes. This is the expected pressure profile emitted from a cylindrical thermoacoustic target inside a background medium with a different density and speed of sound (Diebold *et al* 1990). The first positive and first negative lobes are characteristic of two-dimensional waves emitted from a cylindrical acoustic source.

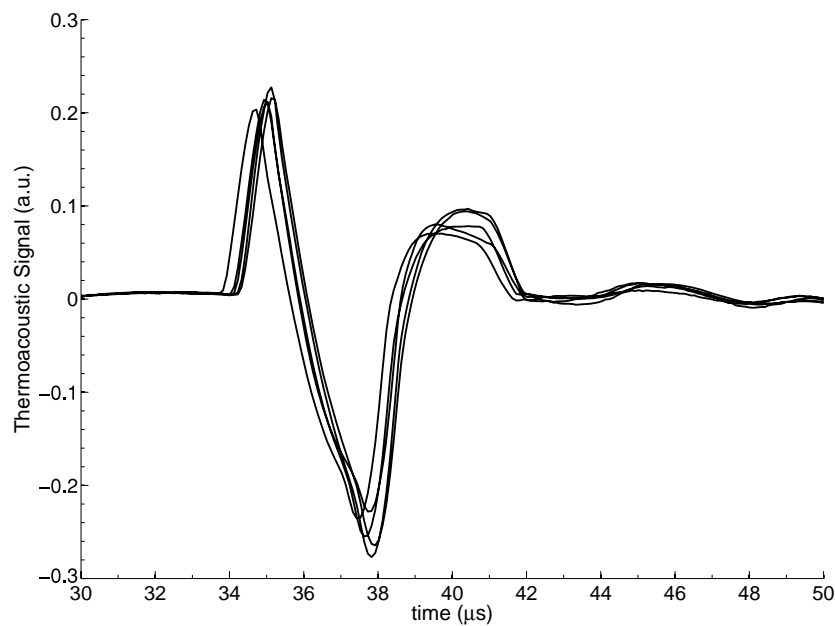


**Figure 3.** Thermoacoustic temporal waveform of Solution 1 for five independent trials. The waveform shown for each trial represents an average of 200 measurements. The small variations observed across waveforms reflect slight differences between trials (e.g., small differences in the plastic tubes and their positions).

The third positive lobe and ensuing acoustic signature trail is due to the difference in the density and speed of sound of the target, EG, and the background medium, safflower oil.

We used the multiple trials reported in figure 3 to characterize the repeatability of our measurements under experimental conditions that are intended to be invariant (e.g., fixed concentration of microbubbles). This assessment is critical for correctly interpreting the differences observed in the thermoacoustic waveform under intentionally varying experimental conditions (differing concentrations, for example). Figure 3 shows that the variations in the thermoacoustic response of similar dielectric targets are no greater than approximately 6% in the first peak and 10% in the temporal width when compared to the average values. The temporal fluctuations are no greater than approximately  $1 \mu\text{s}$ . We attribute these variations in the thermoacoustic waveform to small changes in the physical properties of the plastic tube and the placement of the target relative to the ultrasound transducer. These variations are inevitably introduced between different trials.

Figure 4 shows thermoacoustic temporal waveforms for one representative trial of each of the solutions. The average and the range of minimum and maximum values of the first peak as well as the temporal width of the thermoacoustic response for the five different trials of each concentration are summarized in table 2. Solution 1 (pure EG) and Solution 6 (the plastic tube filled with only microbubbles) serve as an upper and a lower bound of the thermoacoustic response. The thermoacoustic response of Solution 6 is very small, and most likely due to the microwave absorption of the glass shells of the microbubbles and the plastic tube. The change observed across solutions is clearly larger than the variation for repeat measurements with the same solution, as seen in figure 3.

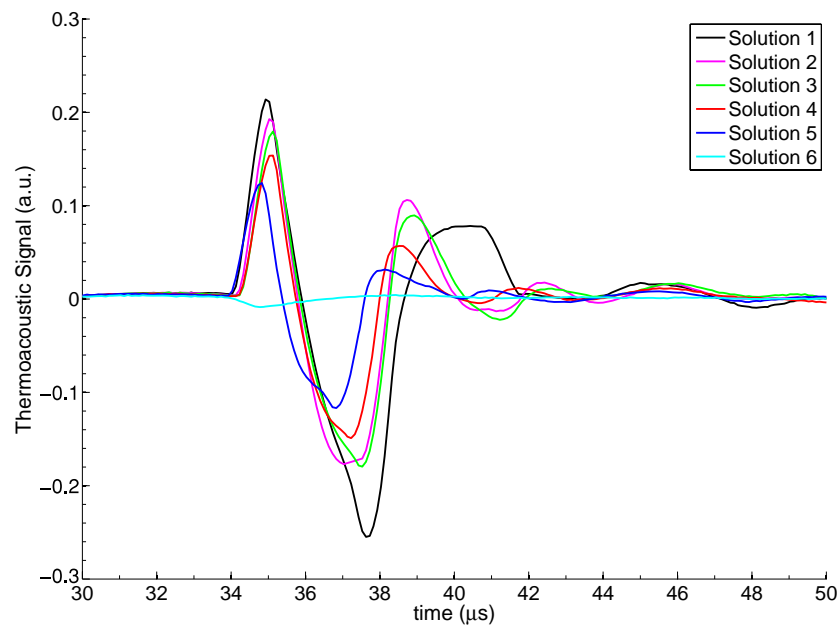


**Figure 4.** Thermoacoustic temporal waveform for all solutions.

**Table 2.** Summary of data presented in figure 4 and speed of sound measurement results.

Solution	Average amplitude of first peak in TA <sup>a</sup> waveform (a.u.)	Min/max amplitude of first peak in TA <sup>a</sup> waveform (a.u.)	Average temporal width <sup>b</sup> of TA <sup>a</sup> waveform (μs)	Speed of sound (m/s)
1	0.214	0.203/0.227	5.1	1660.7
2	0.182	0.171/0.202	3.56	1729.8
3	0.176	0.164/0.188	3.50	1805.2
4	0.149	0.138/0.155	3.28	1922.6
5	0.116	0.103/0.127	3.18	2049.4
6	≈0	≈0/≈0	2.6	NA <sup>c</sup>

<sup>a</sup> TA: Thermoacoustic.

<sup>b</sup> Measured by calculating the temporal distance between the two positive peaks in the thermoacoustic waveform.

<sup>c</sup> NA: not available.

Figure 4 and the data in table 2 show that the thermoacoustic response diminishes with increasing concentrations of microbubbles. Not only does the addition of air-microbubbles modify the dielectric properties (see figure 2), but it is also well known that gas-filled microbubbles increase acoustic attenuation due to acoustic scattering effects (Chen *et al* 2002). Therefore, it is important to distinguish whether the reduction in the initial peak of the measured thermoacoustic waveform after the addition of microbubbles is due to acoustic attenuation or dielectric properties modification. The analytic solution for the thermoacoustic impulse response of a target without acoustic attenuation has been discussed in great detail

in Wang and Wu (2007). This derivation shows that the leading edge of the thermoacoustic waveform is due to a pressure wave emitted from the target surface closest to the detector. This physical fact remains true even if the non-attenuating target medium is replaced with an acoustically lossy target. The amplitude of the acoustic disturbance from the closest target surface will not be affected by any acoustic attenuation within the target volume. Therefore, one can conclude that the observed reduction in the first peak of the thermoacoustic response with increasing concentrations of microbubbles is due to the reduced effective conductivity of the mixtures as shown by the dielectric measurements. The lower conductivity leads to smaller microwave dissipation and hence to a lower thermoacoustic response.

#### 4.3. Speed of sound measurements

Another observation from figure 4 and the data in table 2 is the reduction in temporal width of the thermoacoustic waveforms with higher concentrations of microbubbles. The temporal width of the induced thermoacoustic wave is directly related to the acoustical width of the target (Diebold *et al* 1991). As discussed in the review article by Goldberg *et al* (1993), several research groups have shown that the speed of sound of a medium decreases with increasing concentrations of gas-filled organic-shell microbubbles. Therefore, the expected trend of introducing gas microbubbles is that the thermoacoustic pulse width should widen since the speed of sound in air is much slower than the speed of sound in EG. However, in our experiments, we observed a decrease in the temporal width of the thermoacoustic waveform with increasing concentrations of microbubbles, suggesting an increase in the speed of sound in our microbubble mixtures.

This inference was confirmed with the speed of sound measurements summarized in table 2. These data show that as the concentration of microbubbles increases the speed of sound in the mixture increases as well. This is consistent with the trends observed in figure 4 and table 2 in which the thermoacoustic temporal width decreased with increasing concentration of microbubbles.

## 5. Conclusions

In these experiments we characterized the dielectric and acoustic properties as well as the thermoacoustic response of mixtures with varying concentration of air-filled glass microbubbles. Microbubbles significantly lower the microwave absorption of the target which should reduce the thermoacoustic response. These microbubbles also increase the acoustic velocity which should reduce the temporal width of the thermoacoustic response. In our thermoacoustic experiments we observed reductions of both the magnitude and temporal width of the thermoacoustic response with higher levels of microbubble concentrations. With organic-shell microbubbles one can expect the same reduction in amplitude, but a broadening of the temporal width. The changes in amplitude of the thermoacoustic response are promising enough to warrant further investigation into the use of microbubbles as a potential contrast agent in MI-TAT.

## Acknowledgments

The authors would like to thank Dr. Sarah Patch, University of Wisconsin-Milwaukee, for supporting the acquisition of the microwave generator used in the experiments and for her helpful discussions. In addition, the authors would like to thank Gary Frank for his assistance with the construction of various parts of the experimental setup, and Tomy Varghese and his

graduate students, Nick Rubert and Ryan Dewall, for their assistance with the speed of sound measurements. Finally, the authors would like to thank the reviewers for their insightful comments and suggestions. This work was supported by the National Institutes of Health under grant R01CA112398 awarded by the National Cancer Institute and the Department of Defense Breast Cancer Research Program under grant W81XWH-07-1-0629.

## References

- Calliada F, Campani R, Bottinelli O, Bozzini A and Grazia Sommaruga M G 1998 Ultrasound contrast agents: basic principals *Eur. J. Radiol.* **27** S157–60
- Chen Q, Zagzebski J, Wilson T and Stiles T 2002 Pressure-dependent attenuation in ultrasound contrast agents *Ultrasound Med. Biol.* **28** 1041–51
- Cosgrove D 2006 Ultrasound contrast agents: an overview *Eur. J. Radiol.* **60** 324–30
- Diebold G J, Khan M I and Park S M 1990 Photoacoustic signatures of particulate matter: optical production of acoustic monopole radiation *Science* **250** 101–4
- Dielbold G J, Sun T and Khan M I 1991 Photoacoustic monopole radiation in one, two and three dimensions *Phys. Rev. Lett.* **67** 3384–7
- Gabriel S, Lau R W and Gabriel C 1996 The dielectric properties of biological tissues: III. Parametric models for the dielectric spectrum of tissues *Phys. Med. Biol.* **41** 2271–93
- Goldberg B B, Liu J B and Forsberg F 1993 Ultrasound contrast agents: a review *Ultrasound Med. Biol.* **20** 319–33
- Jin X, Keho A, Meissner K and Wang L V 2007 Iron oxide nanoparticles as a contrast agent in thermoacoustic tomography *Progress in Biomedical Optics and Imaging* **8** 64370E
- Kremkau F W, Barnes R W and McGraw C P 1981 Ultrasonic attenuation and propagation speed in normal human brain *J. Acoust. Soc. Am.* **70** 29–38
- Kruger R A, Kopecky K K, Aisen A M, Reinecke D R, Kruger G A and Kiser W L 1999 Thermoacoustic CT with radio waves: a medical imaging paradigm *Radiology* **211** 275–8
- Kruger R A, Stantz K and Kiser W L 2002 Thermoacoustic CT of the breast *Proc. SPIE* **4682** 521–5
- Ku G, Fornage B D, Jin X, Xu M, Hunt K K and Wang L V 2005 Thermoacoustic and photoacoustic tomography of thick biological tissues toward breast imaging *Technol. Cancer Res. Treatment* **4** 559–65
- Lazebnik M *et al* 2007 A large-scale study of the ultrawideband microwave dielectric properties of normal, benign and malignant breast tissues obtained from cancer surgeries *Phys. Med. Biol.* **52** 6093–115
- Li X, Bond E J, Van Veen B D and Hagness S C 2005 An overview of ultrawideband microwave imaging via space-time beamforming for early-stage breast cancer detection *IEEE Antennas Propag. Mag.* **47** 19–34
- Maeda H, Wu J, Sawa T, Matsumura Y and Hori K 2000 Tumor vascular permeability and the EPR effect in macromolecular therapeutics: a review *J. Control. Release* **65** 271–84
- Meaney P M, Fanning M W, Li D, Poplack S P and Paulsen K D 2000 A clinical prototype for active microwave imaging of the breast *IEEE Trans. Microw. Theory Tech.* **48** 1841–53
- Paltauf G, Nuster R, Haltmeier M and Burgholzer P 2007 Photoacoustic tomography using a Mach–Zehnder interferometer as an acoustic line detector *Appl. Opt.* **46** 3352–8
- Popovic D, McCartney L, Beasley C, Lazebnik M, Okoniewski M, Hagness S C and Booske J H 2005 Precision open-ended coaxial probes for in vivo and ex vivo dielectric spectroscopy of biological tissues at microwave frequencies *IEEE Trans. Microw. Theory Tech.* **53** 1713–22
- Stride E and Saffari N 2005 Investigating the significance of multiple scattering in ultrasound contrast agent particle populations *IEEE Trans. Ultrason. Ferroelectr. Freq. Control* **52** 2332–45
- Tam A C 1986 Application of photoacoustic sensing techniques *Rev. Mod. Phys.* **50** 381–431
- Wang L V and Wu H-I 2007 *Biomedical Optics: Principles and Imaging* (NJ: Wiley) p 293
- Wells P N T 2006 Ultrasound imaging *Phys. Med. Biol.* **51** R83–98
- Xu M, Geng K, Xing J, Wang L V, Fornage B D and Hunt K K 2005 Breast cancer imaging by microwave-induced thermoacoustic tomography *Proc. SPIE* **5697** 45–8
- Xu M and Wang L V 2006 Photoacoustic imaging in biomedicine *Rev. Sci. Instrum.* **77** 041101

# Global modeling of carrier-field dynamics in semiconductors using EMC–FDTD

K.J. Willis · J.S. Ayubi-Moak · S.C. Hagness ·  
I. Knezevic

© Springer Science+Business Media LLC 2009

**Abstract** The interactions between carriers and fields in semiconductors at low frequencies ( $<100$  GHz) can be adequately described by numerical solution of the Boltzmann transport equation coupled with Poisson's equation. As the frequency approaches the THz regime, the quasi-static approximation fails and full-wave dynamics must be considered. Here, we review recent advances in global modeling techniques—numerical techniques that couple carrier dynamics with full wave dynamics. We focus on the coupling between the stochastic ensemble Monte Carlo (EMC) simulation of carrier transport and the finite-difference time-domain (FDTD) solution to Maxwell's curl equations. We discuss the stability and accuracy requirements for different types of high-frequency excitation (wave illumination vs. *ac* bias), and present simulation results for the THz-regime conductivity of doped bulk silicon, ultrafast carrier dynamics and radiation patterns in GaAs filaments, and the *ac* response of GaAs MESFETs.

**Keywords** Global modeling · THz conductivity · Microwave devices · EMC-FDTD · Monte Carlo simulation

## 1 Introduction

Typical doped semiconductors have plasma frequencies and characteristic carrier scattering rates in the high mi-

crowave and terahertz (THz) frequency regimes. Outside of the regime where the stimulating frequency is comparable to the carrier relaxation rate, the effects of carrier transport and electromagnetic (EM) wave propagation are sufficiently decoupled to permit independent treatment in numerical models. Accordingly, most of the recent advances and applications of charge transport solvers use simple electrostatic solvers to incorporate electric field effects [1–4]. At the same time, EM analyses use simpler bulk material models alongside full-wave electrodynamic solvers [5].

As device speeds continue to increase in step with decreasing critical dimensions, electrodynamic effects directly influence high-frequency device performance, and analyses that rely on quasi-static electric fields lose accuracy [6, 7]. Similarly, as the frequency of stimulating EM fields increases from the lower microwave range, the assumptions inherent to low-frequency material models (namely, that  $\omega\tau \ll 1$ , where  $\omega$  is the stimulating frequency and  $\tau^{-1}$  is the scattering rate) lose validity. This prominent interplay between carrier dynamics and electromagnetic wave dynamics in the sub-THz and THz regimes has been the driving force behind advancements in modeling techniques that combine a charge transport kernel with a computational electromagnetic (CEM) solver, hereafter referred to as global modeling techniques.

Interest in plasma fusion devices prompted early work into the development of global models. Pioneering work by Langdon and Dawson demonstrated for the first time the viability of an EM-particle solver [8]. Buneman's 1968 report [9] detailed the advantages of time-integrating Maxwell's equations using the Yee cell [10]. Several applications of this technique followed [11–13]. Boris gave a detailed account of the global model as it stood in 1970 [14]. Advances in the 1970s addressed self-force [15] and numerical Cherenkov

---

K.J. Willis · S.C. Hagness · I. Knezevic (✉)  
Department of Electrical and Computer Engineering, University  
of Wisconsin–Madison, Madison, WI 53706, USA  
e-mail: [knezevic@engr.wisc.edu](mailto:knezevic@engr.wisc.edu)

J.S. Ayubi-Moak  
Department of Electronics and Electrical Engineering, University  
of Glasgow, Glasgow, Scotland G12 8LT, UK



instabilities [16, 17]. The global models resulting from these and other advances are described in detail in Refs. [18–20].

The technique was limited by the computational capabilities of the era. EM calculations exhibited a continual linear increase in noise [21, 22]. Additionally, system timescales varied too greatly to include major relevant interactions without forcing a reduced speed of light and simultaneously increased electron mass. A 1980 review by Buneman et al. suggested that a 3D EM-particle tracking solver could provide qualitative insight, but quantitative results were only possible for reduced systems [23].

For a number of years after the early 1980s, particle tracking models and CEM solvers advanced more or less independently. Many of the early EM-particle reports used electromagnetic models that were clearly early finite-difference time-domain (FDTD) implementations. Researchers continued to advance FDTD; a detailed history is available in Refs. [5, 24]. The Monte Carlo technique had already been of great interest for many years, and the discipline continued to mature in this time; for a history of the ensemble Monte Carlo (EMC) technique see Ref. [25].

The need for greater efficiency and decreased memory requirements drove exploration into alternative global modeling approaches. Hydrodynamics transport models and drift-diffusion models have been used successfully in place of EMC in many cases [7, 26–35] offering decreased computational overhead [7]. Numerical simulations combining full-wave electromagnetic solutions via modern FDTD with particle-based transport models via EMC were first reported by El-Ghazaly, Joshi, and Grondin in 1990 [36]. This work provided a more accurate model of sub-picosecond carrier transport in photoconductive switches than had previously been available. A comprehensive review of the global modeling efforts of the 1980s and 1990s was conducted by Grondin, El-Ghazaly, and Goodnick [7].

Modern improvements in computer processing power have eased the restrictions on computational burden in current device and materials simulations, allowing researchers to use more computationally intensive techniques such as EMC and FDTD. Application of a combined 3D full-band cellular Monte Carlo (CMC) device simulator with a 3D full-wave FDTD solver was first demonstrated in 2003, for modeling the electromagnetic environment surrounding a simple *pin* diode [37]. This simulator was used to analyze high-frequency transistor behavior using direct capture of incident and reflected voltage waves from a full-wave analysis of a 3D MESFET device [38]. Further developments include accurate models of electron transport [39, 40] and the full-wave effects [41] in ultrasubmicrometer-gate, pseudomorphic, high-electron mobility transistors (pHEMTs). Recently, a 2D combined EMC-FDTD solver was developed and employed for high-frequency characterization of doped silicon [42, 43].

In this paper, we describe recent developments in the field of global modeling of semiconductor materials and devices, with a focus on coupled EMC-FDTD simulations. In Sect. 2, we highlight the salient features of EMC and FDTD techniques, with the assumption that the reader is not familiar with both techniques. This background overview is followed by details on the implementation of the combined EMC-FDTD, with focus on the importance of current conservation and the definition of charge assignment and current assignment schemes. The application of this global solver to doped bulk silicon characterization at THz frequencies is presented in Sect. 3. Excellent agreement between the numerically-extracted complex conductivity of doped silicon and available experimental data demonstrates the validity of the global technique for high-frequency semiconductor analysis. Section 4 describes the simulation of microwave transistors using the global CMC-FDTD model. That work uses implementation modifications necessary for *ac* device analysis, and uses a faithful description of ultrafast carrier dynamics and radiation patterns to characterize thin intrinsic GaAs filaments and GaAs MESFETs. Finally, in Sect. 5 we summarize these results and provide an outlook on the future of global modeling.

## 2 Coupled EMC-FDTD simulation

### 2.1 Ensemble Monte Carlo (EMC) simulation

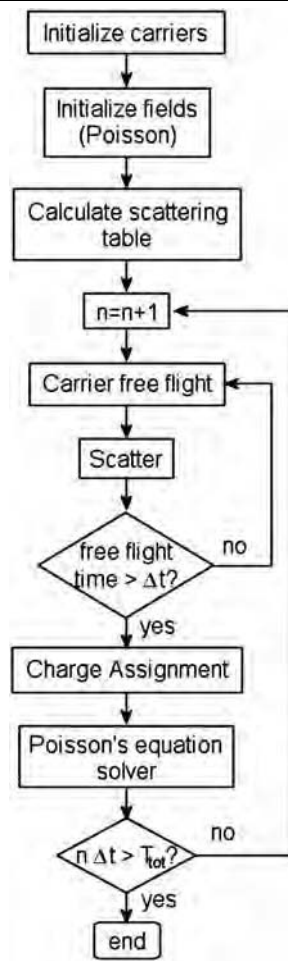
Ensemble Monte Carlo (EMC) is a powerful stochastic method used for numerical simulation of carrier transport in semiconductors in the scattering-limited (diffusive) regime [25]. It has been used for almost four decades to accurately simulate carrier transport properties of bulk semiconductors and semiconductor-based devices, and it provides a benchmark for drift-diffusion and hydrodynamics equations approaches [2]. EMC technique details are discussed below; for more information see Refs. [1–4, 18, 25, 44, 45].

On timescales longer than typical relaxation times, EMC yields the numerical solution to the Boltzmann transport equation (BTE)

$$\frac{\partial f}{\partial t} + \vec{v} \cdot \nabla_{\vec{r}} f + \vec{F} \cdot \nabla_{\vec{p}} f = \left. \frac{\partial f}{\partial t} \right|_{\text{scatter}}, \quad (1)$$

where  $f(\vec{r}, \vec{p}, t)$  is the semiclassical distribution function,  $\vec{v}$  is the carrier velocity, and  $\vec{F}$  is the total force acting on the carrier. The distribution function describes the instantaneous probability that a carrier exists with position  $\vec{r}$  and momentum  $\vec{p}$ .  $f(\vec{r}, \vec{p}, t)$  evolves in time according to (1) as a result of diffusive processes (included in the second term) and carrier drift due to external forces (described by the third term). The collision integral (described by the term on the

**Fig. 1** Flowchart of the ensemble Monte Carlo transport kernel



right hand side of the equation) describes the impact of the material-specific scattering mechanisms on the carrier ensemble.

The EMC simulates carrier dynamics in semiconductors by tracking the evolution of a large ensemble of particles [typically  $O(10^5)$ ] through time. Each carrier undergoes a series of scattering events and free flights. Free-flight momentum is updated according to the Lorentz force,

$$m^* \frac{d\vec{v}}{dt} = q(\vec{E} + \vec{v} \times \vec{B}), \quad (2)$$

where  $m^*$  is the carrier effective mass,  $q$  the carrier charge,  $\vec{v}$  the carrier velocity, and  $\vec{E}$  and  $\vec{B}$  are the electric and magnetic fields, respectively. A random number generator is used to calculate the duration of each free flight, choose the mechanism for the next scattering event, and update the particle's momentum and energy state as needed, according to the appropriate statistical probabilities. Macroscopic quantities of interest (such as charge density and drift velocity) may be readily extracted via ensemble averages.

The majority of EMC implementations employ the quasi-static assumption, where the electromagnetic period of oscillation is sufficiently long compared to carrier scattering

times that the field may be considered constant within any time step. A simplified flowchart of the general electrostatic EMC approach, self-consistently coupled to a Poisson's equation solver, is shown in Fig. 1. In this implementation, the Poisson solver calculates the grid-based scalar potential that results from the instantaneous charge density and imposed biasing conditions. Poisson solver accuracy requires a grid spacing small enough to resolve the smallest feature of interest [46], typically chosen to be between  $0.3\lambda_D$  and  $0.5\lambda_D$ . Here  $\lambda_D$  is the Debye length,

$$\lambda_D = \sqrt{\frac{\epsilon k_B T}{q^2 n_0}}, \quad (3)$$

where  $\epsilon$  is the permittivity,  $k_B$  is the Boltzmann constant,  $T$  is the temperature, and  $n_0$  the carrier density.

Stability requires that the fastest likely carrier not traverse a full grid cell over the duration of a time step,  $\Delta t$ . A second, typically more restrictive  $\Delta t$  requirement comes from the necessity to resolve plasma oscillations, in order to maintain charge balance across the testing domain and avoid charge instabilities [1]. The plasma frequency  $\omega_p$  is defined by

$$\omega_p = \sqrt{\frac{q^2 n_0}{\epsilon m^*}}. \quad (4)$$

The corresponding time step requirement is

$$\Delta t < \frac{0.5}{\omega_p}. \quad (5)$$

Note that these stability and accuracy restrictions result from the incorporation of the Poisson's equation solver; these requirements are not intrinsic to the EMC. If one is interested in resolving transient-regime transport,  $\Delta t$  should additionally be much smaller than the relaxation time ( $\Delta t \ll \tau$ ).

In the typical EMC implementation, changes in carrier energy and momentum, from individual scattering events, are calculated dynamically during the simulation. These calculations are simple for low-energy electrons where the energy is parabolic in momentum, as well as for intermediate-energy electrons where the simple first-order non-parabolic approximation accurately describes the band structure [2]. However, these simple approximations do not describe high-energy carrier dynamics well [45]. Such cases require the incorporation of the full band structure in EMC, known as the full-band Monte Carlo [47–49]. This technique provides a highly accurate description of high-field transport [44] but the added computational burden is significant.

The Cellular Monte Carlo (CMC) method, originally developed by Komater et al. [50], was designed to reduce this computational burden, but the CMC method itself requires a sizable amount of computer storage to properly maintain the required energy and momentum conservation

laws. A hybrid EMC/CMC method reduces this computational overhead, and offers a trade-off in terms of increased memory usage. The particle-based simulator used in Sect. 4 of this work is based upon the hybrid approach developed by Saraniti and Goodnick [51]. The general algorithm of the full-band device simulator follows the same steps as those previously shown in Fig. 1; now all possible initial and final states for every scattering mechanism are precomputed and stored, to be accessed during the simulation. Using the hybrid EMC/CMC (henceforth referred to as CMC for brevity), bulk material simulations have been demonstrated to run 50 times faster than with the traditional EMC method [51].

## 2.2 Finite-Difference Time-Domain (FDTD) simulation

FDTD is a highly accurate and efficient computational technique for modeling electromagnetic wave interactions with physical structures. Advances in absorbing boundary conditions, dispersive and nonlinear materials modeling, low-numerical-dispersion schemes, unconditionally stable schemes, and incident wave source conditions make FDTD a highly attractive tool for electromagnetic analysis. Some details on these advances are given here, and further information is available in Ref. [5].

FDTD is a direct numerical solution of the time-dependent Maxwell's curl equations,

$$\begin{aligned}\frac{\partial(\mu\vec{H})}{\partial t} &= -\nabla \times \vec{E} - \vec{M}, \\ \frac{\partial(\epsilon\vec{E})}{\partial t} &= \nabla \times \vec{H} - (\vec{J} + \sigma\vec{E})\end{aligned}\quad (6)$$

where  $\vec{E}$  and  $\vec{H}$  are the electric and magnetic fields, respectively,  $\epsilon$ ,  $\mu$  and  $\sigma$  are the permittivity, permeability and conductivity of the medium, respectively, and  $\vec{J}$  and  $\vec{M}$  are electric and magnetic source current densities. Note that (6) may be expressed as six coupled scalar equations, each a partial differential equation involving  $\vec{E}$ ,  $\vec{H}$ ,  $\vec{J}$ , and  $\vec{M}$  vector components.

The fully explicit FDTD algorithm is obtained by numerically approximating the spatial partial derivatives in (6) with centered finite differences, and numerically integrating the resulting system of spatial difference equations with respect to time via a centered finite-difference approximation of the temporal partial derivatives. The staggering of  $\vec{E}$  and  $\vec{H}$  in time yields an efficient leapfrog time-marching scheme wherein all of the  $\vec{E}$  components are updated at time step  $n$  (corresponding to a physical time of  $n\Delta t$ ) using previously stored  $\vec{H}$  data, and then all of the  $\vec{H}$  components are updated at time step  $n + 1/2$  using the just-computed  $\vec{E}$  data. The FDTD method does not require any formal treatment of Maxwell's divergence equations (e.g. Gauss's

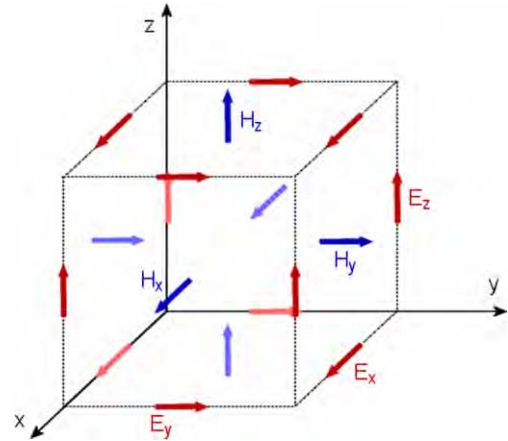


**Fig. 2** (Color online) Illustration of the staggered electric and magnetic field components about a single Yee cell in a 3D space lattice. The axis origin is positioned at index  $(i, j, k)$ , and the opposite corner has index  $(i + 1, j + 1, k + 1)$ . Each electric field component, indicated in red, is surrounded by four circulating magnetic field components. Likewise, each magnetic field component, indicated in blue, is surrounded by four circulating electric field components

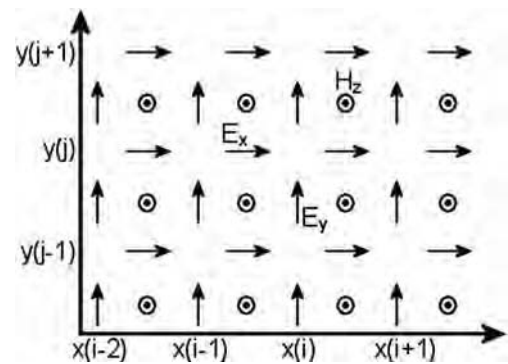


**Fig. 3** Illustration of a 2D TE<sub>z</sub> FDTD grid

Laws) because those equations are implicitly enforced by Yee's space-time grid, as shown in [5].

Figure 2 illustrates the staggered sampling of  $\vec{E}$  and  $\vec{H}$  over one grid cell of dimensions  $\Delta x$ ,  $\Delta y$ , and  $\Delta z$ , in a 3D Cartesian spatial lattice. Each vector component of  $\vec{J}$  is spatially collocated with the corresponding component of  $\vec{E}$ ;  $\vec{M}$  and  $\vec{H}$  are similarly collocated. Position within the discrete grid is defined in terms of grid indices  $(i, j, k)$ . The grid point at  $(i, j, k)$  has physical location  $[x(i), y(j), z(k)]$  where  $x(i) = i\Delta x$ ,  $y(j) = j\Delta y$ , and  $z(k) = k\Delta z$ .

If we assume all structures and fields to be  $z$ -invariant so that  $\partial/\partial z \rightarrow 0$ , we obtain a simpler two-dimensional formulation. The 2D TE<sub>z</sub> FDTD grid describes  $H_z$ ,  $E_x$  and  $E_y$ ; for most media, the other three field components decouple from these three, and may therefore be ignored for this discussion. Note that the TE<sub>z</sub> components reside on the  $x$ - $y$  plane in Fig. 3.

Electromagnetic energy may be introduced into the FDTD grid through the application of nonzero current densities,  $\vec{J}$  and  $\vec{M}$ , which may be assigned any temporal behavior in any geometrical configuration. The total-field scattered-field (TFSF) formulation applies electric and magnetic currents along a transparent closed surface within the FDTD grid [5]. This technique calculates  $\vec{J}$  and  $\vec{M}$  according to surface equivalence [52] to produce a homogeneous propagating plane wave within the closed surface. The analytic-field-propagation (AFP)-TFSF formulation is used in Sect. 3 to allow plane wave interaction with conductive material [53–55].

In open-region simulations, grid boundaries are truncated with absorbing boundary conditions such as the perfectly-matched layer (PML), which reduce reflections from the grid boundary by at least 80 dB [56, 57]. Thus, the main grid is electromagnetically isolated from the grid boundary, so that a finite grid may model an infinite space. The majority of FDTD implementations described in Sects. 3 and 4 use convolutional PML (CPML) [5, 58].

The standard FDTD method is second-order-accurate in both space and time. The algorithm exhibits numerical dispersion and conditional stability, which together constrain the choice of grid cell size and time step. Sub-wavelength sampling in space is required to properly capture the highest spatial frequencies of interest in the problem and to adequately suppress the numerical phase velocity errors. Typically, 10–20 samples per smallest wavelength of interest are needed [5]. The sampling in time is chosen to satisfy the following Courant stability condition [59]:

$$\Delta t \leq \frac{1}{v_{\max} \sqrt{\left(\frac{1}{\Delta x}\right)^2 + \left(\frac{1}{\Delta y}\right)^2 + \left(\frac{1}{\Delta z}\right)^2}}, \quad (7)$$

where  $v_{\max}$  represents the highest wave speed in the simulation domain. For a 3D lattice where  $\Delta x = \Delta y = \Delta z$ ,  $\Delta t \leq \Delta x / (v_{\max} \sqrt{3})$ , whereas for a 2D square lattice,  $\Delta t \leq \Delta x / (v_{\max} \sqrt{2})$ . As an example, consider a 3D simulation of bulk doped silicon at room temperature, with  $\epsilon_r = 11.8$ ,  $\Delta x = 20$  nm, and  $n_0 = 10^{16} \text{ cm}^{-3}$ . The Poisson solver time step restriction from (5) gives  $\Delta t_{\text{Poisson}} \leq 0.29$  ps. At the same time, FDTD stability requires  $\Delta t_{\text{FDTD}} \leq 0.13$  fs. The maximum Poisson solver time step is more than three orders of magnitude larger than the maximum FDTD time step.

If both EMC and FDTD are updated at every time step, particle positions and momenta are updated far more often than required, at the cost of a dramatic increase in the computational burden. To alleviate the burden caused by the Courant stability limit inherent to the standard FDTD technique, we use the alternating-direction-implicit (ADI)-FDTD technique in the analyses of Sect. 4. ADI-FDTD is an unconditionally stable algorithm; that is, the choice of

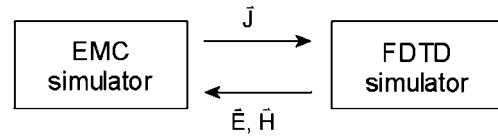


**Fig. 4** Flowchart for the combined EMC-FDTD simulation tool. The carrier transport solver (EMC or CMC) acts on field calculations via the spatially-varying current density  $\vec{J}$ . The electrodynamic solver acts on charge transport calculations via spatially-varying electric and magnetic fields  $\vec{E}$ ,  $\vec{H}$

$\Delta t$  is no longer restricted by stability requirements, but instead by much looser accuracy requirements. Details on this technique are available in Refs. [5, 60–63].

### 2.3 Coupled EMC-FDTD simulation

In the combined EMC-FDTD solver, electric and magnetic fields from FDTD influence EMC carrier motion according to the Lorentz force, (2). Microscopic currents resulting from carrier motion in the EMC influence FDTD-computed field values according to Maxwell’s curl equations, (6). A schematic of the coupling between the solvers is given in Fig. 4.

The combination of a full-wave FDTD solver with a device simulator based upon a stochastic transport kernel is conceptually straightforward, but the development and implementation of such an algorithm can be challenging, as we will see with specific examples in the following sections. Simultaneous adherence to the stability requirements of the Poisson solver and FDTD results in a heavy computational burden in the combined solver. We will describe two different approaches to this issue.

The first approach, described in Sect. 3, is appropriate to the examination of bulk materials under electromagnetic field irradiation, where charge distribution is expected to be spatially constant. If doping density is sufficiently low ( $n_0 \leq 10^{17} \text{ cm}^{-3}$ ), plasmon interactions impact material parameters only negligibly, and the Poisson’s equation solver is not necessary for the calculation. In this case, the stability requirements are only slightly modified from those of FDTD [14], and the computational burden is substantially lightened. This approach is used in Sect. 3.

The electrostatic field calculation is vital to accurate device analysis. In microwave devices a splitting of the  $dc$  and  $ac$  components and a simultaneous solution of the Poisson equation for the  $dc$  components and the FDTD solution to the  $ac$  components is necessary. Adherence to stability criteria of both solvers prolongs computation times. The second approach, described in Sect. 4, relaxes the FDTD stability requirements on  $\Delta t$  through implementation of ADI-FDTD. Computational burden is further lifted through the use of the Cellular Monte Carlo (CMC) method.

The EMC tracks carrier positions in continuous space, but most commonly used numerical electromagnetics



solvers, including FDTD and Poisson's equation solvers, calculate electromagnetic quantities at discrete grid-based locations. The quasi-static EMC-Poisson solver assumes an instantaneously electrostatic system; in Maxwell's equations  $\partial/\partial t \rightarrow 0$ . If we neglect the effect of  $\vec{H}$  on carriers, the only non-trivial equality is Gauss's law,

$$\nabla \cdot \vec{E} = \frac{\rho}{\epsilon}, \quad (8)$$

where  $\rho$  is charge density, which is incorporated in the EMC through the Poisson solver.

The EMC and the electromagnetic solver must interact through a continuous-to-discrete spatial mapping. In EMC-Poisson simulations this is called the charge assignment scheme (CAS) [4, 64]. The charge density associated with each carrier in continuous-space is assigned to discrete grid locations according to the CAS. The Poisson's equation solver uses this instantaneous charge density, along with the known permittivity, to find the grid-based electrostatic potential. Partial derivatives of the potential produce the grid-based electric field, which is then interpolated in continuous-space to determine the force on the particle, with interpolation weights identical to those in the CAS [18, 64].

The charge assignment scheme is the backbone of the simulated carrier-field interaction. Implementation of each scheme may be more or less appropriate depending on local simulation particulars; inappropriate choice of CAS may lead to non-physical electric fields at contacts and dielectric interfaces [64]. Inconsistent coupling may cause a nonphysical carrier self-force [4], where a carrier is acted on by its own potential. Minimization of these effects has driven extensive research in the application of CAS in rectangular-grid EMC-Poisson solvers [4, 64–66]. The conceptual advances resulting from this work have been invaluable in establishing the Ensemble Monte Carlo technique as the benchmark against which other computational electronics methods are gauged.

These advances were made with the assumption of a rectangular grid, with field components positioned at grid cell corners. The noncollocated field components of FDTD change the grid geometry sufficiently that it cannot be taken for granted that the results of EMC-Poisson research apply. Instead of assigning a single scalar quantity, charge, to a single grid, we must now assign the current density vector components to each of the three noncollocated grids. Early contributions to the description of current assignment schemes are given in Refs. [9, 14, 18, 21].

The electrodynamic EMC-FDTD solver assumes full time dependence of the fields, and incorporates this time dependence through Maxwell's curl equations, given in (6). This does not mean that Gauss's law no longer applies, however; Gauss's law is indeed satisfied in the EMC-FDTD by

locally enforcing current continuity, given by

$$\nabla \cdot \vec{J} = -\frac{\partial \rho}{\partial t}. \quad (9)$$

Current continuity is easily satisfied in the typical EMC-Poisson implementation. In that case,  $\rho$  and  $\vec{J}$  are calculated at the same locations on the grid, and as a result current continuity is ensured by using the same weighting scheme for the two quantities. In the EMC-FDTD implementation, however,  $\rho$  and  $\vec{J}$  are defined at separate locations on the grid. The approximations inherent to the charge and current assignment schemes mean that current continuity must be enforced explicitly.

Several current assignment schemes that ensure local charge conservation have been developed. Marder presented a modified version of Maxwell's equations to prevent violations of Gauss's law in numerical tests [67]. Villasenor and Buneman's method forced exact charge conservation in the current density calculation for simply shaped particles [68]. A generalized charge-conserving current calculation technique, for particles of arbitrary shape, was given by Esirkepov [69]. A 2005 comparison showed no difference in the quality of results between the Villasenor-Buneman method or the Esirkepov method for similar particles [70]. That study highlighted the necessity of local charge conservation in particle-in-cell codes.

Here, we describe the fundamental EMC-FDTD current assignment scheme. The method given below assumes the Villasenor-Buneman [68] current conservation technique. The reader is referred to Refs. [68–70] for implementation details. First we outline the EMC-Poisson charge assignment schemes, following the description given in Ref. [64], to establish notation and provide a basepoint for comparison. Then we detail the general EMC-FDTD current assignment scheme.

### 2.3.1 EMC-Poisson NGP and CIC schemes

The two most commonly used charge assignment schemes are the nearest-grid-point (NGP) scheme and the cloud-in-cell (CIC) scheme [1, 65, 71]. The NGP scheme treats the carrier as a  $\delta$ -function of charge: each carrier's entire charge is assigned to the nearest grid location.

In the CIC scheme, each carrier's charge is assumed to be evenly distributed over a finite region [65]. The width of this charge "cloud" may be chosen to suit the implementation; in this discussion we will assume each cloud to span one grid cell in each direction. The CIC scheme assigns each carrier's charge density among the grid points bounding the element containing the carrier; see Fig. 5. The various charge assignment schemes have different advantages, and each is appropriate under different conditions. The validity and accuracy of these schemes and others were examined in great detail

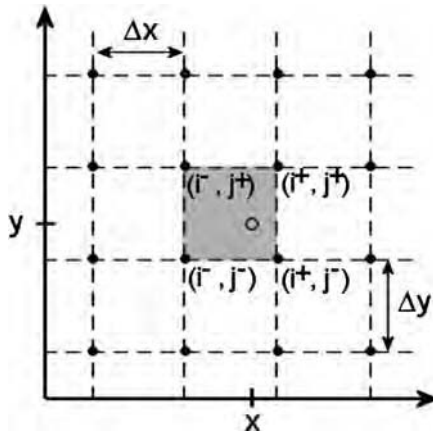


**Fig. 5** CIC schematic. The *dashed lines* show the locations of grid lines, and the *dark circles* show grid points. The *open circle* indicates a carrier located at  $(x, y)$ . In the CIC scheme, the carrier is assumed to have charge spread over a finite region, shown by the *grey square*. In this 2D example, the grid element containing the carrier is bounded by four grid points, with indices  $(i^\pm, j^\pm)$

in references [64, 65]. Improvements and various nuances of implementation were described in Ref. [64].

In this discussion, we examine only the 2D case; extension to the 3D mesh is straightforward. Consider a carrier with charge  $q$  positioned at  $(x, y)$  in continuous space, as shown in Fig. 5. We define in the  $x$ - $y$  plane a corresponding uniform mesh,  $(i, j)$ , where  $i \in [1, N_i]$  and  $j \in [1, N_j]$ . The grid spacing is given by  $\Delta x$  in the  $x$ -direction and  $\Delta y$  in the  $y$ -direction. The volume of one grid cell is  $V = l\Delta x\Delta y$ , where  $l$  is the assumed domain depth in the  $z$ -direction.

We define  $i^+$ ,  $i^-$ ,  $j^+$  and  $j^-$  as the indices of the grid points at the corners of the cell that contains the carrier (Fig. 5).  $w(i, j)$  is the charge-assignment weight at grid point  $(i, j)$ , and the grid position is as described in Sect. 2.2. For the CIC scheme, the distribution weights are given by

$$\begin{aligned} w(i^-, j^-) &= w_x w_y, \\ w(i^+, j^-) &= (1 - w_x) w_y, \\ w(i^-, j^+) &= w_x (1 - w_y), \\ w(i^+, j^+) &= (1 - w_x) (1 - w_y), \end{aligned} \quad (10)$$

where

$$\begin{aligned} w_x &= \frac{x(i^+) - x}{x(i^+) - x(i^-)} = \frac{x(i^+) - x}{\Delta x}, \\ w_y &= \frac{y(j^+) - y}{y(j^+) - y(j^-)} = \frac{y(j^+) - y}{\Delta y}. \end{aligned} \quad (11)$$

Note that charge conservation dictates  $\sum_{i^\pm, j^\pm} w(i, j) = 1$ .

**1. Charge assignment:** The point charge density  $q/V$  is assigned to the grid, producing a grid-based charge density  $\rho_{i,j}$ . In NGP the entire charge  $q$  is assigned to the

nearest grid point, so that one of the  $w(i, j)$  in (10) has value one and the rest have value zero. In CIC, we allow  $i = \text{floor}(x/\Delta x)$  and  $j = \text{floor}(y/\Delta y)$ , and use  $i^\pm = i + 1/2 \pm 1/2$  and  $j^\pm = j + 1/2 \pm 1/2$  in (10) and (11). In both schemes, we add  $qw(i, j)/V$  to  $\rho_{i,j}$  for all  $(i, j)$ .

- 2. Find the electrostatic solution:** Starting with  $\rho_{i,j}$  and  $\epsilon$ , Poisson's equation gives the grid-based potential  $\phi_{i,j}$ .
- 3. Calculate grid-based  $\vec{E}$ :** The electric field is calculated on each mesh point  $(i, j)$  as  $E_{i,j}^x = -(\phi_{i+1,j} - \phi_{i-1,j})/(2\Delta x)$  and  $E_{i,j}^y = -(\phi_{i,j+1} - \phi_{i,j-1})/(2\Delta y)$ .
- 4. Interpolate:** In NGP, the field acting on the carrier is assumed to be that at the nearest grid location. In CIC,  $\vec{E}(x, y)$  is found using the  $w(i, j)$  calculated for step 1:

$$E^x(x, y) = \sum_{i^\pm, j^\pm} w(i, j) E_{i,j}^x$$

and

$$E^y(x, y) = \sum_{i^\pm, j^\pm} w(i, j) E_{i,j}^y.$$

The NGP scheme is computationally simple, but inaccuracies are introduced because the NGP scheme effectively shifts the carrier position to the nearest grid location for all electromagnetic interactions. Additionally, this scheme does little to counteract local charge density fluctuations resulting from a finite carrier ensemble size [1, 65].

CIC is computationally more intensive than NGP, but it vastly improves smoothing of local charge density fluctuations, often permitting smaller ensemble sizes and a decreased overall computational burden. CIC has been shown to produce nonphysical fields at metal contacts, however, and therefore must be used judiciously [64, 65].

### 2.3.2 EMC-FDTD NGP and CIC schemes

Consider a point charge with the current density contribution  $\vec{J} = (J_x, J_y)$  located at  $(x, y)$  in a 2D FDTD mesh, as shown in Fig. 6. The computational grid shown incorporates  $H_z$ ,  $E_x$ , and  $E_y$  fields. Because the  $J_x$  and  $J_y$  components are noncollocated in the FDTD formulation, the problem is not straightforward. The  $x$ - and  $y$ -current densities must be considered independently.

Assume a CIC scheme with a rectangular charge cloud of height  $\rho = q/V$ . A carrier moves from  $r_n = (x_n, y_n)$  to  $r_{n+1} = (x_{n+1}, y_{n+1})$  over a single time step  $\Delta t$ . For now we assume  $r_n$  and  $r_{n+1}$  are in the same grid cell, and the cell is bound by indices  $(i, j)$  and  $(i + 1, j + 1)$ . Then, the Villasenor-Buneman method [68] defines the current density contribution of that carrier by

$$J_{i+\frac{1}{2},j}^x = \frac{\rho l}{\Delta t} (x_{n+1} - x_n) \left( j + 1 - \frac{y_{n+1} + y_n}{2\Delta y} \right),$$

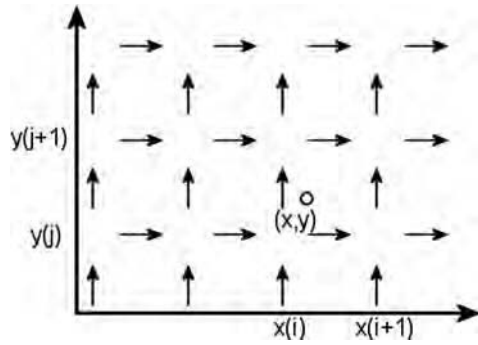


**Fig. 6** The carrier at  $(x, y)$  in the staggered FDTD grid. Only the  $E_x$  and  $E_y$  field components are shown

$$\begin{aligned} J_{i+\frac{1}{2},j+1}^x &= \frac{\rho l}{\Delta t} (x_{n+1} - x_n) \left( \frac{y_{n+1} + y_n}{2\Delta y} - j \right), \\ J_{i,j+\frac{1}{2}}^y &= \frac{\rho l}{\Delta t} (y_{n+1} - y_n) \left( i + 1 - \frac{x_{n+1} + x_n}{2\Delta x} \right), \\ J_{i+1,j+\frac{1}{2}}^y &= \frac{\rho l}{\Delta t} (y_{n+1} - y_n) \left( \frac{x_{n+1} + x_n}{2\Delta x} - i \right). \end{aligned} \quad (12)$$

If the carrier passes through a grid cell boundary (or two boundaries, if the carrier is located at the corner of a grid cell), the current calculation is split into two (or three) parts, where each part is used to find the carrier's current contribution within each cell. See Refs. [68, 70] for further details. If  $\vec{J}$  is defined in this manner, current continuity is ensured.

- 1. Current assignment:** The current density of the particle is calculated from the change in the particle position over  $\Delta t$ .  $J_{i+1/2,j}^x$ ,  $J_{i+1/2,j+1}^x$ ,  $J_{i,j+1/2}^y$  and  $J_{i+1,j+1/2}^y$  are calculated according to (12) and the procedures given in Refs. [68–70].
- 2. Find the electrodynamic solution:** Using  $J_x$ ,  $J_y$  and  $\epsilon$ , FDTD gives the electric and magnetic fields  $E_x$ ,  $E_y$  and  $H_z$ .
- 3. Interpolate field:** It is necessary to spatially average the electric fields so that they are known at the grid intersections, in order to avoid particle self-force [70].  $E_{i,j}^x = (E_{i+1/2,j}^x + E_{i-1/2,j}^x)/2$  and  $E_{i,j}^y = (E_{i,j+1/2}^y + E_{i,j-1/2}^y)/2$ . The electric field at the carrier's location  $(x, y)$  is found by interpolating between the nearest grid points following the same procedure as that used in the CIC charge assignment scheme.

### 3 THz conductivity of doped bulk silicon

The plasma frequency and characteristic scattering rate of moderately doped semiconductors typically fall within the THz regime [72]. For this reason, semiconductor carrier response to THz-frequency stimulation depends strongly on the specific form of the material transport parameters. The

bulk materials behavior in the THz-range is extremely sensitive to small deviations in doping density and temperature [73, 74].

In this section, we explore the use of the global EMC-FDTD solver in the context of doped bulk silicon materials characterization. First, for reference, we review THz-regime experimental characterizations of doped silicon in Sect. 3.1. Then in Sect. 3.2 we describe the specific coupled EMC-FDTD solver used to simulate THz-frequency electromagnetic plane wave interactions with doped bulk silicon, and the method we use to extract the frequency-dependent effective conductivity from the computed fields and currents. We examine simulation performance in the context of predicted conductivity convergence under variation in grid cell size, ensemble size, averaging technique, and impedance mismatch. Finally, we compare the simulation results—that is, the predicted effective conductivity—with published experimental results for doped silicon at THz frequencies.

#### 3.1 Experimental characterization

Since the advent of THz time-domain spectroscopy (THz-TDS) 20 years ago, extensive experimental work has examined the THz characteristics of doped bulk silicon [72–84]. Pure undoped silicon is almost completely transparent and nondispersive under THz-frequency radiation, more so than quartz, sapphire, or fused silica, making silicon a very attractive THz-optics material [73]. However, this behavior is only observed in extremely pure samples. Carriers introduced by low-level doping and impurities strongly impact the THz-frequency materials characteristics of silicon [73]. As doping density is increased, silicon becomes quite opaque to THz radiation [72]. Because pure silicon is extremely transparent, it is reasonable to assume that carrier-field dynamics within doped silicon are solely responsible for doped silicon's opacity under THz radiation [73].

The seminal THz-TDS characterizations extracted the complex transmission spectrum of semiconductor samples through the use of freely-propagating THz beams. The high accuracy of this technique is mainly limited by uncertainties in sample thickness that lead to minor uncertainties in the transmission amplitude, and comparatively large ( $\sim 10\%$ ) uncertainties in the phase [72].

As carrier density increases to around  $10^{17} \text{ cm}^{-3}$ , the increased opacity of silicon precludes transmission-based characterization [79]. The development of reflection-based THz-TDS in 1996 [85] has since permitted extensive study of optically dense media [74, 79]. In reflecting THz-TDS the exact placement and orientation of the sample is critically important. In analogy to uncertainties from sample thickness in transmission THz-TDS, here small deviations in sample position contribute to uncertainty in the reflection spectrum amplitude and larger uncertainties in phase. This

**Table 1** Summary of experimental results on doped bulk silicon under THz radiation, as obtained from THz-TDS, chronologically ordered. Values in bold were calculated for comparison purposes, based on data from the referenced work. The table shows the conductivity model assumed in the original work; the material *dc* characteristics including

resistivity, doping density, and mobility; the fitted THz characteristics including doping density and mobility; the percent change from *dc* to THz doping density and mobility values, and the data citation. In most cases, both  $n_0$  and  $\mu$  are taken as fitting parameters; Ref. [82] assumes known  $\mu$  for all calculations.

Model	<i>dc</i>			THz		$\Delta n_0$ %	$\Delta \mu$ %	Ref.
	$\rho$ ( $\Omega$ cm)	$n_0$ ( $\text{cm}^{-3}$ )	$\mu$ ( $\text{cm}^2/\text{V s}$ )	$n_0$ ( $\text{cm}^{-3}$ )	$\mu$ ( $\text{cm}^2/\text{V s}$ )			
Drude	1.15	$4.6 \times 10^{15}$	<b>1302</b>	$3.3 \times 10^{15}$	1680	28	−29	[77]
Drude	8.1	$7.0 \times 10^{14}$	<b>1349</b>	$4.2 \times 10^{14}$	1820	40	−35	[72]
Drude	8.15	<b><math>5.2 \times 10^{14}</math></b>	<b>1352</b>	$3.4 \times 10^{14}$	2340	34	−73	[78]
Drude	0.21	<b><math>3.2 \times 10^{16}</math></b>	<b>1083</b>	$2.1 \times 10^{16}$	1420	34	−31	[78]
Cole-Davidson	8.15	<b><math>5.2 \times 10^{14}</math></b>	<b>1352</b>	$4.0 \times 10^{14}$	2000	23	−47	[78]
Cole-Davidson	0.21	<b><math>3.2 \times 10^{16}</math></b>	<b>1083</b>	$2.3 \times 10^{16}$	1280	28	−18	[78]
Drude	1.1	$3.8 \times 10^{15}$	1350	$4.9 \times 10^{15}$	1350	−29	0	[82]
Drude	2.5	$1.7 \times 10^{15}$	1350	$1.8 \times 10^{15}$	1350	−6	0	[82]
Drude	10.0	$4.2 \times 10^{14}$	1350	$6.7 \times 10^{14}$	1350	−59	0	[82]
Drude	1.1	$4.1 \times 10^{15}$	<b>1306</b>	$3.7 \times 10^{15}$	1560	12	−19	[74]
Drude	0.14	$4.0 \times 10^{16}$	<b>1036</b>	$3.5 \times 10^{16}$	1280	14	−17	[80]

uncertainty may be minimized by analytically sweeping the relative positions of sample and reference plane; see, for example, Ref. [79]. While careful implementation of reflecting THz-TDS produces excellent results, the sensitivity of the technique has prompted research into other THz-regime characterization methods [81–84].

In summarizing available experimental results on the THz characteristics of doped silicon, we consider only those reports which provide sufficient data for comparison: the room temperature *dc* resistivity or assumed equivalent doping density, as well as THz-range fitting doping density or plasma frequency [72, 74, 77–81]. These data are shown in Table 1. In nearly every case, these results were extracted from observed reflection and transmission spectra assuming Drude model behavior, where the Drude model conductivity is given by

$$\sigma = \frac{\epsilon_0 \omega_p^2 \tau}{1 - i\omega\tau}. \quad (13)$$

$\tau$  is the characteristic carrier scattering time and  $\omega_p$  is the plasma frequency. If we consider only the data in Table 1 in which carrier density and mobility are taken as fitting parameters, the fit to the Drude model requires assumed doping densities that average  $\sim 27\%$  lower than those calculated from the known *dc* resistivity, and calculated mobilities  $\sim 32\%$  higher than those found at *dc*. This suggests that  $\tau$  energy-dependence sufficiently impacts THz-frequency properties that it must be accounted for by the conductivity model [72]. Several other models have been developed to incorporate  $\tau$  energy dependence, with promising results [72, 78].

The ill-fit of the Drude model to doped silicon at THz frequencies, and the absence of another well-accepted model, makes prediction of THz-frequency materials properties of arbitrarily doped silicon difficult. As demonstrated below, the EMC-FDTD method has the potential to provide detailed materials characterization of doped silicon at THz frequencies.

### 3.2 Simulation domain

For both EMC and FDTD we use two-dimensional (2D) computational domains defined in the  $x$ – $y$  plane (Fig. 8). The EMC domain is filled with (001) doped silicon with doping density  $n_0 = 10^{17} \text{ cm}^{-3}$ . The typical simulation carrier ensemble size is  $O(10^5)$ . To permit examination of the interaction between these carriers and propagating THz-frequency electromagnetic plane waves, we embed the EMC domain into an FDTD domain.

The FDTD simulation testbed is a semi-infinite half space of doped silicon (Regions B and C in Fig. 8) and a semi-infinite half space of air (Region A in Fig. 8). Region A is assigned a dielectric constant of 1 and zero conductivity. A dielectric constant of 11.8 is assigned to Regions B and C. Region C is filled with an assumed value for the continuous bulk *dc* conductivity of doped silicon,  $\bar{\sigma}$ . Region B contains the embedded EMC domain; the current  $\vec{J}$  in (6) is generated solely from the EMC.

The EMC formulation accounts for the smooth material interface by enforcing specular reflection of carriers at the left and right boundaries of the domain. The top and bottom boundaries are given periodic boundary conditions, to allow unrestricted carrier motion in the vertical direction.



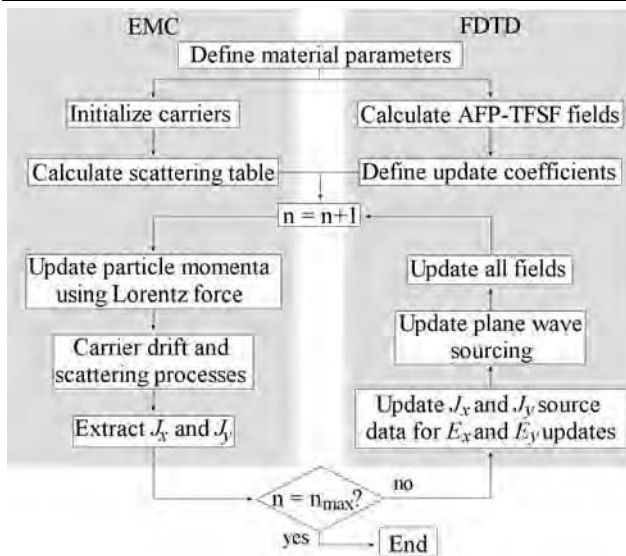


**Fig. 7** Flowchart for the combined EMC-FDTD simulation modeling tool

Care must be taken at the edges of the coupled region to ensure that EMC current density does not extend beyond the coupled region for any charge assignment scheme.

To allow finite-grid representation of an infinite space, we treat FDTD domain boundaries with CPML absorbing boundary conditions [5, 58]. Outward-propagating waves that reflect from the domain boundary are attenuated within the CPML by more than 80 dB, so that the main grid is electromagnetically isolated from the domain boundary to very good approximation. We assume a TE<sub>z</sub> mode for the electromagnetic wave. Plane waves are introduced with a propagation direction normal to the interface via the AFP-TFSF formulation [53–55]. In this polarization, the incident plane wave will excite *y*-directed currents within the EMC-coupled region. The periodic boundaries on the top and bottom edges of the EMC domain and the uniform incident field allow bulk EMC simulation within the finite domain. Figure 7 shows the full simulation flowchart for a coupled EMC-FDTD solver.

Figure 8 shows the 2D spatial distribution of the  $E_y$  phasor amplitude, extracted via discrete Fourier transform over several periods of electromagnetic wave oscillation. The field amplitude is attenuated as a function of depth in both Regions B and C. Amplitude decay in region C corresponds to that expected for a dielectric with conductivity  $\bar{\sigma}$ . No conductivity is enforced in the coupled Region B; field decay in this region results from the carrier-field interaction, exhibiting the macroscopic phenomenon of the skin effect.

Noise in the  $E_y$  phasor amplitude in Region B is caused by thermal electron motion;  $E_x$ ,  $J_x$  and  $J_y$  also exhibit minor fluctuations in phase and amplitude. Transient fields, continually sourced by this noise, propagate to the grid boundary and are attenuated in the CPML. Without high-

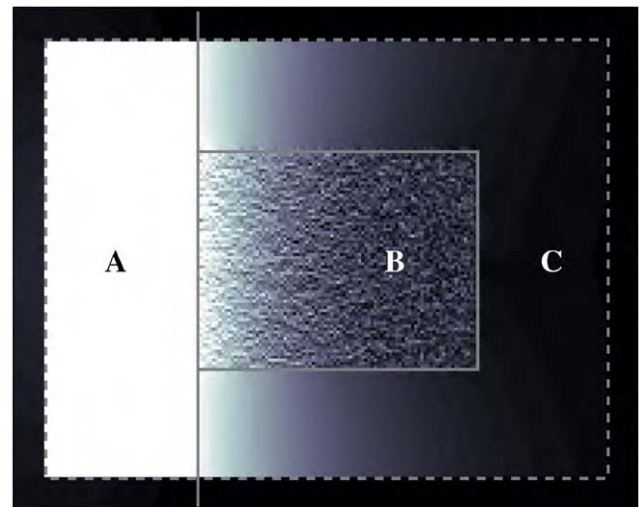


**Fig. 8** Amplitude of  $E_y$  field phasor extracted by DFT over several periods of electromagnetic wave oscillation, where white corresponds to high field amplitude and black corresponds to low field amplitude. The materials interface is indicated by the vertical gray line. The section of the domain shown here lies within the AFP-TFSF boundary; an incident plane wave is sourced from the left boundary. Region B is the EMC-FDTD coupled region, whose boundary is marked by a solid gray box, and Regions A and C are pure-FDTD doped silicon

quality absorbing boundary conditions these simulations would suffer from the same continually increasing noise level that affected the early simulations described in Sect. 1. To reduce the impact of this noise on conductivity calculations, we take spatial averages over small regions surrounding each grid location in the extracted phasor quantities. Increasing the size of the averaging regions decreases phasor quantity noise. The averaging region size must not be increased beyond  $\sim 1/20$ th of the smallest electromagnetic feature of interest.

These noise-reduced phasor quantities are used in the effective linear-regime conductivity calculation,

$$\check{\sigma}(\omega) = \frac{\vec{E}(\omega) \cdot \vec{J}^*(\omega)}{|\vec{E}(\omega)|^2}. \quad (14)$$

The real part of  $\check{\sigma}$  corresponds to power dissipation and is evidenced as the phasor amplitude decay in Fig. 8. The imaginary part of  $\check{\sigma}$  corresponds to phase shift between  $\vec{E}$  and  $\vec{J}$  resulting from the delay in material response to applied fields. As the electromagnetic oscillation frequency approaches the carrier scattering rate, we expect the delay in material response to applied fields to increase.

Figure 9 shows the variance of  $|E_y|$  in Region B as a function of electron ensemble size  $N_e$  for several grid cell sizes  $\Delta x$ . As expected, larger carrier ensembles show decreased phasor quantity noise, at the cost of an increased computational burden. Figure 9 shows dramatic noise reduction for increased  $\Delta x$ . This improvement directly contrasts

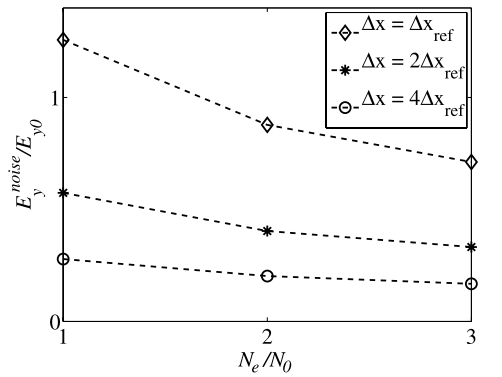


**Fig. 9** Average noise of  $E_y$  in the EMC-FDTD coupled region for several values of electron ensemble size and grid cell size.  $E_y^{\text{noise}}$  is calculated as  $\sqrt{\langle |E_y|^2 \rangle - \langle E_y \rangle^2}$  and is normalized by  $|E_y|$  at the material interface.  $\Delta x_{\text{ref}} \approx 400 \text{ nm}$  is a reference grid cell size. Increasing the size of the ensemble reduces noise, as expected, but increasing the grid cell size produces a much larger improvement

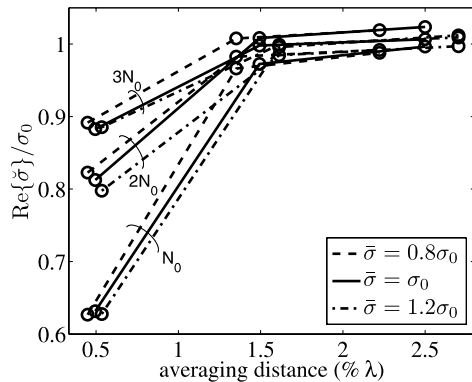


**Fig. 10** Extracted conductivity with varied averaging region size, electron ensemble size, and surrounding bulk conductivity.  $N_0$  is a reference ensemble size, typically  $O(10^5)$ . Larger averaging region size leads to convergence in  $\bar{\sigma}$ . Level of impedance mismatch between Regions B and C, examined through modified  $\bar{\sigma}$ , is associated with line type. See text for discussion

the EMC-Poisson solver accuracy requirements, which favor smaller grid cells for improved electrostatic calculations. The EMC-FDTD solver achieves significant noise reduction for larger  $\Delta x$  by including a larger number of carriers in each  $J_x$  and  $J_y$  grid point calculation.

Figure 10 shows  $\bar{\sigma}$  as a function of phasor quantity averaging region size, for several values of ensemble size and several levels of impedance mismatch between Regions B and C. As the averaging regions size is increased,  $\bar{\sigma}$  converges. Increased ensemble size also leads to convergence in  $\bar{\sigma}$ , indicating correspondence between decreased phasor quantity noise and convergence in  $\bar{\sigma}$ .

Finally, Fig. 10 allows examination of the impact of impedance mismatch between the EMC-FDTD coupled Region B and the surrounding pure-FDTD Region C. In any single test, the conductivity  $\bar{\sigma}$  defined in Region C may not

match the conductivity exhibited by the EMC-FDTD coupled region. The resulting impedance mismatch will cause waveguiding and back-reflections within the coupled region. We tested the effect of these reflections on  $\bar{\sigma}$  by comparing extracted conductivity values for several tests where  $\bar{\sigma}$  was varied through three values, spanning  $\bar{\sigma}$ . Figure 10 shows the results of this experiment;  $\bar{\sigma}$  is insensitive to impedance mismatch between Regions B and C.

### 3.3 Comparison with experiment

We compare the complex  $\bar{\sigma}$  with experimental results obtained via reflecting THz-TDS [78]. The  $dc$  resistivity of the n-type doped silicon sample used is given as  $8.15 \Omega \text{ cm}$ , corresponding to  $n_0 \approx 5.5 \times 10^{14} \text{ cm}^{-3}$  [86]. This doping density is used in the EMC-FDTD solver, and the pure-FDTD  $\bar{\sigma}$  is modified to match the corresponding  $dc$  conductivity.

The analytical best fit of the Cole-Davidson model to experimental data is given by Jeon and Grischkowsky [78]. The Cole-Davidson fit can be regarded as a faithful representation of the experimental data. Figure 11 compares the EMC-FDTD-extracted doped-silicon conductivity to the best fit to experimental results. The global solver provides results which agree well with experiment. The real part of the conductivity shows excellent agreement, especially at higher frequency. The imaginary component of the conductivity shows good agreement, even though small phase errors in the computationally and experimentally extracted conductivities would show up here. In the numerical tests,  $n_0$  is sufficiently low that the binary Coulomb interactions between individual carriers should not substantially contribute to the observed conductivity, but because the plasma frequency  $\omega_p$  is  $O(\text{THz})$ , plasmon scattering may be important.

This preliminary work on a combined EMC-FDTD solver demonstrates its utility in characterization of doped semiconductors at THz and sub-THz frequencies. We have shown that this global numerical technique provides conductivity predictions that match well to experiment. The EMC-FDTD solver exhibits improved accuracy for larger  $\Delta x$ , in contrast to traditional EMC-Poisson accuracy requirements. The EMC-FDTD global solver shows promise as a method for full characterization of doped silicon at THz frequencies.

## 4 Global modeling of microwave transistors

Microwave semiconductor device analysis in the small-signal regime requires a full description of the quasi-static  $dc$  field distribution prior to the application of a small  $ac$  modulation. In the global model developed recently by Ayubi-Moak et al. [37–41],  $dc$  device behavior is obtained first, as the steady-state result of the CMC-Poisson simulation at a given bias point. The calculated  $dc$  current,  $\bar{J}_{dc}$ , is

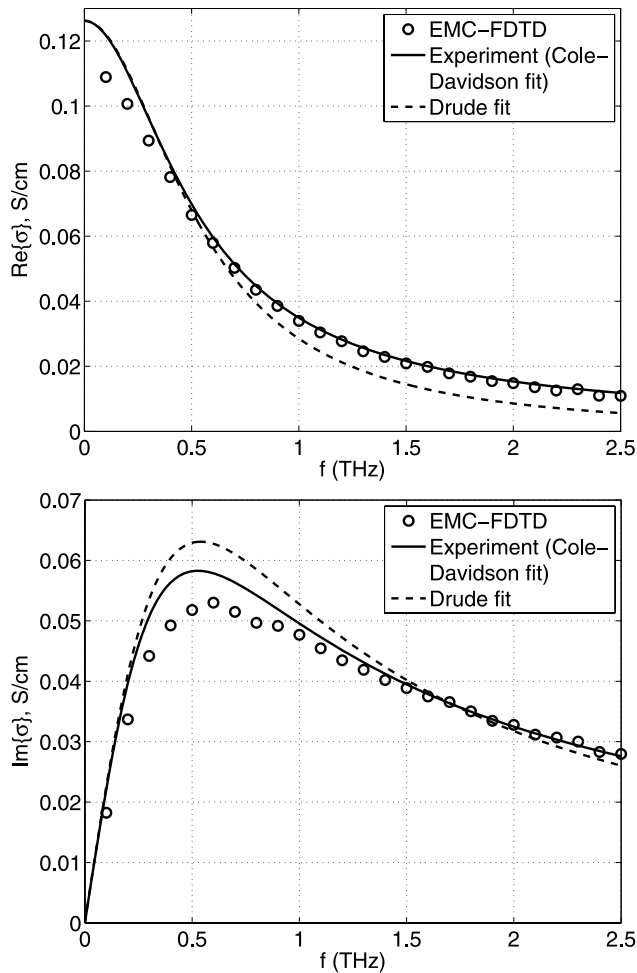


**Fig. 11** THz conductivity of doped bulk silicon. The EMC-FDTD conductivity (circles) agrees well with the experimental data of Ref. [78] (presented here via a faithful Cole-Davidson analytical fit, solid curve)

used to source the  $dc$  Maxwell's curl equations,

$$\nabla \times \vec{E}_{dc} = 0, \quad (15a)$$

$$\nabla \times \vec{H}_{dc} = \vec{J}_{dc}. \quad (15b)$$

An  $ac$  excitation source is then applied to the device via a source plane approach described in the next section. The resulting time-varying distributions of the EM fields are then computed by solving the discretized Maxwell's equations over the entire FDTD grid (repeated here for convenience)

$$\frac{\partial \vec{H}}{\partial t} = -\frac{1}{\mu_0 \mu_r} (\nabla \times \vec{E}), \quad (16a)$$

$$\begin{aligned} \frac{\partial \vec{E}}{\partial t} &= \frac{1}{\epsilon_0 \epsilon_r} (\nabla \times \vec{H}) \\ &= \frac{1}{\epsilon_0 \epsilon_r} (\nabla \times \vec{H}_{ac} + \vec{J}_{dc} - \vec{J}_{total}), \end{aligned} \quad (16b)$$

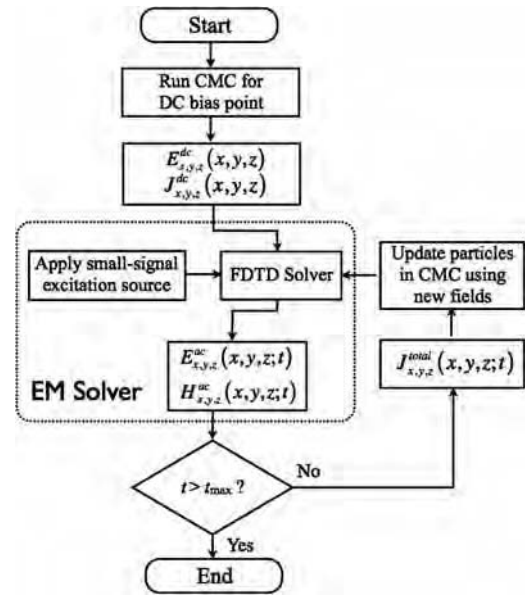


**Fig. 12** Flowchart of coupled CMC/FDTD device simulator [38]

where  $\vec{J}_{total}$  is now the total current density (i.e. the  $ac$  part plus the  $dc$  part) computed by the CMC solver after a specified number of particle free-flight time steps. In (16a) and (16b), a lossless medium has also been assumed for simplicity. Note that during the first FDTD time step of the full-wave simulation in which the  $ac$  excitation is applied,  $\vec{J}_{total}$  is exactly equal to  $\vec{J}_{dc}$ .

Following the individual update of each field component, the new  $ac$  fields are then added to the stored  $dc$  fields and the updated total field is passed back into the CMC solver and used to compute the total Lorentz force, evolve the particle velocities, and recalculate the total current. Once computed, the new current density in each grid cell is passed back to the FDTD solver at the next full-wave time-step and the process is repeated for the remainder of the full-band/full-wave simulation, as illustrated in Fig. 12.

A critical component in the full-wave simulation is the manner in which small-signal voltage perturbations are applied to the electrodes on the FDTD grid. This can be accomplished by applying the proper transverse electric field distribution to a source plane at the front end of the simulation domain. The applied electric field distributions correspond to the solution of Poisson's equation over a 2D source plane for a set of applied contact voltages. This static field distribution is then modulated by the appropriate time signature of the desired excitation function. The resulting distributions are then applied as soft sources to the corresponding field components at each FDTD time step during the full-wave portion of the total simulation.

The source plane is located along a cross-section of the 3D structure, as illustrated in Fig. 13, for a simple coplanar waveguide (CPW) geometry. The FDTD grid is extended

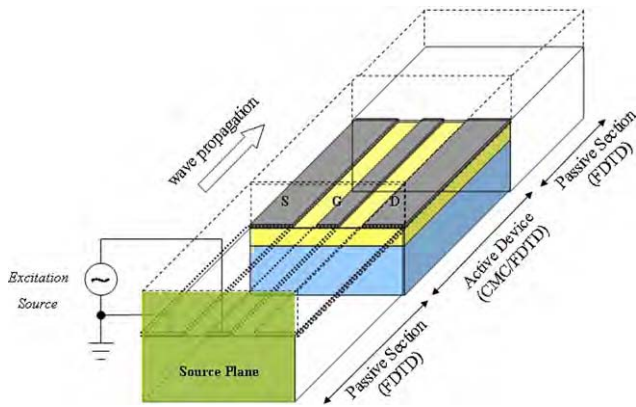


**Fig. 13** Example of simulation domain used in a 3D CMC/FDTD simulation showing passive and active sections

both in the front of and to the back of the actual active device region. Both the passive front-end and back-end sections function as lossless transmission lines. The passive front-end section allows the sourced excitation wave to develop into the proper waveguide mode prior to its interaction with the active device. Both passive sections are defined as extensions of the intrinsic undoped semiconductor material beyond the physically modeled electrode terminations in the CMC simulator. The passive sections separate the active CMC device model from the CPML layers (not shown in figure) which truncate the domain. The domain region above the active device and passive regions is filled with free space and separates the top of the circuit from the upper absorbing boundary layer. The excitation source in Fig. 13 is applied to the gate electrode of a simple three-terminal device. In this illustration, the source electrode is grounded and the drain is left floating (i.e. not grounded). The excitation signal is shown being applied to the gate. Not shown in the figure is the ground plane located directly below the substrate.

#### 4.1 Ultrafast device simulation and results

The first direct measurement of femtosecond velocity overshoot in GaAs and InP was performed by Leitenstorfer et al. [87], by capturing transient THz radiation produced by optically-generated electron-hole pairs in *pin* diodes. This work motivated the subsequent numerical results of the transient response in GaAs and InP by Wigger et al. [88], which used CMC/Poisson transient simulation (basically, the transient electric field was assumed to satisfy Poisson's equation at every point in time, and magnetic field was neglected). Here we present the application of the coupled CMC/FDTD to the simulation and capture of radiated EM fields emanating from ultrafast, high-frequency devices [37].

The test structure was a 3D slice of intrinsic GaAs 500 nm long and 100 nm wide in both transverse dimensions. Contacts were simulated on each end of the structure allowing for the necessary reverse bias across the *pin* diodes

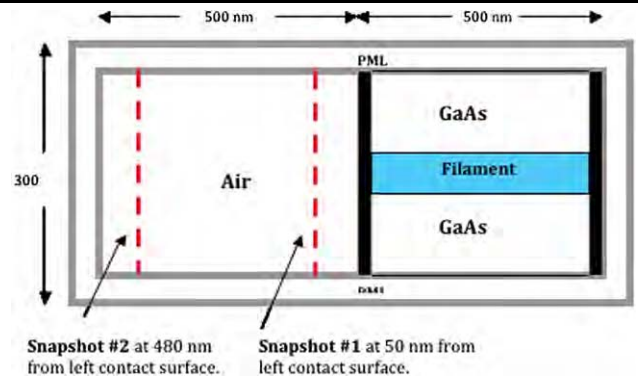


**Fig. 14** Cross-section of the structure used in the THz simulations

used in the original experiments in [87]. A 500 nm long air region was added to the left end of the structure and the entire simulated domain was surrounded by a split-field perfectly matched layer (PML) absorbing boundary region ten cells thick in each direction. A 500 nm long square filament with a cross-sectional area of  $400 \text{ nm}^2$  was centered inside the GaAs region. This filament represented the region over which simulated electron-hole pairs were injected into the device structure. Figure 14 shows a 2D cross-section of the test structure. This device was simulated using a uniform mesh of 10 nm spaced grid cells. This spatial dimension allowed for a maximum time step of only 0.0016 fs and was the limiting factor in these simulations.

Two sets of simulations were performed on the test structure. Both simulations were run for a total of 350 fs. In each case, 25,000 electron-hole pairs were injected into the filament region of the device with a peak injection concentration of  $5 \times 10^{-14} \text{ cm}^{-3}$  occurring 20 fs after the start of the simulation. In the first experiment, a bias of  $-5 \text{ V}$  was applied across the device, corresponding to a uniform electric field of 100 kV/cm. In the second experiment, the bias voltage was decreased to  $-1.2 \text{ V}$ , corresponding to a uniform electric field of 24 kV/cm. Because each simulation demonstrated a similar set of results, only the details of the 100 kV/cm simulation are presented and discussed here.

During runtime, snapshots of the electric and magnetic field components were taken over a cross section of the  $y$ - $z$  plane at distances of 50 nm (Fig. 15) and 480 nm (Fig. 16) from the left contact. These points were chosen in order to capture the near and far-field characteristics of the electric fields surrounding the device. In Fig. 15, a snapshot of the  $E_y$  field was taken approximately 1.25 fs after the peak of the injection pulse. It is clear from the contour plot that the field is dipolar in nature. This behavior is actually the expected response from an elemental oscillating electric or Hertzian dipole in which the magnitude of the electric field intensity is directly proportional to the dipole moment in the longitudinal direction. Under the influence of a high, uniform electric field, electrons and holes are accelerated in opposite directions, creating an electric dipole with



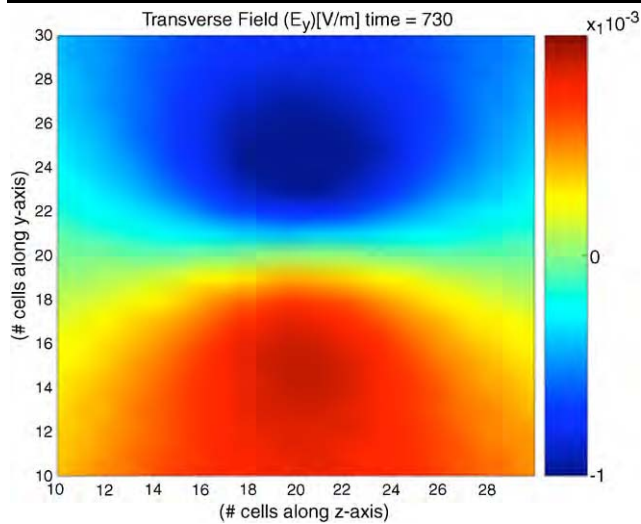


**Fig. 15** Snapshot of  $E_y$  taken 50 nm from the left contact, 1.25 fs after the peak of the injection pulse. The observed dipolar nature of the pulse is characteristic of the near-field region

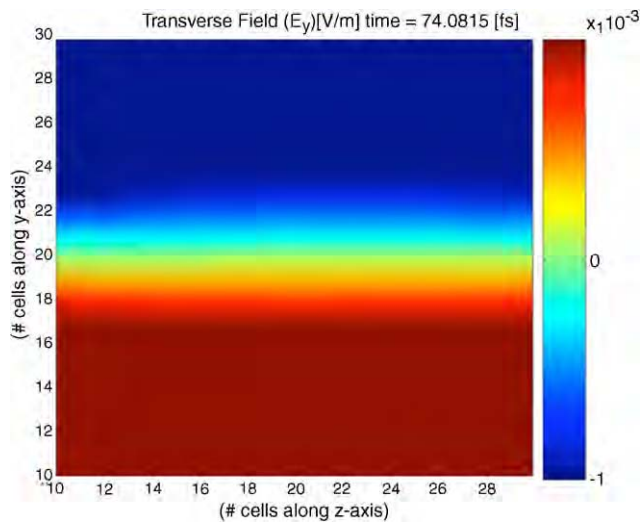


**Fig. 16** Snapshot taken 480 nm from left contact of transverse  $E_y$  component of the electric field 74 fs after the peak of the injection pulse. This wavefront resembles a plane wave (TEM wave) in the far field region

a constantly increasing dipole moment. This displacement of both electrons and holes versus simulation time is plotted in Fig. 17 and validates the notion of an oscillating dipole. When one moves into the far-field region (Fig. 16) the wavefront becomes TEM or plane wave-like in nature. The resulting drift velocities of both electrons and holes are shown in Fig. 18. Peak overshoot velocities of  $7.4 \times 10^7$  cm/s for electrons and  $-1.5 \times 10^7$  cm/s for holes were determined and are in good agreement with those reported in [88] using just the CMC/Poisson device simulator.

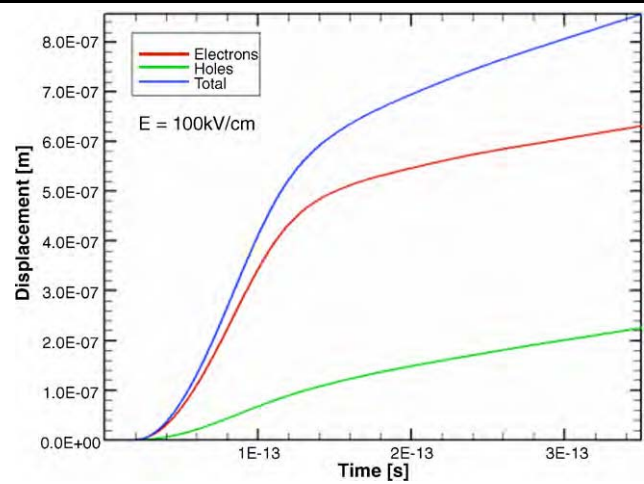


**Fig. 17** Displacement of electrons and holes in the device versus time for the simulation run at 100 kV/cm

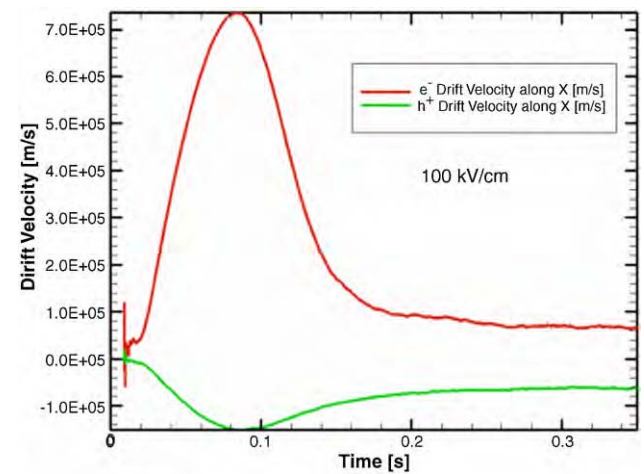


**Fig. 18** Drift velocities of electrons and holes versus time for the simulation run at 100 kV/cm

#### 4.2 Single 0.1 $\mu\text{m}$ gate GaAs MESFET

The coupled device simulator has also been applied to the simulation of a simple 3D MESFET. In [38], a 0.1  $\mu\text{m}$ , single-gate, 3D MESFET was modeled using a version of the coupled simulator which used a conventional 3D FDTD with split-field PML absorbing boundary conditions. Fourier decomposition was used to study the small signal response of this simple device structure. The basic layout of the device is similar to the generic layout illustrated in Fig. 13 but with a 0.1  $\mu\text{m}$  gate length. Specific device dimensions are given in Table 2. An  $80 \times 35 \times 25$  uniform mesh was used. The  $dc$  bias point chosen placed the active device well into the saturation region of transistor operation. A Gaussian pulse excitation with a 3 ps pulse width was applied over a 20 ps period to both gate and drain electrodes separately resulting in a frequency resolution of 50 GHz. The source-gate (input voltage) and source-drain (output voltage) were

**Table 2** Parameters used in device simulation

drain/source contacts	0.5 $\mu\text{m}$
source-gate separation	0.4 $\mu\text{m}$
drain-gate separation	0.4 $\mu\text{m}$
device length	2.0 $\mu\text{m}$
device width	125 $\mu\text{m}$
active layer thickness	0.1 $\mu\text{m}$
active layer doping	$2 \times 10^{-17} \text{ cm}^{-3}$
Schottky barrier height	0.8 V
<i>dc</i> gate-source voltage	-0.5 V
<i>dc</i> drain voltage	0.5 V
<i>ac</i> excitation source peak voltage	0.1 V

computed just forward of the source plane and at 125  $\mu\text{m}$  respectively, and stored at each time step. These voltages were computed by simply integrating the  $x$ -directed electric field component along a line between the source-gate and source-drain regions as follows:

$$V = - \int_a^b E_x \cdot dl, \quad (17)$$

where  $b - a$  represents the distance between source-gate and source-drain regions. The corresponding voltage gain versus frequency was computed by taking the ratio of the Fourier transforms of these input and output voltages as

$$\text{Voltage gain}(\omega) = 20 \log \left\{ \frac{V_{\text{out}}(\omega, z_i)}{V_{\text{in}}(\omega, z_o)} \right\}, \quad (18)$$

where  $z_i$  and  $z_o$  represent the distributed and characteristic impedances and  $V_{\text{in}}$  and  $V_{\text{out}}$  are the corresponding input and output voltages. The result of this calculation is given in Fig. 19.

In addition, the  $S$ -parameters were also computed over a range of frequencies by taking the ratio of the Fourier transforms of incident and reflected voltages on port 1 (source-gate) and port 2 (drain-source) in the front passive section just before the active device region. Using these parameters, the forward current gain,  $h_{21}$ , was computed via

$$h_{21} = \frac{-2S_{21}}{(1 - S_{11})(1 + S_{22}) + S_{12}S_{21}}. \quad (19)$$

The result of this calculation is plotted in Fig. 20. A cutoff frequency of approximately 170 GHz was estimated from the curve.

This work demonstrated that an EM wave solver could be directly coupled to a full-band particle-based simulator for the global modeling of a microwave transistor. The computed voltage gain was approximately 36% larger than that predicted by previous global modeling of a similar device

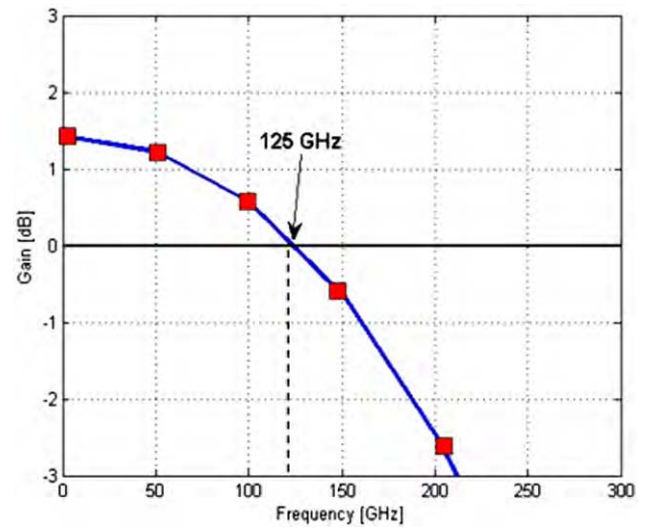


**Fig. 19** Computed voltage gain versus frequency for 0.1  $\mu\text{m}$  gate MESFET using a coupled CMC/conventional FDTD simulator. A maximum cutoff frequency of 125 GHz is determined for a device width of 125  $\mu\text{m}$

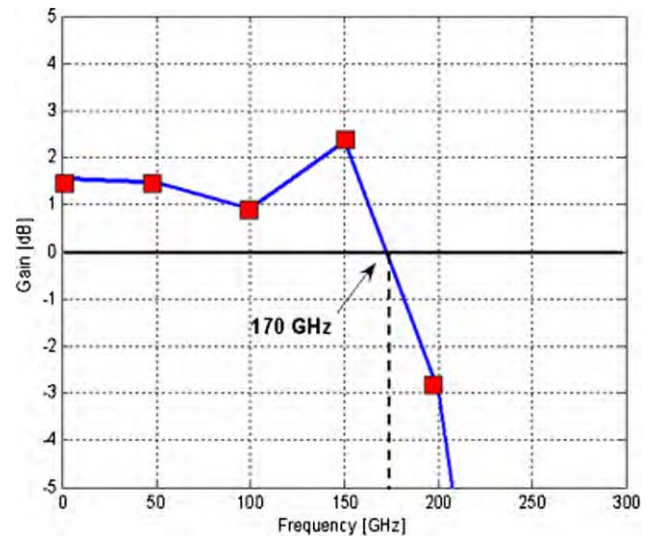


**Fig. 20** Computed current gain versus frequency for 0.1  $\mu\text{m}$  gate MESFET using a coupled CMC/conventional FDTD simulator. An estimate for the maximum cutoff frequency of 170 GHz is determined for a device width of 125  $\mu\text{m}$

using a hydrodynamic-based simulator coupled to a conventional FDTD [6, 89–92]. This difference is attributed in part to the statistical noise inherent to particle-based solvers and also to the specific manner in which the input and output ports of the simulated structure were defined. This latter issue will be discussed in more detail in the next section and addressed through the adoption and implementation of a typical ground-signal-ground (GSG) device layout.

The coupled simulator used in this case employed a conventional FDTD. It was, therefore, severely limited

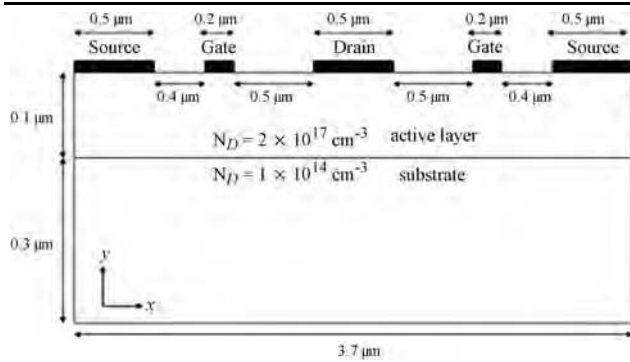


**Fig. 21** Cross-section of simulated 3D dual-gate MESFET device

by the Courant stability requirement. Although the initial *dc* bias point solution could be obtained using a coupled CMC/Poisson time step of 5 fs, the full-wave portion of the total simulation was limited to a maximum FDTD time step of 0.04 fs or about two orders of magnitude smaller than that necessary in the CMC solver. This added computational burden has been resolved with the implementation of the ADI-FDTD method, as described below.

#### 4.3 Dual-finger 0.2 μm gate GaAs MESFET

The 2D cross-section of the 3D dual-gate GaAs MESFET simulated using the CMC/ADI-FDTD coupled simulator is shown in Fig. 21. This structure is simply a combination of two single-gate MESFETs.

A  $141 \times 25$  uniform grid mesh was used along the *x*- and *y*-directions, respectively. The choice of a uniform grid was based upon the fact that both the CMC and FDTD solvers operate on the same grids during the simulation. Although the CMC grid is embedded within the total FDTD grid, its dimensions and cell spacings are matched to those used in the full-wave portion of the simulation. The use of a uniform grid mesh in the FDTD solver helps to minimize the numerical dispersion due to grid error. The standard ADI-FDTD algorithm suffers from the build up of both local and global error over time due to truncation errors made in the approximation of the derivative operator.

##### 4.3.1 Full-wave analysis of the passive structure

A full-wave simulation of the passive device structure was performed in order to generate a full set of *S*-parameters for comparison with those obtained during the coupled simulations discussed in the next section. In this simulation, the ADI-FDTD algorithm with CPML is used. The simulation was performed using a  $141 \times 60 \times 35$  uniform cubic mesh. These simulations were run using an FDTD time step of 5 fs. A differentiated Gaussian pulse with a halfwidth of 1.5 ps is used as the primary excitation source in the passive *ac* simulation. It is applied at 3 cells away from the CPML on either the gate or drain.

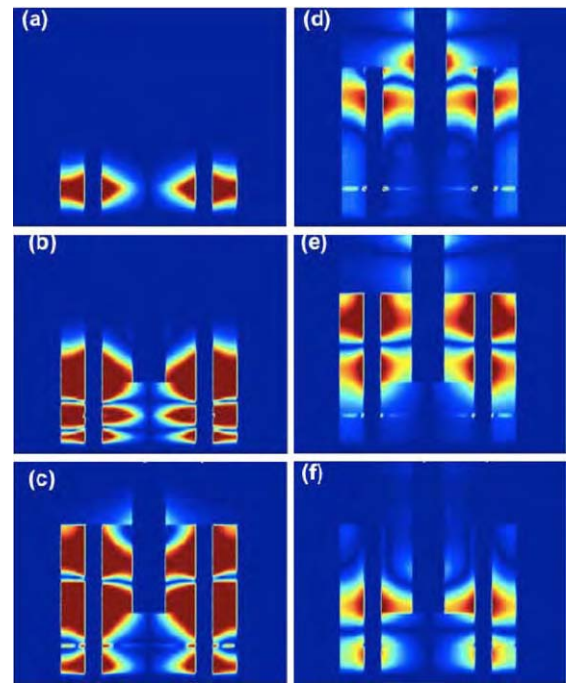


**Fig. 22** Snapshots at (a) 2.5 ps, (b) 5 ps, (c) 7.5 ps, (d) 10 ps, (e) 12.5 ps and (f) 15 ps of the magnitude of  $E_x$  for the excitation applied to the gate

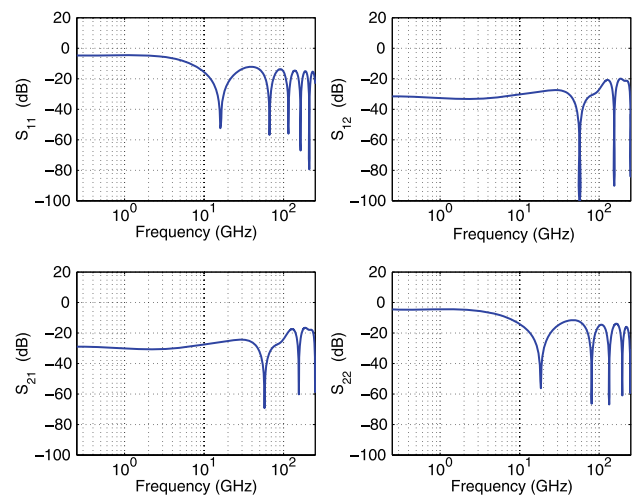


**Fig. 23** Set of calculated *S*-parameters for the passive structure

Snapshots of the wave propagation resulting from the excitation source being applied to the gate are given in Fig. 22. The calculated *S*-parameters are shown in Fig. 23.

##### 4.3.2 Full-band/full-wave analysis of the coupled device structure

A fully coupled 3D simulation of the structure shown in Fig. 21 was performed using the same parameters and excitation source as above. At the start of the full-wave simulation, the CMC device simulation is allowed to run coupled



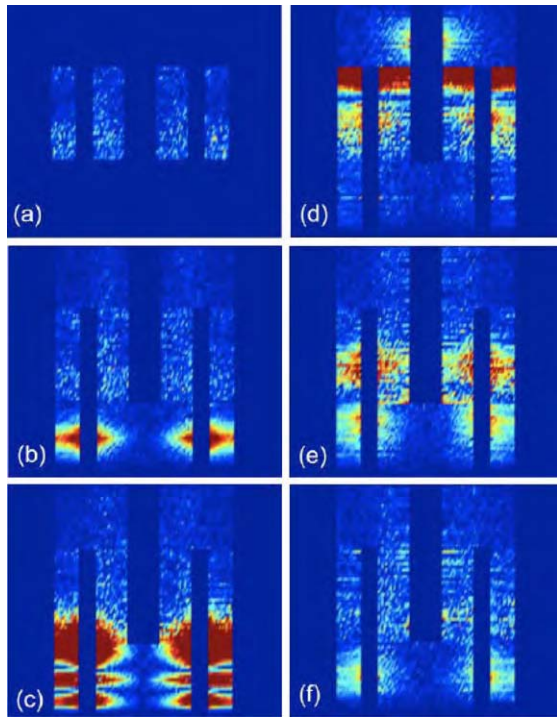


**Fig. 24** Snapshots at (a) 0.15 ps, (b) 7.35 ps, (c) 9.85 ps, (d) 15.85 ps, (e) 18.85 ps and (f) 21.85 ps, of the magnitude of  $E_x$  for the excitation applied to the gate

to the full-wave solver for 5 ps prior to the application of the excitation source pulse. This allows a finite amount of time for the resulting *ac* transients to propagate throughout the FDTD grid. These transients are due to the addition of the time-varying magnetic field into the calculation of the total Lorentz force in the CMC portion of the coupled simulator. This results in a new steady state (quasi-static *dc* condition).

Snapshots of the resulting wave propagation are shown in Fig. 24. At the beginning of the simulation, the electric field is localized within the active region of the domain as shown in the figures. The inclusion of the magnetic field results in a redistribution of the fields out into the passive regions of the structure. The carrier-wave interaction is also apparent in the localized or granular nature of the wavefront as it propagates through the active portion of the domain, and reflects off the open-ended terminations of both the gate and drain contacts.

The full set of calculated *S*-parameters are shown in Fig. 25. The corresponding current gain  $h_{21}$ , calculated according to (19), is plotted in Fig. 26. The unilateral power gain (UPG) was computed using the following expression

$$\text{UPG} = \frac{|S_{21}|^2}{|(1 - |S_{11}|^2)(1 - |S_{22}|^2)|^2} \quad (20)$$

and the resulting curve plotted in Fig. 27. The cutoff frequency (corresponding to unity current gain) and  $f_{\text{max}}$  (corresponding to unity UPG) are readily extracted from Figs. 26 and 27.

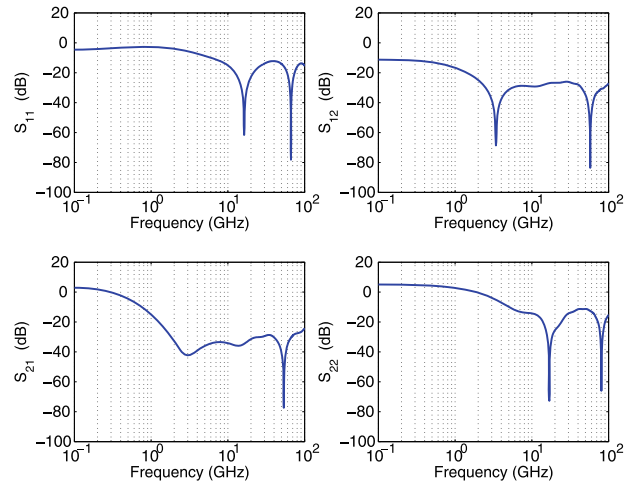


**Fig. 25** Set of calculated *S*-parameters for the active structure

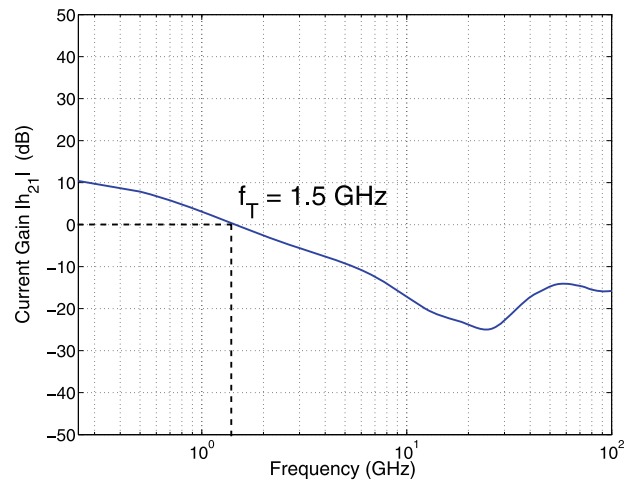


**Fig. 26** Current gain ( $h_{21}$ ) versus frequency

In these simulations, both the gate and drain contacts were assumed to be simply transmission lines with characteristic impedances matched to that of the source and load. The CPML used to truncate the domain was used as a substitute for the lumped circuit elements that would represent the source and load impedances. This is an over-simplification of the problem and does not fully account for the true impedances of the discontinuities present in actual fabricated devices.

## 5 Summary and outlook

We have reviewed recent advances in the global modeling of carrier-field interaction in semiconductor materials and devices using coupled EMC-FDTD simulation tools. Of special interest are applications at high-microwave and THz frequencies, as doped semiconductor plasma frequencies and characteristic carrier scattering rates fall into this



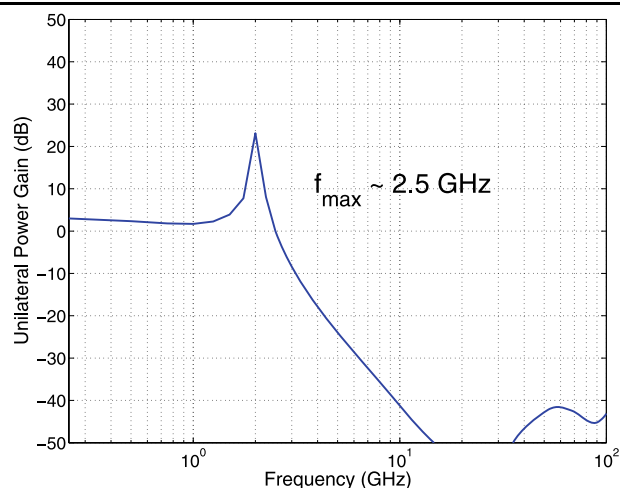


**Fig. 27** Unilateral power gain (UPG) versus frequency

range. Therefore, common simplifications used to allow independent consideration of the particle and the field dynamics are not justified; rather, efficient modeling tools that comprehensively couple carrier transport with full-wave electrodynamics are necessary to provide an accurate description of materials properties.

Coupled EMC-FDTD simulation tools combine two highly accurate and versatile techniques, and they present state-of-the-art in global modeling. The coupled simulation was illustrated on two types of THz-frequency excitation: electromagnetic irradiation (Sect. 3) and *ac* biasing (Sect. 4). We discussed the stability and accuracy requirements for both. In particular, we presented simulation data for the THz-regime conductivity of doped bulk silicon under irradiation, and showed a very good agreement of the calculated complex conductivity with experimental data (Sect. 3). In Sect. 4.1, ultrafast carrier dynamics and radiation patterns in thin intrinsic GaAs are faithfully captured via a CMC-FDTD simulation (CMC being an outgrowth of ensemble Monte Carlo), while the same technique offers a detailed numerical insight into the *ac* response of high-speed GaAs MESFETs (Sect. 4.2).

Efficiency of global modeling tools will continue to improve through algorithm development and parallelization. Further developments likely include analyses of heating in high-speed devices by adding thermal transport to the coupled carrier-field simulation. Also, growing interest in high-frequency behavior of quantum structures may stimulate coupling of quantum transport techniques (Wigner-function simulation or nonequilibrium Green's functions) with full wave electrodynamics.

**Acknowledgements** The authors thank Prof. John Booske (University of Wisconsin-Madison) and Prof. Stephen M. Goodnick (Arizona State University) for helpful discussions. This work has been supported by the AFOSR (grant FA9550-08-1-0052), the DOD Breast Cancer Research Program (grant W81XWH-07-1-0629), the Wisconsin Alumni

Research Foundation, and the DARPA SWIFT project through the Army Research Laboratory under cooperative agreement W911NF-06-2-0012.

## References

1. Tomizawa, K.: Numerical Simulation of Submicron Semiconductor Devices. Artech House, Norwood (1993)
2. Lundstrom, M.: Fundamentals of Carrier Transport, 2nd edn. Cambridge University Press, Cambridge (2000)
3. Jacoboni, C., Lugli, P.: The Monte Carlo Method for Semiconductor Device Simulation. Springer, New York (1989)
4. Hockney, R.W., Eastwood, J.W.: Computer Simulation Using Particles. Adam Hilger, Bristol (1988)
5. Taflov, A., Hagness, S.C.: Computational Electrodynamics: The Finite-Difference Time-Domain Method, 3rd edn. Artech House, Norwood (2005)
6. Alsunaidi, M.A., Imtiaz, S.M., El-Ghazaly, S.: IEEE Trans. Microw. Theory Tech. **44**, 799 (1996)
7. Grondin, R.O., El-Ghazaly, S., Goodnick, S.M.: IEEE Trans. Microw. Theory Tech. **47**, 817 (1999)
8. Langdon, A.B., Dawson, J.M.: Investigations of a sheet model for a bounded plasma with magnetic field and radiation. In: Symposium on Computer Simulation of Plasma and Many-Body Problems, College of William and Mary, Virginia, USA, April 19–21, 1967, p. 39. Scientific and Technical Information Division of the Office of Technology Utilization, NASA, Washington (1967)
9. Buneman, O.: Relativistic Plasmas. Coral Gables, Florida (1968)
10. Yee, K.S.: IEEE Trans. Antennas Propag. **AP-14**, 302 (1966)
11. Burn, R.D.: J. Plasma Phys. **12**, 331 (1970)
12. Sinz, K.H.: In: Fourth Conference on Numerical Simulation of Plasmas, Washington, D.C., 1970
13. Haber, I., Wagner, C.E., Boris, J.P., Dawson, J.M.: In: Fourth Conference on Numerical Simulation of Plasmas, Washington, D.C., 1970
14. Boris, J.P.: In: Fourth Conference on Numerical Simulation of Plasmas, Washington, D.C., 1970
15. Boris, J.P., Lee, R.: J. Comput. Phys. **12**, 131 (1973)
16. Godfrey, B.B.: J. Comput. Phys. **15**, 504 (1974)
17. Godfrey, B.B., Langdon, A.B.: J. Comput. Phys. **20**, 251 (1976)
18. Birdsall, C.K., Langdon, A.B.: Plasma Physics via Computer Simulation. Adam Hilger, Bristol (1991)
19. Langdon, A.B., Lasinski, B.F.: Meth. Comput. Phys. **16**, 327 (1976)
20. Dawson, J.M.: Rev. Mod. Phys. **55**, 403 (1983)
21. Morse, R.L., Nielson, C.W.: Phys. Fluids **14**, 830 (1971)
22. Langdon, A.B.: Phys. Fluids **15**, 1149 (1972)
23. Buneman, O., Barnes, C.W., Green, J.C., Nielsen, D.E.: J. Comput. Phys. **38**, 1 (1980)
24. Taflov, A.: Advances in Computational Electrodynamics: The Finite-Difference Time-Domain Method. Artech House, Norwood (1998)
25. Jacoboni, C., Reggiani, L.: Rev. Mod. Phys. **55**, 645 (1983)
26. Blotekjaer, K.: IEEE Trans. Electron Devices **17**, 38 (1970)
27. Shur, M.: Electron. Lett. **12**, 615 (1976)
28. Carne, B., Cappy, A., Kaszynski, A., Constant, E., Salmer, G.: J. Appl. Phys. **51**, 784 (1980)
29. Feng, Y.K., Hintz, A.: IEEE Trans. Electron Devices **35**, 1419 (1988)
30. Goasguen, S., Tomeh, M.M., El-Ghazaly, S.: IEEE Trans. Microw. Theory Tech. **49**, 2258 (2001)
31. Goasguen, S., El-Ghazaly, S.: IEEE Microw. Guided Wave Lett. **10**, 273 (2000)
32. Hussein, Y.A., El-Ghazaly, S.: IEEE Trans. Microw. Theory Tech. **51**, 1842 (2003)

33. Hussein, Y.A., El-Ghazaly, S., Goodnick, S.M.: IEEE Trans. Microw. Theory Tech. **51**, 2234 (2003)
34. Hussein, Y.A., El-Ghazaly, S.: IEEE Trans. Microw. Theory Tech. **52**, 329 (2004)
35. Movahhedi, M., Abdipour, A.: IEEE Trans. Microw. Theory Tech. **54**, 2636 (2006)
36. El-Ghazaly, S., Joshi, R.P., Grondin, R.O.: IEEE Trans. Microw. Theory Tech. **36**, 629 (1990)
37. Ayubi-Moak, J.S., Goodnick, S.M., Aboud, S.J., Saraniti, M., El-Ghazaly, S.: J. Comput. Electron. **2**, 183 (2003)
38. Ayubi-Moak, J.S., Goodnick, S.M., Saraniti, M.: J. Comput. Electron **5**, 415 (2006)
39. Ayubi-Moak, J.S., Ferry, D.K., Goodnick, S.M., Akis, R., Saraniti, M.: IEEE Trans. Electron Devices **54**, 2327 (2007)
40. Ayubi-Moak, J.S., Goodnick, S.M., Ferry, D.K., Akis, R., Saraniti, M., Faralli, N.: Physica Status Solidi (c) **5**, 135 (2008)
41. Ayubi-Moak, J.S., Goodnick, S.M., Ferry, D.K., Akis, R., Saraniti, M., Faralli, N.: J. Comput. Electron. **7**, 187 (2008)
42. Willis, K.J., Hagness, S.C., Knezevic, I.: In: 13th International Workshop on Computational Electronics (IWCE 2009), Beijing, 2009. <http://dx.doi.org/10.1109/IWCE.2009.5091080>
43. Willis, K.J., Hagness, S.C., Knezevic, I.: Appl. Phys. Lett. (2009, in preparation)
44. Hess, K.: Monte Carlo Device Simulation: Full Band and Beyond. Kluwer Academic Publishers, Dordrecht (1991)
45. Fischetti, M.V., Laux, S.: Phys. Rev. B **38**, 9721 (1988)
46. Langdon, A.B.: J. Comput. Phys. **6**, 247 (1970)
47. Shichijo, H., Hess, K.: Phys. Rev. B **23**, 4197 (1981)
48. Tang, J.Y., Hess, K.: J. Appl. Phys. **54**, 5139 (1983)
49. Fischetti, M.V., Dimaria, D.J., Brorson, S.D., Theis, T.N., Kirtley, J.: Phys. Rev. B **31**, 8124 (1985)
50. Kometer, K., Zandler, G., Vogl, P.: Phys. Rev. B **46**, 1382 (1992)
51. Saraniti, M., Goodnick, S.M.: IEEE Trans. Electron Devices **47**, 1909 (2000)
52. Balanis, C.A.: Advances Engineering Electromagnetics, Chap. 7.8, pp. 329–332. Wiley, New York (1989)
53. Schneider, J.B.: IEEE Trans. Antennas Propag. **52**, 3280 (2004)
54. Schneider, J.B., Abdijalilov, K.: IEEE Trans. Antennas Propag. **54**, 2531 (2006)
55. Abdijalilov, K., Schneider, J.B.: IEEE Antennas Wirel. Propag. Lett. **5**, 454 (2006)
56. Berenger, J.P.: IEEE Trans. Antennas Propag. **44**, 110 (1996)
57. Berenger, J.P.: J. Comput. Phys. **127**, 363 (1996)
58. Roden, J.A., Gedney, S.D.: Microw. Opt. Technol. Lett. **27**, 334 (2000)
59. Courant, R., Friedrichs, K., Levy, H.: IBM J. Res. Dev. (1967)
60. Namiki, T.: IEEE Trans. Microw. Theory Tech. **47**, 2003 (1999)
61. Namiki, T.: IEEE Trans. Microw. Theory Tech. **48**, 1950 (2000)
62. Zhen, F., Chen, Z., Zhang, J.: IEEE Trans. Antennas Propag. **48**, 1550 (2000)
63. Zheng, F., Chen, Z.: IEEE Trans. Antennas Propag. **49**, 1006 (2001)
64. Laux, S.E.: IEEE Trans. Comput-Aided Des. Integr. Circuits Syst. **15**, 1266 (1996)
65. Birdsall, C.K., Fuss, D.: J. Comput. Phys. **3**, 494 (1969)
66. Eastwood, J.W.: J. Comput. Phys. **18**, 1 (1975)
67. Marder, B.: J. Comput. Phys. **68**, 48 (1987)
68. Villasenor, J., Buneman, O.: Comput. Phys. Commun. **69**, 306 (1992)
69. Esirkepov, T.Z.: Comput. Phys. Commun. **135**, 144 (2001)
70. Barthelmé, R., Parzani, C.: Numerical Methods for Hyperbolic and Kinetic Problems, pp. 7–28. European Mathematical Society, Marseille (2005)
71. Hockney, R.W.: Phys. Fluids **9**, 1826 (1966)
72. van Exter, M., Grischkowsky, D.: Phys. Rev. B **41**, 12140 (1990)
73. Grischkowsky, D., Keiding, S., van Exter, M., Fattinger, C.: J. Opt. Soc. Am. B-Opt. Phys. **7**, 2006 (1990)
74. Nashima, S., Morikawa, O., Takata, K., Hangyo, M.: J. Appl. Phys. **90**, 837 (2001)
75. Hangyo, M., Tani, M., Nagashima, T.: Int. J. Infrared Millim. Waves F **26**, 1661 (2005)
76. Herrmann, M., Tani, M., Sakai, K., Fukasawa, R.: J. Appl. Phys. **91**, 1247 (2002)
77. van Exter, M., Grischkowsky, D.: Appl. Phys. Lett. **56**, 1694 (1990)
78. Jeon, T.I., Grischkowsky, D.: Phys. Rev. Lett. **78**, 1106 (1997)
79. Jeon, T.I., Grischkowsky, D.: Appl. Phys. Lett. **72**, 3032 (1998)
80. Nashima, S., Morikawa, O., Takata, K., Hangyo, M.: Appl. Phys. Lett. **79**, 3923 (2001)
81. Morikawa, O., Tonouchi, M., Hangyo, M.: Appl. Phys. Lett. **76**, 1519 (2000)
82. Morikawa, O., Tonouchi, M., Hangyo, M.: Appl. Phys. Lett. **75**, 3772 (1999)
83. Mendis, R.: Electron. Lett. **42**, 19 (2006)
84. Nagashima, T., Hangyo, M.: Appl. Phys. Lett. **79**, 3917 (2001)
85. Howells, S.C., Schlie, L.A.: Appl. Phys. Lett. **69**, 550 (1996)
86. Hull, R.: Properties of Crystalline Silicon. IET, Stevenage (1999)
87. Leitenstorfer, A., Hunsche, S., Shah, J., Nuss, M.C., Knox, W.H.: Phys. Rev. B **61**, 16642 (2000)
88. Wigger, S., Saraniti, M., Goodnick, S.M., Leitenstorfer, A.: J. Comput. Electron. **1**, 475 (2002)
89. Imtiaz, S.M., El-Ghazaly, S.: IEEE Trans. Microw. Theory Tech. **46**, 923 (1998)
90. Imtiaz, S.M., El-Ghazaly, S.: IEEE Trans. Microw. Theory Tech. **45**, 2208 (1997)
91. Imtiaz, S.M.S.: Ph.D. thesis, Arizona State University (1999)
92. Hammadi, S.M., El-Ghazaly, S.: IEEE Trans. Microw. Theory Tech. **47**, 890 (1999)

# Toward Carbon-Nanotube-Based Theranostic Agents for Microwave Detection and Treatment of Breast Cancer: Enhanced Dielectric and Heating Response of Tissue-Mimicking Materials

Alireza Mashal\*, *Student Member, IEEE*, Balaji Sitharaman, Xu Li, *Member, IEEE*, Pramod K. Avti, Alan V. Sahakian, *Fellow, IEEE*, John H. Booske, *Fellow, IEEE*, and Susan C. Hagness, *Fellow, IEEE*

**Abstract**—The experimental results reported in this paper suggest that single-walled carbon nanotubes (SWCNTs) have the potential to enhance dielectric contrast between malignant and normal tissue for microwave detection of breast cancer and facilitate selective heating of malignant tissue for microwave hyperthermia treatment of breast cancer. In this study, we constructed tissue-mimicking materials with varying concentrations of SWCNTs and characterized their dielectric properties and heating response. At SWCNT concentrations of less than 0.5% by weight, we observed significant increases in the relative permittivity and effective conductivity. In microwave heating experiments, we observed significantly greater temperature increases in mixtures containing SWCNTs. These temperature increases scaled linearly with the effective conductivity of the mixtures. This work is a first step towards the development of functionalized, tumor-targeting SWCNTs as theranostic (integrated therapeutic and diagnostic) agents for microwave breast cancer detection and treatment.

**Index Terms**—Breast cancer, carbon nanotubes, contrast agent, dielectric spectroscopy, microwave hyperthermia, microwave imaging, phantoms.

## I. INTRODUCTION

MICROWAVE-FREQUENCY dielectric contrast between malignant and normal tissue in the breast serves as the physical basis for emerging microwave methods of detecting and treating breast cancer. Dielectric contrast leads to scatter-

ing of an illuminating microwave signal, which is exploited for breast cancer detection, and selective absorption of incident microwave power, which is exploited for localized hyperthermia treatment. The effective dielectric properties of breast tissue are influenced at microwave frequencies by endogenous polar molecules, such as free and bound water, peptides, and proteins. Consequently, the dielectric properties depend on the type and physiological state of the tissue. A recent study conducted by the University of Wisconsin-Madison and the University of Calgary showed that the endogenous dielectric contrast between malignant and normal adipose-dominated tissues in the breast is as large as 10:1, while the contrast between malignant and normal glandular/fibroconnective tissues is no more than about 10% [1].

The effective dielectric properties—both the dielectric constant and effective conductivity—can also be influenced by exogenous molecules introduced as contrast agents. For example, another recent study found that tissue-mimicking (TM) mixtures containing encapsulated microbubbles at clinically relevant concentrations, similar to those used in ultrasound imaging, exhibit significantly lower dielectric properties than pure TM materials [2]. Here, we propose the use of single-walled carbon nanotubes (SWCNTs) as a diagnostic and therapeutic agent—an integrated “theranostic” nanoplatform [3]—for both microwave detection and treatment of breast cancer. The size and unique physiochemical properties of SWCNTs make them ideal candidates for tumor-targeting applications [4]. SWCNT-based contrast agents have already shown promise for molecular imaging by magnetic resonance, positron emission tomography, nuclear, and photoacoustic imaging modalities [5]–[7].

Our present investigation is motivated by the hypothesis that the accumulation of biocompatible carbon nanotubes in tumors will significantly increase the microwave-frequency dielectric properties of the tumor. Exogenous particles passively accumulate via an enhanced permeability and retention effect in tumor vasculature [8]. Functionalization of these particles with tumor-targeting biomarkers may amplify their accumulation properties in tumors [9]. The presence of carbon nanotubes in or near a malignant lesion will result in changes to the dielectric properties of malignant tissue. If these changes are significant, they can be used to enhance the sensitivity of low-power microwave imaging of breast cancer via differential imaging [10], [11] and to enhance the selectivity of higher power microwave thermal therapy.

Manuscript received December 22, 2009; revised January 24, 2010; accepted January 31, 2010. Date of publication February 18, 2010; date of current version July 14, 2010. This work was supported by the Department of Defense Breast Cancer Research Program under Grant W81XWH-07-1-0629, by the National Institutes of Health under Grant R01CA112398 awarded by the National Cancer Institute, and by the Carol M. Baldwin Breast Cancer Research Fund. *Asterisk indicates corresponding author.*

\*A. Mashal is with the Department of Electrical and Computer Engineering, University of Wisconsin, Madison, WI 53706 USA (e-mail: amashal@wisc.edu).

B. Sitharaman and P. K. Avti are with the Department of Biomedical Engineering, Stony Brook University, Stony Brook, NY 11794 USA (e-mail: bsitharaman@notes.cc.sunysb.edu; pavti@notes.cc.sunysb.edu).

X. Li and A. V. Sahakian are with the Department of Biomedical Engineering, Northwestern University, Evanston, IL 60208 USA (e-mail: xuli@northwestern.edu; sahakian@ece.northwestern.edu).

J. H. Booske and S. C. Hagness are with the Department of Electrical and Computer Engineering, University of Wisconsin, Madison, WI 53706 USA (e-mail: booske@engr.wisc.edu; hagness@engr.wisc.edu).

Color versions of one or more of the figures in this paper are available online at <http://ieeexplore.ieee.org>.

Digital Object Identifier 10.1109/TBME.2010.2042597



In this paper, we report the results of wideband (0.6–20 GHz) dielectric spectroscopy measurements and heating efficiency experiments (at 3 GHz) using TM materials mixed with various concentrations of SWCNTs that have been identified to be non-toxic in mice [12]. Our study addresses the dielectric and thermal effect of SWCNTs over the frequency range that is of interest for microwave imaging and hyperthermia treatment of breast cancer. Frequencies between 0.5 and 3 GHz are commonly employed in microwave imaging via inverse scattering [13] while the ultra-wideband range of 3.1–10.6 GHz is of interest in tissue-penetrating radar imaging [14]. Microwave-induced thermoacoustic imaging has been explored using 434 MHz [15] and 3 GHz [16]. Microwave hyperthermia treatment of breast cancer has been conducted at 915 MHz [17], although slightly higher frequencies (1.5–4.0 GHz) have been shown recently to be optimal for tightly focusing microwave energy in the breast [18]. We choose 3 GHz for our heating experiments because of its relevance to both microwave-induced thermoacoustic imaging and hyperthermia treatment. Our work complements previous radiofrequency heating studies [19] as well as previous microwave-frequency characterizations of the dielectric properties of mixtures of SWCNTs or multiwalled carbon nanotubes in various host media of interest for electromagnetic shielding and radar absorption [20]–[26].

## II. MATERIALS AND METHODS

### A. Construction of Samples

The TM materials were constructed from oil-in-gelatin dispersions following the procedure outlined in [27]. The dielectric properties of these materials can be customized to mimic the properties of a variety of human soft tissues by controlling the concentrations of gelatin, safflower oil, kerosene, and preservatives. The results reported in [1] show that a 10%-oil mixture adequately replicates the microwave properties of malignant breast tissue over our frequency range of interest (0.6 GHz to 20 GHz). Furthermore, these materials are relatively inexpensive to fabricate and possess long term stability.

For this study we constructed 10%-oil TM materials with various concentrations of SWCNTs. The SWCNTs were synthesized by a commercial vendor (Cheap Tubes Inc., Brattleboro, VT) using a chemical vapor deposition technique and acid treated for purification. According to the manufacturer's specifications, the nanotubes were 1–2 nm in diameter and 5–30  $\mu\text{m}$  in length, and were composed of mainly SWCNTs (>90% by weight) with trace amounts of multiwalled carbon nanotubes and metal catalyst (e.g., cobalt, 1% by weight). We mixed various concentrations (1, 2, and 3 mg/mL) of SWCNTs into a 1% by weight mixture of Pluronic (F127) and deionized water using a probe sonicator for 25 min at a 120 W power level. Then, we substituted these mixtures for the pure deionized water in the TM recipe described in [27]. The resulting percent-by-weight concentrations of SWCNTs in the samples were 0.07%, 0.15%, and 0.22%, respectively. For reference, we also constructed a pure TM mixture with the same amount of Pluronic as the other samples, but with no SWCNTs.

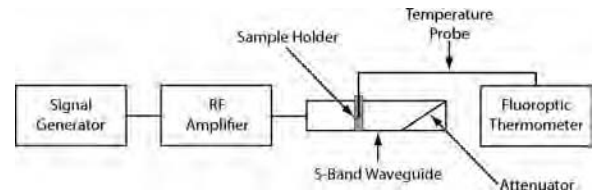


Fig. 1. Experimental setup for characterizing the heating response of a TM sample.

### B. Characterization of Dielectric Properties

The dielectric properties of the TM samples were characterized using a well established open-ended coaxial probe technique described in [28]. The measurement uncertainty of this technique is no more than approximately 10% [28]. We poured the liquid oil–gelatin mixtures, described in Section II-A, into small covered glass jars and allowed the mixture to gel unperturbed. We positioned the tip of the precision coaxial probe against the surface of the sample [27]. We conducted these measurements at room temperature (approximately 22 °C) on three TM samples of each SWCNT concentration.

### C. Characterization of Heating Response

The configuration for the heating experiment is shown in Fig. 1. We prepared the samples for the heating experiments by pouring the liquid TM mixture, as described in Section II-A, into a 1.1-mm-inner-diameter glass capillary tube. The mixture was allowed to gel around a fiber-optic temperature probe connected to a calibrated fluoroptic thermometer (Luxtron, 3100). The capillary tube was inserted through a small hole drilled into the center of the broad wall of an S-band (WR-284) rectangular waveguide with cross-sectional dimensions of 72 mm  $\times$  34 mm. The vertical extent of the sample in capillary tube spanned the entire height of the waveguide. A microwave synthesizer (Agilent, 83623B) and amplifier (Mini-Circuits, ZHL-42W) generated 1 W of continuous microwave power at 3 GHz that was delivered to the sample via the waveguide. The waveguide was terminated with a matched load to suppress standing waves and ensure single-pass electromagnetic wave illumination. Network analyzer measurements verified that the small hole drilled in the waveguide and the presence of the sample did not significantly perturb the fields inside the waveguide; namely, these waveguide alterations increased  $|S_{11}|$  by approximately 0.6 dB. The fluoroptic thermometer recorded the time-varying temperature of each sample as it was heated. We heated each sample for 3 min, then turned off the microwave source and allowed it to cool for 5 min.

## III. RESULTS AND DISCUSSION

### A. Dielectric Properties

Fig. 2(a) and (b) shows the relative permittivity and effective conductivity of the TM materials with various concentrations of SWCNTs over a frequency range of 0.6–20 GHz. Each wide-band curve represents the average properties (relative permittivity or effective conductivity) of the three samples with the same

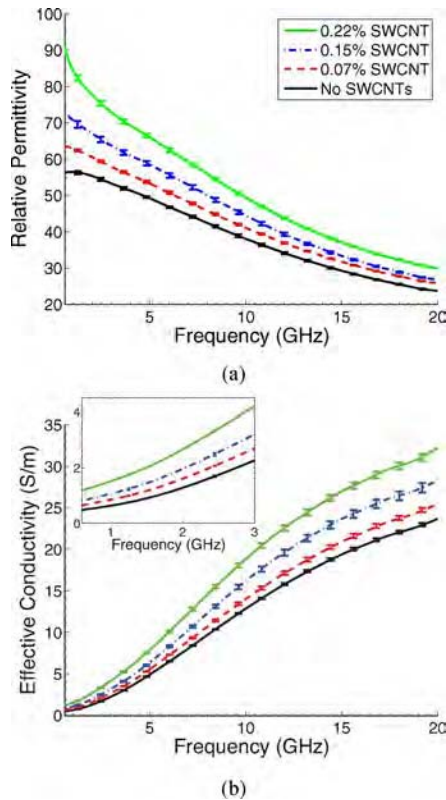


Fig. 2. (a) Relative permittivity and (b) effective conductivity of TM materials with varying concentrations of SWCNTs, measured from 0.6 to 20 GHz. Each curve represents the average properties of three different samples of the same concentration. The bars span the maximum and minimum values at specific frequencies. Both the permittivity and effective conductivity of the TM materials increase with increasing concentration of SWCNTs.

TABLE I  
SUMMARY OF DATA PRESENTED IN FIG. 2 AT 3 GHz

Percent by weight concentration of SWCNTs	Average $\epsilon_r$ (3 GHz)	Average $\sigma$ (3 GHz)	Average percent change $\epsilon_r$ (3 GHz)	Average percent change $\sigma$ (3 GHz)
None	53.3	2.3 S/m	-	-
0.07 %	57.9	2.7 S/m	9 %	16 %
0.15 %	63.7	3.2 S/m	19 %	38 %
0.22 %	73.0	4.2 S/m	37 %	81 %

SWCNT concentration. The vertical bars span the maximum and minimum values at specific frequencies. Table I summarizes the dielectric properties of the different TM mixtures at 3 GHz. This particular frequency is of interest for microwave inverse scattering [10], [11], microwave-induced thermoacoustic imaging [16], and microwave hyperthermia [18]. Both Fig. 2 and Table I show that the permittivity and conductivity increase with small increases in the concentration of SWCNTs.

These substantial changes in the dielectric properties caused by the carbon nanotubes will have a significant impact on microwave scattering and absorption. The results reported here were used in a microwave imaging computational test bed in order to determine the impact of these changes in microwave breast cancer detection [10], [11]. Briefly, microwave inverse scattering techniques were used to reconstruct images of anatomically realistic numerical breast phantoms with a compact malignant

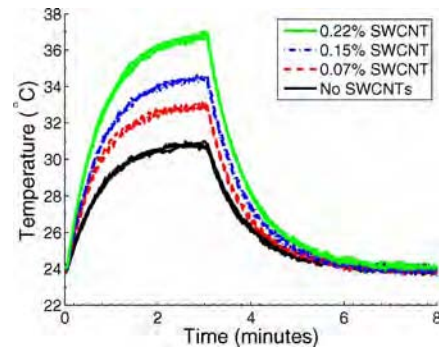


Fig. 3. Microwave heating response of TM materials with various concentrations of SWCNTs. Each curve shows the temperature profile of a sample that was heated via 3-GHz microwave illumination for 3 min and allowed to cool for 5 min. The maximum temperature of the TM mixtures increases with increasing concentration of SWCNTs.

TABLE II  
SUMMARY OF DATA PRESENTED IN FIG. 3

Percent by weight concentration of SWCNTs	Average steady-state temperature	Average temperature rise	$\Delta T$ increase compared to SWCNT-free sample
None	30.9°C	6.9°C	-
0.07 %	33.0°C	9.0°C	2.1°C
0.15 %	34.5°C	10.5°C	3.6°C
0.22 %	36.9°C	12.9°C	6.0°C

lesion. Two images were reconstructed: an image of a phantom with the endogenous dielectric properties of the tumor and another with elevated dielectric properties values due to the carbon nanotubes. A differential image was formed by subtracting the two images obtained from pre- and postcontrast measurements. Using this differential imaging technique, Shea *et al.* [10], [11] reported detection of previously undetectable tumors in four different classes of numerical phantoms that ranged from “mostly fatty” to “extremely dense” in radiographic density. These results suggest that the changes in dielectric properties shown in Fig. 2 are significant enough to dramatically improve the sensitivity of microwave imaging.

### B. Heating Response

Fig. 3 shows the time-dependent temperature rise of the various TM mixtures under continuous microwave illumination. The individual temperature value on each curve was a rolling average of five different temperature measurements of a single sample that was recorded every 0.25 s. For each TM mixture concentration, measurements were performed on three different samples of each TM mixture. Fig. 3 demonstrates the measurement repeatability for each concentration, as well as the statistical significance of the differences observed across concentrations. Table II summarizes the principal characteristics of the results shown in Fig. 3. These data show that as the concentration of SWCNTs in the TM material increases, the maximum temperature of that sample also increases. This increase in temperature for each TM mixture scales roughly linearly with the increase in conductivity reported in Table I, as expected for a configuration in which various samples are exposed to approximately the same electric field intensity. In other experiments, we

have observed that microwave-heated capillary tubes of liquids and SWCNT-containing liquids similarly exhibit a temperature rise proportional to their effective conductivity. Therefore, this heating response scaling appears to be a general trend, not restricted to just TM material mixtures.

The enhanced heating shown in Fig. 3 due to the carbon nanotubes is of interest to microwave-induced thermoacoustic imaging and microwave hyperthermia of breast cancer. Our results suggest that the increase in heating response will lead to a larger thermoacoustic response for a malignant tumor that is infused with carbon nanotubes in comparison to a tumor in a precontrast stage. In addition, the results of Fig. 3 suggest that malignant tissue that has preferentially accumulated carbon nanotubes will heat more efficiently; this selective heating is a desired property for microwave hyperthermia of breast cancer. As seen in Fig. 2(b), various samples exhibit a large spread in effective conductivity over the range of 0.6–20 GHz. Therefore, we expect a similar heating response to those seen in Fig. 3 for these samples over the 0.6–20 GHz frequency range.

#### IV. CONCLUSION

We characterized the dielectric properties of TM materials with several different concentrations of SWCNTs. Our results indicate that low concentrations of SWCNTs significantly impact the dielectric properties and heating response of the TM materials. For example, at 3 GHz, SWCNTs concentrations as small as 0.22% by weight increased the relative permittivity of the TM material by 37% and the effective conductivity by 81%. In our heating experiments, this concentration of SWCNTs led to an average steady-state temperature rise that was 6 °C higher than the rise observed in the TM material without SWCNTs. These results suggest that SWCNTs may enhance contrast for microwave imaging and facilitate selective microwave heating for treatment of breast cancer.

#### REFERENCES

- [1] M. Lazebnik, D. Popovic, L. McCartney, C. B. Watkins, M. J. Lindstrom, J. Harter, S. Sewall, T. Ogilvie, A. Magliocco, T. M. Breslin, W. Temple, D. Mew, J. H. Booske, M. Okoniewski, and S. C. Hagness, "A large-scale study of the ultrawideband microwave dielectric properties of normal, benign and malignant breast tissues obtained from cancer surgeries," *Phys. Med. Biol.*, vol. 52, pp. 6093–6115, 2007.
- [2] A. Mashal, J. H. Booske, and S. C. Hagness, "Toward contrast-enhanced microwave-induced thermoacoustic imaging of breast cancer: An experimental study of the effects of microbubbles on simple thermoacoustic targets," *Phys. Med. Biol.*, vol. 54, pp. 641–650, 2009.
- [3] B. Sumer and J. Gao, "Theranostic nanomedicine for cancer," *Nanomedicine*, vol. 3, no. 2, pp. 137–140, 2008.
- [4] M. McDevitt, D. Chattopadhyay, B. Kappel, J. Jaggi, S. Schiffman, C. Antczak, J. Njardarson, R. Brentjens, and D. Scheinberg, "Tumor targeting with antibody-functionalized, radiolabeled carbon nanotubes," *J. Nucl. Med.*, vol. 48, no. 7, pp. 1180–1189, 2007.
- [5] B. Sitharaman and L. Wilson, "Gadofullerenes and gadonanotubes: A new paradigm for high-performance magnetic resonance imaging contrast agent probes," *J. Biomed. Nanotechnol.*, vol. 3, no. 4, pp. 342–352, 2007.
- [6] Z. Liu, W. Cai, L. He, N. Nakayama, K. Chen, X. Sun, X. Chen, and H. Dai, "In vivo biodistribution and highly efficient tumour targeting of carbon nanotubes in mice," *Nat. Nanotechnol.*, vol. 2, no. 1, pp. 47–52, 2007.
- [7] A. De La Zerd, C. Zavaleta, S. Keren, S. Vaithilingam, S. Bodapati, Z. Liu, J. Levi, B. R. Smith, T.-J. Ma, O. Oralkan, Z. Cheng, X. Chen, H. Dai, B. T. Khuri Yakub, and S. S. Gambhir, "Carbon nanotubes as photoacoustic molecular imaging agents in living mice," *Nat. Nanotechnol.*, vol. 3, pp. 557–562, 2008.
- [8] H. Maeda, J. Wua, T. Sawaa, Y. Matsumurab, and K. Horic, "Tumor vascular permeability and the EPR effect in macromolecular therapeutics: A review," *J. Controlled Release*, vol. 65, pp. 271–284, 2000.
- [9] I. Brigger, C. Dubernet, and P. Couvreur, "Nanoparticles in cancer therapy and diagnosis," *Adv. Drug Del. Rev.*, vol. 54, pp. 631–651, 2002.
- [10] J. D. Shea, P. Kosmas, S. C. Hagness, and B. D. Van Veen, "Contrast-enhanced microwave breast imaging," presented at the 13th Int. Symp. Antenna Technol. Appl. Electromagn. (ANTEM) Can. Radio Sci. Meeting (URSI/CNC), Banff, AB, Canada, 2009.
- [11] J. D. Shea, P. Kosmas, S. C. Hagness, and B. D. Van Veen, "Contrast enhanced microwave imaging of breast tumors," *Inverse Prob.*, to be published.
- [12] Z. Liu, C. Davis, W. Cai, L. He, X. Chen, and H. Dai, "Circulation and long-term fate of functionalized, biocompatible single-walled carbon nanotubes in mice probed by raman spectroscopy," *Proc. Nat. Acad. Sci. USA*, vol. 105, no. 5, pp. 1410–1415, 2008.
- [13] T. Rubæk, P. M. Meaney, P. Meincke, and K. D. Paulsen, "Nonlinear microwave imaging for breast-cancer screening using Gauss-Newton's Method and the CGLS inversion algorithm," *IEEE Trans. Antennas Propag.*, vol. 55, no. 8, pp. 2320–2331, Aug. 2007.
- [14] X. Li, E. J. Bond, B. D. V. Veen, and S. C. Hagness, "An overview of ultrawideband microwave imaging via space-time beamforming for early-stage breast cancer detection," *IEEE Antennas Propag. Mag.*, vol. 47, no. 1, pp. 19–34, Feb. 2005.
- [15] R. Kruger, K. Miller, H. Reynolds, W. Kiser, D. Reinecke, and G. Kruger, "Breast cancer in vivo: Contrast enhancement with thermoacoustic CT at 434 MHz-feasibility study," *Radiology*, vol. 216, no. 1, pp. 279–283, 2000.
- [16] M. Xu, G. Ku, X. Jin, L. V. Wang, B. D. Fornage, and K. K. Hunt, "Breast cancer imaging by microwave-induced thermoacoustic tomography," *Proc. SPIE*, vol. 5697, pp. 45–48, 2005.
- [17] H. I. Vargas, W. C. Dooley, R. A. Gardner, K. D. Gonzalez, R. Venegas, S. H. Heywang-Kobrunner, and A. J. Fenn, "Focused microwave phased array thermotherapy for ablation of early-stage breast cancer: Results of thermal dose escalation," *Ann. Surg. Oncol.*, vol. 11, no. 2, pp. 139–146, 2004.
- [18] E. Zastrow, S. C. Hagness, and B. D. Van Veen, "3D computational feasibility study of non-invasive patient-specific microwave hyperthermia treatment of breast cancer," *Phys. Med. Biol.*, to be published.
- [19] C. Gannon, P. Cherukuri, B. Yakobson, L. Cognet, J. Kanzius, C. Kittrell, R. Weisman, M. Pasquali, H. Schmidt, R. Smalley, and S. Curley, "Carbon nanotube-enhanced thermal destruction of cancer cells in a noninvasive radiofrequency field," *Cancer*, vol. 110, no. 12, pp. 2654–2665, 2007.
- [20] J. Roberts, T. Imholt, Z. Ye, C. Dyke, D. Price Jr., and J. Tour, "Electromagnetic wave properties of polymer blends of single wall carbon nanotubes using a resonant microwave cavity as a probe," *J. Appl. Phys.*, vol. 95, pp. 4352–4356, 2004.
- [21] C. Xiang, Y. Pan, X. Liu, X. Sun, X. Shi, and J. Guo, "Microwave attenuation of multiwalled carbon nanotube-fused silica composites," *Appl. Phys. Lett.*, vol. 87, pp. 123103–1–123103-3, 2005.
- [22] Z. Fan, G. Luo, Z. Zhang, L. Zhou, and F. Wei, "Electromagnetic and microwave absorbing properties of multi-walled carbon nanotubes/polymer composites," *Mater. Sci. Eng., B*, vol. 132, pp. 85–89, 2006.
- [23] Y.-H. Li and J.-T. Lue, "Dielectric constants of single-wall carbon nanotubes at various frequencies," *J. Nanosci. Nanotechnol.*, vol. 7, pp. 3185–3188, 2007.
- [24] N. N. A. Moayed, U. Khan, M. Oboll, S. Gupta, and M. N. Afsar, "Characterization of single- and multi-walled carbon nanotubes at microwave frequencies," in *Proc. IEEE Instrum. Meas. Tech. Conf.*, 2007, pp. 1–4.
- [25] L. Wang, R. Zhou, and H. Xin, "Microwave (8–50 GHz) characterization of multiwalled carbon nanotube papers using rectangular waveguides," *IEEE Trans. Microw. Theory Tech.*, vol. 56, no. 2, pp. 499–506, Feb. 2008.
- [26] R. K. Challa, D. Kajfez, V. Demir, J. R. Gladden, and A. Z. Elsherbeni, "Characterization of multiwalled carbon nanotube (MWCNT) composites in a waveguide of square cross section," *IEEE Microw. Wireless Compon. Lett.*, vol. 18, no. 3, pp. 161–163, Mar. 2008.
- [27] M. Lazebnik, E. L. Madsen, G. R. Frank, and S. C. Hagness, "Tissue-mimicking phantom materials for narrowband and ultrawideband microwave applications," *Phys. Med. Biol.*, vol. 50, pp. 4245–4258, 2005.
- [28] D. Popovic, L. McCartney, C. Beasley, M. Lazebnik, M. Okoniewski, S. C. Hagness, and J. H. Booske, "Precision open-ended coaxial probes for in vivo and ex vivo dielectric spectroscopy of biological tissues at microwave frequencies," *IEEE Trans. Microw. Theory Tech.*, vol. 53, no. 5, pp. 1713–1722, Sep. 2005.

## Dielectric-Properties Contrast Enhancement for Microwave Breast Cancer Detection: Numerical Investigations of Microbubble Contrast Agents

*Mariya Lazebnik<sup>1</sup>, Susan C. Hagness<sup>1</sup>, John H. Booske<sup>1</sup>*

<sup>1</sup>Department of Electrical and Computer Engineering, University of Wisconsin – Madison, 1415 Engineering Drive, Madison, WI 53706, USA, lazebnik@cae.wisc.edu, hagness@engr.wisc.edu

### Abstract

The physical basis for microwave breast cancer detection is the dielectric-properties contrast between malignant and normal breast tissue. The Wisconsin-Calgary study showed that this contrast is as high as 10:1 in fatty breast tissue but no more than 10% in fibroglandular tissue. We are investigating the feasibility of air-filled microbubbles as contrast agents for enhancing the malignant-to-normal dielectric contrast. Our initial numerical studies suggest that the presence of moderate volume fractions of microbubbles reduces the effective dielectric properties of the tumor by as much as 30%, potentially improving detection efficacy via differential imaging.

### 1. Introduction

Emerging microwave breast cancer detection techniques seek to exploit a large dielectric-properties contrast between malignant and normal breast tissues. Our recently-completed large-scale dielectric characterization study of human breast tissue samples conducted over the 0.5-20 GHz frequency range demonstrated that the dielectric-properties contrast between malignant and normal adipose-dominated breast tissues is as large as 10:1, while the dielectric-properties contrast between malignant and normal fibroglandular tissues is no more than approximately 10% [1]. Since the vast majority of breast tumors originate within fibroglandular breast tissue, our results suggest that the malignant lesion is a weakly scattering target within a high clutter environment. To address this challenging imaging scenario, we are assessing the feasibility of using dielectric or conducting micro- and nano-particles as contrast agents for enhancing the dielectric-properties contrast between the tumor and surrounding normal fibroglandular tissue. The specific particles we have chosen for this analysis are air-filled microbubbles, such as the ones used as ultrasound contrast agents, and metallic nanoparticles. Once introduced into the breast, the particles are assumed to accumulate in the malignancy via passive and/or active mechanisms [2]. The efficacy of tumor detection is expected to be enhanced via differential imaging of the breast. In this paper we present the results of our initial numerical studies of dielectric-properties contrast enhancement for the case of air-filled microbubble contrast agent particles. A comparison between experimental and numerical results is also presented.

### 2. Methodology

The accumulation of contrast agent particles in a breast tumor is modeled as a binary mixture consisting of a certain volume fraction (VF) of inclusions (microbubbles) in a background medium (malignant breast tissue). We implemented both a 2D quasi-static finite-element method (QS-FEM), as well as a 2D finite-difference time-domain (FDTD) approach. The advantages of the former method are that it is simple and fast. However, it does not account for the physical size of the inclusions, but simply assumes that the particles are much smaller than the wavelength of the electromagnetic wave in the mixture. Since size-related effects, such as skin depth, are particularly important for finite-conductivity inclusions, such as metallic nanoparticles, we conducted full-wave FDTD simulations to validate the QS-FEM technique and obtain supplemental information. Here we address the simpler case of air-filled microbubble inclusions, since the results for this case are not confounded by skin depth and percolation effects.

For both numerical approaches, the dielectric properties of the background medium in the computational domain [Figures 1(a) and 2(a)] were set to those of malignant breast tissue at 5 GHz ( $\epsilon_{r,b}=50.65$ ,  $\sigma_b=4.84$  S/m) [1]. The dielectric properties of the air-filled microbubbles were set to those of free space ( $\epsilon_{r,i}=1$ ,  $\sigma_i=0$  S/m). The randomly-positioned inclusions were allowed to touch, but not overlap. For simplicity, the particles did not intersect the edges of the computational domain. For every VF of inclusions (5, 10, and 20%), 100 geometries with random particle locations were generated and simulated in order to capture the effects of different inclusion distributions in the ensemble average of effective dielectric properties values. For every VF, an average effective dielectric constant and conductivity was computed.



## 2.1. QS-FEM approach

The 2D QS-FEM approach, based on [3], was implemented using the partial differential equation toolbox in Matlab. The QS-FEM solved Laplace's equation for the geometry and boundary conditions of Figure 1(a). Once the electrostatic potential  $\phi(\mathbf{r})$  was computed at every point  $\mathbf{r}$  in the computational domain, the stored and dissipated energies in the capacitor of Figure 1(a) (henceforth referred to as a complex stored energy) were found using  $W^* = 1/2 \epsilon_0 \int \epsilon^*(\mathbf{r}) [\nabla \phi(\mathbf{r})]^2 d^2 \mathbf{r}$ , where  $\epsilon^*(\mathbf{r}) = \epsilon'(\mathbf{r}) - j \sigma(\mathbf{r}) / (\omega \epsilon_0)$  is the complex permittivity at every point in the computational domain,  $\epsilon_0$  is the permittivity of free space,  $\omega$  is the angular frequency, and  $j = \sqrt{-1}$ . Assuming that the complex stored energy of the capacitor in Figure 1(a) is equivalent to that of Figure 1(b), the effective dielectric properties in 1(b) were found using  $\epsilon_{\text{eff}}^* = 2W^* / (\epsilon_0 \phi_0^2)$ .

The top plate of the capacitor in Figure 1(a) was held at a constant potential of  $\phi_0 = 1$  V, while the bottom plate was held at 0 V. In order to avoid fringing fields at the edges of the structure, Neumann boundary conditions were enforced on the left and right sides of the computational domain [Figure 1(a)]. The size of the computational domain was 100 by 100 units, while the radius of the inclusions was 2 units (the actual physical dimensions are irrelevant). A mesh conformal to the geometry was automatically generated by the solver.

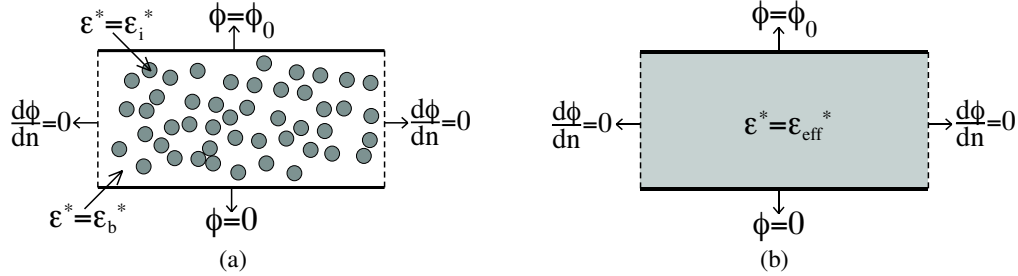


Figure 1. (a) Diagram of the geometry simulated using QS-FEM. (b) Effective medium formulation.  $\epsilon_b$ : background dielectric properties,  $\epsilon_i$ : inclusion dielectric properties,  $\epsilon_{\text{eff}}$ : effective dielectric properties.

## 2.2. FDTD approach

The 2D  $\text{TE}_z$  FDTD formulation used to simulate the TEM parallel-plate waveguide of Figure 2(a) was similar to that of [4]. The computed field components were  $E_x$ ,  $E_y$ , and  $H_z$ . This polarization was chosen to match the polarization of the QS-FEM simulations. The FDTD-computed  $E_y$  was recorded at 10 equally-spaced grid cells along the y-dimension of the waveguide at observation planes 1 and 2 [see Figure 2(a)]. Next, we calculated the attenuation ( $\alpha_s$ ) and propagation ( $\beta_s$ ) constants (assuming that the TEM mode in the mixture “slab” was not perturbed) using the FDTD-computed Fourier transforms of  $E_y$  at planes 1 and 2. Finally, we extracted the effective dielectric properties of the mixture from the attenuation and propagation constants. For every simulation, the effective dielectric properties calculated from data at the ten observation points along the y-dimension were averaged.

We used a modulated Gaussian source, with a center frequency of 5 GHz, and a  $1/e$  width of approximately 318 ns. Every simulation was run as long as necessary to sufficiently dissipate the energy inside the grid. The TEM mode was excited within the waveguide by assigning a current source to the  $E_y$  components along the source plane [see Figure 2(a)].

The plate separation was  $N_y = 50$  grid cells. The mixture “slab” of width  $N_x = 100$  grid cells was placed in the center of the waveguide, where  $L_1 = L_2 = 50$  grid cells. The waveguide was terminated with perfectly matched layer absorbing boundary conditions. The top and bottom walls of the waveguide were assumed to be perfect electric conductors. Since the microbubbles used as ultrasound contrast agents are approximately  $1\text{--}5\ \mu\text{m}$  in diameter, we set the diameter of the particles in the FDTD simulations to be  $5\ \mu\text{m}$ . In order to properly resolve the particles, the grid cell size was  $1.0\ \mu\text{m}$ . We used the Yu-Mitra technique [5] to compute the local dielectric properties for the electric-field components that cross the edges of the inclusions.



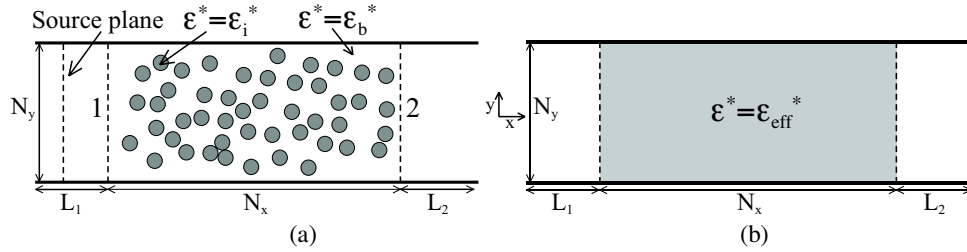


Figure 2. (a) Diagram of the parallel-plate waveguide simulated using FDTD. (b) Effective medium formulation.

### 2.3. Comparison with experimental studies

In addition to comparing the QS-FEM numerical results with FDTD, we compared our numerical results with experimental data for the cases of 5% and 10% by weight mixtures of air-filled microbubbles in ethylene glycol [6]. For this comparison, the dielectric properties of the background medium in the QS-FEM simulations were set to those of ethylene glycol at 5 GHz. The density of the glass-shell, air-filled microbubbles (average diameter: 18  $\mu\text{m}$ ) is 0.6 g/mL, so the VF of microbubbles in the 5% and 10% by weight mixtures were approximately 8.3% and 16.7%, respectively. Ethylene glycol was chosen as an inexpensive, readily available reference liquid, with dielectric properties representative of those of biological tissues. Immediately after mixing, the dielectric properties of the mixture were measured from 0.5 to 20 GHz using an open-ended coaxial probe [6]. The measurements were repeated five times for three different probe positions within the measurement beakers, and the dielectric properties recorded for all trials were averaged.

### 3. Comparison between QS-FEM and FDTD simulations

Table 1 shows the numerically computed effective dielectric properties, averaged over 100 iterations, of three different mixtures (VF=5%, 10%, and 20%) of microbubbles in a background medium representing malignant breast tissue. For every VF of inclusions, the variability in the effective dielectric properties across iterations is very small, no more than about 7%. In addition, we found excellent agreement between the QS-FEM-computed and FDTD-computed effective dielectric properties of the mixtures. In fact, for all three VFs investigated in this study, the QS-FEM-computed effective dielectric properties were within approximately 1% of the FDTD-computed effective dielectric properties, indicating that the simpler QS-FEM formulation is very accurate for modeling the dielectric-properties changes due to microbubble inclusions. Furthermore, we found that moderate VFs of microbubbles have noticeable effects on the effective dielectric properties of malignant breast tissue (Table 1). For example, a 20% VF of microbubbles resulted in an approximately 30% reduction in the effective dielectric properties of the tissue.

Table 1. Comparison between QS-FEM-computed and FDTD-computed effective dielectric properties of mixtures of air-filled microbubbles in breast tumor.

VF (%)	Effective dielectric constant at 5 GHz			Effective conductivity at 5 GHz (S/m)		
	QS-FEM	FDTD	% change	QS-FEM	FDTD	% change
0	50.65	50.65	--	4.84	4.84	--
5	46.09	45.87	-9	4.39	4.36	-10
10	41.76	41.81	-17	3.96	3.96	-18
20	34.46	34.16	-32	3.23	3.22	-33

### 4. Comparison between numerical and experimental studies

Figure 3 shows the effective dielectric properties of a 5% and 10% by weight mixture of microbubbles in ethylene glycol. The solid and dotted lines represent experimental data, while the symbols represent QS-FEM-computed effective dielectric properties at 5, 10, and 15 GHz. We found excellent agreement between the experimental and numerical results – the QS-FEM-computed results are within about 8.5% of the experimental results. This small discrepancy can be attributed to the simplified, 2D nature of the QS-FEM simulations and the uncertainties in the actual VF of inclusions in the mixtures and the exact dielectric properties of the microbubbles. The fact that the actual dielectric properties of the microbubbles are slightly higher than the

assumed value of free space and are spherical rather than cylindrical may explain why the QS-FEM-predicted decrease in the effective dielectric properties is somewhat larger than the experimentally measured decrease.

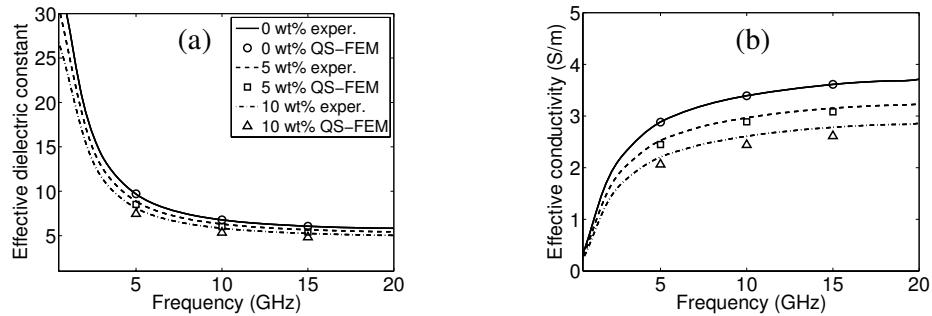


Figure 3. Experimentally-measured and QS-FEM computed effective (a) dielectric constant and (b) conductivity of mixtures consisting of 5% and 10% by weight air-filled microbubbles in ethylene glycol.

## 5. Conclusions

We have conducted numerical studies to investigate the effects of air-filled microbubbles on the dielectric properties of malignant breast tissue. We demonstrated that the QS-FEM technique accurately models the change in dielectric properties of a dielectric medium representing malignant breast tissue due to the presence of microbubbles. We found that a 5-20% VF of microbubbles can lower the dielectric properties of malignant tissue by as much as 30%. Through another research effort in our group, we have explored the impact of this dielectric properties reduction on microwave images generated for 3D anatomically realistic numerical breast phantoms using an inverse scattering algorithm. Results from those studies demonstrate the feasibility of tumor detection via differential (pre- and post-contrast-agent) imaging.

## 6. Acknowledgments

The authors thank Alireza Mashal for providing the experimental data. This work has been funded by the Department of Defense Breast Cancer Research Program under W81XWH-07-1-0629, the American Association of University Women Educational Foundation Selected Professions Engineering Dissertation Fellowship, and the National Science Foundation under a Graduate Research Fellowship.

## 7. References

- [1] M. Lazebnik, D. Popovic, L. McCartney, C. B. Watkins, M. J. Lindstrom, J. Harter, S. Sewall, T. Ogilvie, A. Magliocco, T. M. Breslin, W. Temple, D. Mew, J. H. Booske, M. Okoniewski, and S. C. Hagness, "A large-scale study of the ultrawideband microwave dielectric properties of normal, benign, and malignant breast tissues obtained from cancer surgeries," *Phys. Med. Biol.*, **52**, Oct. 2007, pp. 6093-6115.
- [2] I. Brigger, C. Dubernet, and P. Couvreur, "Nanoparticles in cancer therapy and diagnosis," *Adv. Drug Delivery Rev.*, **54**, 2002, pp. 631-651.
- [3] I. Krakovsky and V. Myroshnychenko, "Modeling dielectric properties of composites by finite-element method," *J. Appl. Phys.*, **92**, Dec. 20002, pp. 6743-6748.
- [4] O. Pekonen, K. Karkkainen, A. Sihvola, and K. Nikoskinen, "Numerical testing of dielectric mixing rules by FDTD method," *J. Electromagnetic Waves and Appl.*, **13**, 1999, pp. 67-87.
- [5] A. Taflov and S. C. Hagness, *Computational Electrodynamics: The Finite-Difference Time-Domain Method, Third Edition*, Boston, Artech House, 2005, pp. 426.
- [6] A. Mashal, J. H. Booske, and S. C. Hagness, "Towards contrast-enhanced microwave-induced thermoacoustic imaging of breast cancer: An experimental study of the effects of microbubbles on simple thermoacoustic targets," *Phys. Med. Biol.*, in preparation.

## **Characterization of the Dielectric and Heating Response of Carbon Nanotubes for Enhancing Microwave Detection and Treatment of Breast Cancer**

Alireza Mashal<sup>(1)</sup>, Earl Zastrow<sup>(1)</sup>, Pramod Avti<sup>(2)</sup>, Balaji Sitharaman<sup>(2)</sup>, John H. Booske<sup>(1)</sup>, and Susan C. Hagness<sup>(1)</sup>

(1) Electrical and Computer Engineering, University of Wisconsin, Madison, WI 53706

(2) Biomedical Engineering, Stony Brook University, Stony Brook, NY 11794

E-mail: amashal@wisc.edu, hagness@engr.wisc.edu

Microwave-frequency dielectric contrast between malignant and normal tissue in the breast serves as the physical basis for emerging microwave methods of detecting and treating breast cancer. Dielectric contrast leads to scattering of an illuminating microwave signal, which is exploited for breast cancer detection, and selective absorption of incident microwave power, which is exploited for localized hyperthermia treatment. The endogenous dielectric properties of breast tissue are dependent on the physiological type and state of the tissue (Lazebnik, et al., *Phys. Med. Bio.*, vol. 52, pp. 2637-2656 and 6093-6115, 2007). The effective dielectric properties may also be influenced by exogenous molecules introduced as contrast agents. We propose the use of single-walled carbon nanotubes (SWCNTs) as a diagnostic and therapeutic agent – an integrated “theranostic” nanoplatform – for both microwave detection and treatment of breast cancer (Mashal, et al., *IEEE TBME Letters*, accepted).

Here, we report the results of wideband (0.5-10 GHz) dielectric spectroscopy measurements and heating efficiency experiments (0.5-1 GHz) of SWCNT-water dispersions. Our study addresses the dielectric and thermal effect of biomedically relevant concentrations of SWCNTs over the frequency range that is of interest for microwave imaging and hyperthermia treatment of breast cancer.

We created the SWCNT dispersions by sonicating SWCNTs in a mixture of water and polyethylene glycol (PEG). FDA-approved PEG is used to non-covalently functionalize the SWCNTs, thereby ensuring that they remain biocompatible and well dispersed with no aggregation. We measured the dielectric properties using a precision open-ended coaxial probe technique (Popovic, et al., *IEEE Trans. Microwave Theory Tech.*, vol. 53, pp. 1713-1722, 2005). For a concentration of 2 mg/mL of SWCNTs, we saw an increase in permittivity of about 10% and an increase in conductivity of about 25% when compared to a pure DSPE-PEG solution across the 0.5 GHz to 3 GHz frequency range. Next we measured the impact of the SWCNTs on the heating response of a water-based mixture. A sample of the SWCNT dispersion was introduced into a 1.1-mm-inner-diameter glass capillary tube. The capillary tube was inserted through a small hole drilled into the center of a hardline coax and was illuminated with continuous microwave energy at discrete frequencies between 0.5 GHz to 1 GHz. A fluoroptic thermometer was used to record the temperature during each experiment. We observed the maximum final temperature increase by a factor of three at 0.5 GHz and a factor of two at 1 GHz. This increase in temperature scales approximately with the changes observed in the effective conductivities at these frequencies.

The enhanced dielectric properties and heating response suggest that SWCNTs are promising theranostic agents for microwave detection and thermal treatment of breast cancer. We have previously shown that the CNT-enhanced dielectric contrast greatly improves the sensitivity of microwave breast imaging (Shea, et al., ANTEM/URSI 2009). Here, we will highlight their impact on hyperthermia performance using computational electromagnetic and thermal simulations of numerical breast phantoms containing tumors targeted with CNTs.

# A Global EMC-FDTD Simulation Tool for High-Frequency Carrier Transport in Semiconductors

K. J. Willis, S. C. Hagness, and I. Knezevic

Electrical and Computer Engineering, University of Wisconsin-Madison, Madison, WI 53706, USA  
kjwillis@wisc.edu

Semiconductor material properties at terahertz (THz) and sub-THz frequencies cannot be well described by the models used at low frequencies. Bulk doped silicon has yet to be fully characterized at high frequencies, though some preliminary results have been reported [1]. Also, metals such as copper and aluminum have long demonstrated high-frequency conductivities significantly lower than predicted by the Drude model [2].

The Poisson solver incorporated into the typical Ensemble Monte Carlo (EMC) implementation assumes quasi-static fields. As the stimulating frequency approaches the THz regime, this assumption loses validity. Plasma frequencies and characteristic scattering rates of conductive media often fall within the THz frequency range. At high frequencies fully electrodynamic field calculations are required to ensure accuracy. The finite-difference time-domain (FDTD) method is a fully electrodynamic, highly accurate solver based on Maxwell's curl equations [3]. In the combined EMC-FDTD solver electric and magnetic fields from the FDTD solver influence EMC carrier motion. Microscopic currents resulting from carrier motion in the EMC correspondingly influence new FDTD-computed field values. A simulation flowchart is shown in Fig. 1.

Past research explored the combined EMC-FDTD solver in the context of AC device characterization [4]. The necessary consideration of a DC component requires continued Poisson's equation calculations in addition to FDTD, necessitating substantial computational resources and limiting solver applicability.

In this paper we examine the characteristics of the coupled EMC-FDTD solver in the context of high-frequency electromagnetic wave interactions with bulk doped silicon. The Poisson solver is not necessary for this calculation. We characterize the EMC-FDTD solver in terms of grid spacing, carrier ensemble size, and averaging technique.

We use two-dimensional (2D) computational domains for both FDTD and EMC. The FDTD domain boundaries are treated with perfectly-matched layer absorbing boundary conditions for conductive media, allowing finite-grid representation of an infinite space. The grid is defined in the  $x-y$  plane. We assume a  $TE_z$  mode for the electromagnetic wave; thus the FDTD grid comprises  $E_x$ ,  $E_y$ , and  $H_z$  field components. The simulation testbed is a semi-infinite half space of doped silicon (Regions B and C in Fig. 2) and a semi-infinite half space of air (Region A in Fig. 2). Region A is assigned a dielectric constant of 1 (and zero conductivity). A dielectric constant of 11.8 is assigned to Regions B

and C. Region C is filled with an assumed value for the continuous bulk conductivity of doped silicon,  $\sigma_{\text{bulk}}$ . Region B is in continuous interaction with the EMC; the conductivity terms in the FDTD update equations for  $E_x$  and  $E_y$  are removed from Region B, and interaction of FDTD fields and EMC currents is enforced. We use EMC reflecting boundary conditions at the vertical edges of Region B and periodic boundary conditions at the horizontal edges. An incident 0.5 THz plane wave is introduced via the analytic field propagation total-field scattered-field (AFP-TFSF) formulation [5].

Fig. 2 shows the 2D spatial distribution of the  $E_y$  phasor amplitude, extracted over several periods of electromagnetic wave oscillation. The field amplitude is attenuated as a function of depth in both Regions B and C; this macroscopic phenomenon is indicative of the skin effect in the coupled region. The effective linear-regime conductivity observed in Region B is calculated as  $\sigma_{\text{obs}} = \mathbb{R}\{\mathbf{E} \cdot \mathbf{J}^*\}/|\mathbf{E}|^2$ . Significant noise in  $|E_y|$ , resulting from electron motion, is visible in Region B. Noise levels in  $J_x$ ,  $J_y$ , and  $E_x$  in that region are similarly impacted by electron motion. Accurate calculation of  $\sigma_{\text{obs}}$  requires careful consideration of the effects of this noise.

Fig. 3 shows the observed noise of  $|E_y|$  in Region B for several configurations of grid cell size  $\Delta x$  and electron ensemble size  $N_e$ . Larger carrier ensembles show decreased noise, as expected. This improvement is dwarfed, however, by the improvements gained through increased grid cell size. In direct contrast to the EMC-Poisson solver, in which smaller grid cells improve accuracy, the EMC-FDTD solver produces cleaner results for larger grid cells. Instead of choosing several grid points per Debye length, as per Poisson solver accuracy and stability requirements, the EMC-FDTD grid cell size may be defined by the much less restrictive FDTD numerical dispersion requirements, which only require  $\Delta x$  to be smaller than roughly  $1/20^{\text{th}}$  of the smallest wavelength of interest.

Noise in the current density and field phasors may be reduced, and more accurate conductivity values calculated, through spatial averaging of extracted phasor quantities prior to the  $\sigma_{\text{obs}}$  calculation. Fig. 4 shows  $\sigma_{\text{obs}}$  plotted with respect to the size of the square region over which the phasor quantities are averaged. Noise is sufficiently reduced for large averaging region size to ensure convergence in  $\sigma_{\text{obs}}$ . Fig. 4 shows that larger ensembles also allow convergence in  $\sigma_{\text{obs}}$ , supporting the assertion that reduced phasor noise permits convergence  $\sigma_{\text{obs}}$ .

Finally, in Fig. 4 we examine the importance of impedance matching between the EMC-FDTD coupled

Region B and the surrounding pure-FDTD Region C (filled with continuous conductivity). These results show  $\sigma_{\text{obs}}$  to be insensitive to impedance mismatch between Regions B and C.

This preliminary work on a combined EMC-FDTD solver demonstrates the feasibility of a first-principles approach to predicting the effective conductivity of doped semiconductors at THz and sub-THz frequencies. Further work is needed to fully evaluate the performance of this approach.

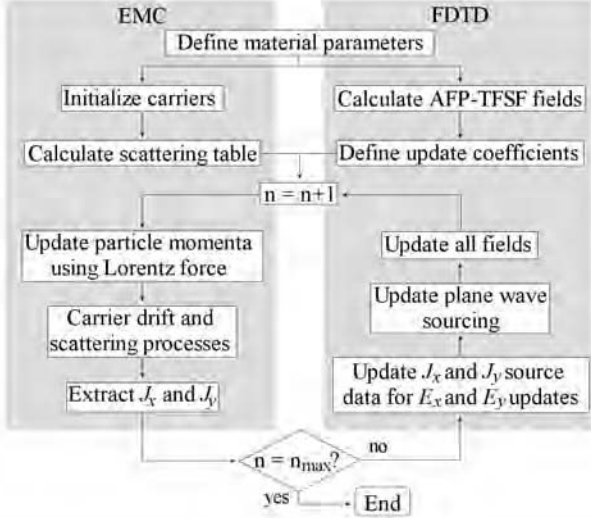


Figure 1: Simulation flowchart. The EMC and FDTD simulations are initialized independently. The time step counter is  $n$ . Currents and fields pass between the two simulation tools at every time step.

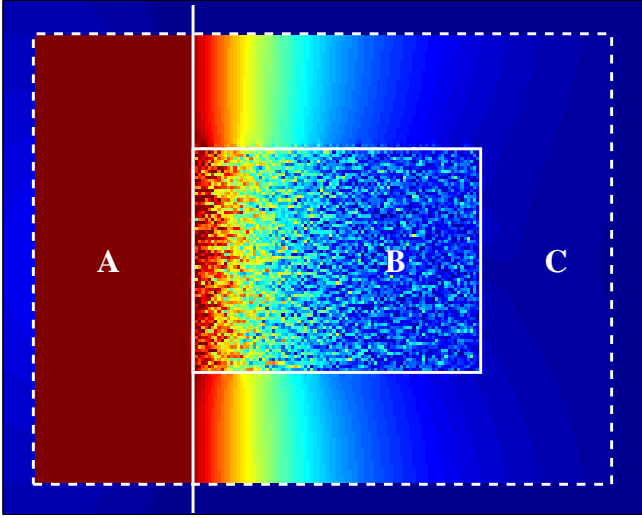


Figure 2: Amplitude decay of  $E_y$  field phasor extracted over several periods of electromagnetic wave oscillation. Air fills Region A, while Regions B and C are doped silicon. The material interface is indicated by the vertical solid white line. An incident plane wave is sourced from the TFSF boundary, shown by the dashed line. Region B is the EMC-FDTD coupled region, whose boundary is marked by a solid white box, and Region C is pure-FDTD doped silicon.

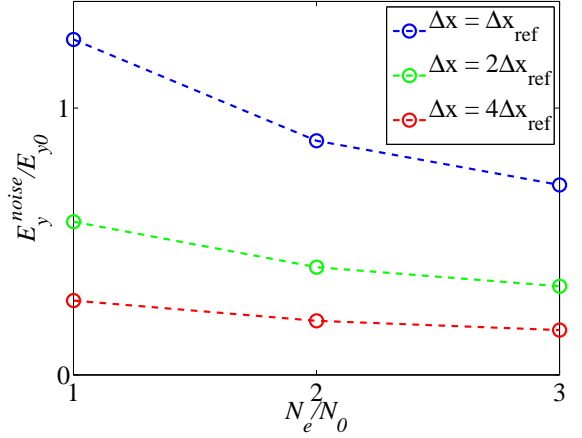


Figure 3: Average noise of  $E_y$  in the EMC-FDTD coupled region for several values of electron ensemble size and grid cell size, where  $\Delta x_{\text{ref}} \approx 400$  nm is a reference grid cell size.  $E_y^{\text{noise}}$  is calculated as  $\sqrt{\langle |E_y|^2 \rangle - |\langle E_y \rangle|^2}$  and is normalized by  $|E_y|$  at the material interface. Increasing the size of the ensemble reduces noise, as expected, but increasing the grid cell size produces a much larger improvement.

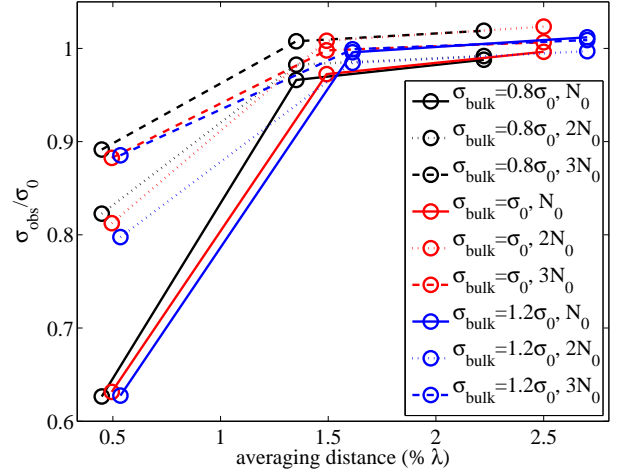


Figure 4: Observed conductivity with varied averaging region size, electron ensemble size, and surrounding bulk conductivity.  $N_0$  is a reference ensemble size, typically  $O(10^5)$ . Both electron ensemble size and averaging region size increase  $\sigma_{\text{obs}}$ .  $\sigma_{\text{obs}}$  is insensitive to impedance mismatch between Regions B and C.

- [1] T. I. Jeon and D. Grischkowsky, *Phys. Rev. Lett.* Vol. 78, pp. 1106–1109, 1997.
- [2] A. B. Pippard, *Proc. R. Soc. A-Math. Phys. Eng. Sci.* Vol. 191, pp. 385–399, 1947.
- [3] A. Taflov and S. C. Hagness, *Computational Electrodynamics: The Finite-Difference Time-Domain Method*, Artech House, 2nd ed., 2000.
- [4] J. S. Ayubi-Moak, S. M. Goodnick, and M. Saraniti, *J. Comput. Electron.* Vol. 5, pp. 415–418, 2006.
- [5] J. B. Schneider, *IEEE Trans. Antennas Propag.* Vol. 52, pp. 3280–3287, 2004.

# **Dielectric Characterization of Carbon Nanotube Contrast Agents for Microwave Breast Cancer Detection**

Alireza Mashal<sup>\*(1)</sup>, Balaji Sitharaman<sup>(2)</sup>, John H. Booske<sup>(1)</sup>, and Susan C. Hagness<sup>(1)</sup>

(1) Department of Electrical Engineering, University of Wisconsin, Madison, WI 53706

(2) Department of Biomedical Engineering, Stony Brook University,  
Stony Brook, NY 11794

E-mail: amashal@wisc.edu, booske@engr.wisc.edu, hagness@engr.wisc.edu

## **Abstract**

We are investigating the feasibility of single-walled carbon nanotubes (SWCNTs) as contrast agents for microwave breast cancer detection. We hypothesize that the accumulation of SWCNTs in a tumor will enhance the dielectric contrast between normal and malignant tissue and potentially improve the efficacy of microwave imaging techniques. As an initial step, we constructed tissue-mimicking phantom materials with varying concentrations of SWCNTs. We characterized their dielectric properties and estimated the pressure wave induced in the phantom materials under microwave illumination. At SWCNT concentrations of less than 0.5% by weight, we observed significant changes in both the relative permittivity and effective conductivity of these SWCNT/tissue-mimicking material mixtures. Our estimates suggest a similarly significant change in the thermoacoustic response relative to the phantom material mixtures without carbon nanotubes.

## **1. Introduction**

Microwave detection of breast cancer has been under intense investigation for the past decade because of its potential as a low cost, non-ionizing modality that offers 3D tomographic imaging capabilities. Until recently, work in this area has primarily focused on exploiting the intrinsic dielectric contrast between normal and malignant tissue. However, a published large-scale dielectric spectroscopy study conducted by the Universities of Wisconsin-Madison and Calgary has shown that while the contrast in the microwave-frequency dielectric properties between malignant tissues and healthy adipose-dominated tissues in the breast is as large as 10:1, the contrast between malignant and normal glandular/fibroconnective tissues in the breast is no more than about 10% [1]. Since most tumors originate in glandular tissue, these results suggest that solely exploiting the intrinsic dielectric contrast between normal and malignant tissue will result in a more challenging cancer detection scenario than previously thought.

We have recently initiated an investigation of exogenous contrast agents to determine how they affect the sensitivity of microwave imaging modalities. In [2, 3], we describe the dielectric contrast-enhancement effects of gas-filled microbubbles and metallic nanoparticles, while in [4] we describe the impact of microbubbles on 3D microwave tomographic breast imaging. Here we propose the use of single wall carbon nanotubes (SWCNTs) as a contrast agent for microwave imaging. Biocompatible carbon nanotubes are being broadly explored for a variety of diagnostic and therapeutic applications in medicine such as nanoscale biosensors, drug delivery for cancer treatment, novel biomaterials, and molecular imaging [5]. SWCNTs that accumulate in tumors via passive or active mechanisms could alter the effective complex permittivity of the tumor

when compared to a tumor in its pre-contrast stage. This change in dielectric properties can be exploited via differential imaging to improve sensitivity. In addition, the increase in effective conductivity could be advantageous in thermal therapy applications. To test the feasibility of these carbon nanotubes as a contrast agent for microwave applications, we characterize the dielectric properties of tissue mimicking (TM) materials mixed with various concentrations of SWCNTs. We then evaluate the impact of the dielectric contrast enhancement on microwave-induced thermoacoustic imaging by estimating the amplitude of the induced pressure wave in a thermoacoustic imaging system.

## 2. Materials and methods

Lazebnik *et al* [6] discusses the construction of TM materials that approximate the dielectric properties of a variety of human soft tissues over the microwave frequency range that spans 0.5 GHz to 20 GHz. The results reported in [1] show that a 10% oil-gelatin mixture adequately describes the microwave properties of malignant breast tissue. Therefore, for this study we constructed 10% oil-gelatin TM materials by following the procedure outlined in [6] and adding the step of introducing of SWCNTs. We mixed in the SWCNTs by first adding the indicated amount of SWCNTs to a 1% by weight mixture of Pluronic (F127) deionized water mixture. The SWCNTs we used had an outer diameter of 1-2 nm, length of 5-30  $\mu\text{m}$ , and purity of greater than 90% by weight. This mixture was then sonicated using a probe sonicator for twenty minutes at a 120 W power level. We made various concentrations (1 mg/mL, 2 mg/mL, and 3 mg/mL) of SWCNT in deionized water and substituted these mixtures for the pure deionized water in the TM recipe described in [6]. We poured the liquid oil-gelatin mixtures into small covered glass jars and allowed the mixture to gel unperturbed.

We characterized the dielectric properties of the mixtures using a wideband open-ended coaxial probe technique [7]. We positioned the tip of the probe against the surface of the TM mixture, being careful not to compress the gel excessively or puncture the surface as described in [6]. We made measurements on three different samples of each TM mixture and averaged the results.

## 3. Results and discussion

Figures 1(a) and (b) show the measured relative permittivity and effective conductivity of the pure TM material and the TM materials with three different SWCNT concentrations over a frequency range of 0.6 – 20 GHz. Each wideband curve represents the average of measurements on three samples of the given mixture and the vertical bars depict the deviation of the individual measurements from the average value. Table 1 summarizes this data at 3 GHz and quantifies the percent change in dielectric properties due to the introduction of the SWCNTs. Our results show that small increases in the concentration of SWCNTs lead to a significant increase in both the relative permittivity and effective conductivity of the TM material.

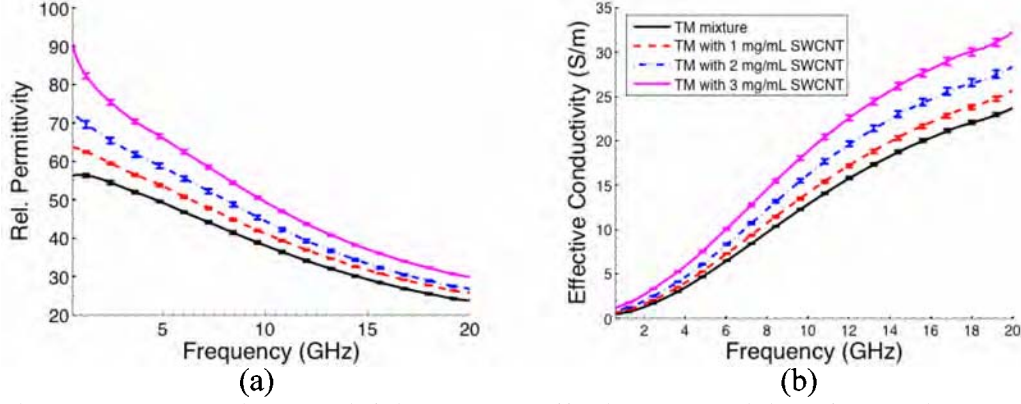


Figure 1. (a) Relative permittivity and (b) effective conductivity of TM mixture with varying concentrations of SWCNTs.

**Table 1.** Summary of dielectric spectroscopy data at 3 GHz.

Concentration of SWCNT in water	% by weight of SWCNTs	Average $\epsilon_r$ (3 GHz)	Average $\sigma$ (3 GHz)	Percent change $\epsilon_r$	Percent change $\sigma$
0	0	53.22	2.31 S/m	-	-
1 mg/mL	0.074 %	57.99	2.69 S/m	9 %	16 %
2 mg/mL	0.148 %	63.59	3.19 S/m	19 %	38 %
3 mg/mL	0.222 %	72.75	4.18 S/m	37 %	81 %

The changes in dielectric properties can lead to an improvement in the sensitivity of microwave imaging techniques, such as microwave-induced thermoacoustic imaging (MI-TAT). MI-TAT is a hybrid imaging modality that exploits dielectric-properties contrasts at microwave frequencies while creating images with ultrasound-quality resolution. In MI-TAT, the tissue is irradiated with a sub-microsecond electromagnetic pulse, which is then selectively absorbed by the higher-conductivity tissues and induces acoustic waves. These acoustic waves are detected by ultrasound transducers and processed for image reconstruction. We estimate the thermoacoustic response of a simple target by calculating the amplitude of the induced pressure wave assuming stress confinement, uniform heating, and neglecting thermal diffusion [8]:

$$\Delta P = B \cdot \beta_e \cdot \Delta T = B \cdot \beta_e \cdot \frac{SAR \cdot \tau}{C_p} = \frac{B \cdot \beta_e \cdot \tau}{C_p} \cdot \frac{\sigma |E|^2}{2\rho} \propto \sigma. \quad (1)$$

Here,  $\beta_e$  is the average volumetric expansion coefficient over small temperature ranges,  $B$  is the bulk modulus,  $\Delta T$  is the change in local temperature,  $\tau$  is the microwave pulse length,  $C_p$  is the specific heat. SAR is the specific absorption rate, defined as  $\sigma |E|^2 / 2\rho$ , where  $E$  is the electric field,  $\sigma$  is the effective electrical conductivity, and  $\rho$  is the mass density.

Equation 1 shows that the amplitude of the induced pressure wave is proportional to the effective conductivity of the tissue. If we assume that the carbon nanotubes do not significantly alter the thermomechanical properties of the tissue or the electric field intensity penetrating the tumor, then we can infer that the dielectric contrast provided by the SWCNT's correlate to a similar contrast in the thermoacoustic response and hence can aid the sensitivity of MI-TAT imaging.



## Conclusions

We characterized the dielectric properties of TM materials with varying concentrations of SWCNTs. Our results indicate that concentrations as small as 0.222% by weight of SWCNTs alter the relative permittivity of the TM phantom material by 37% and the effective conductivity by 81% when compared to the TM material without SWCNTs. Our estimates show a similar change in the induced pressure in a thermoacoustic imaging system. These changes in dielectric properties and thermoacoustic response at such low concentrations of carbon nanotubes are promising and suggest that SWCNTs have the potential to be effective as a contrast agent in microwave imaging modalities.

## Acknowledgements

The authors would like to thank Professor K. McMahon for granting access to her research group's sonicator. This work was supported by the Department of Defense Breast Cancer Research Program under grant W81XWH-07-1-0629, the National Institutes of Health under grant R01CA112398 awarded by the National Cancer Institute, and the Carol M. Baldwin Breast Cancer Research Fund.

## References

- [1] M. Lazebnik *et al*, "A large-scale study of the ultrawideband microwave dielectric properties of normal, benign, and malignant breast tissues obtained from cancer surgeries," *Phys. Med. Biol.*, vol. 52, pp. 6093-6115, Oct. 2007.
- [2] A. Mashal, J.H. Booske, and S.C. Hagness, "Towards contrast-enhanced microwave-induced thermoacoustic imaging of breast cancer: An experimental study of the effects of microbubbles on simple thermoacoustic targets," *Phys. Med. Biol.*, vol. 54, pp. 641-650, Feb. 2009.
- [3] M. Lazebnik, J. H. Booske, and S. C. Hagness, "Towards contrast-enhanced microwave detection and treatment of breast cancer: Dielectric characterization of microbubbles or metallic particles in lossy media," *IEEE Trans. Microw. Theory Tech.*, submitted (under review).
- [4] J. D. Shea, P. Kosmas, S. C. Hagness, and B. D. Van Veen, "Contrast-Enhanced Microwave Breast Imaging," in *ANTEM/URSI*, Banff, Alberta, Canada, Feb. 2009.
- [5] Y. Lin *et al*, "Advances towards bioapplications of carbon nanotubes," *J. Mater Chem.*, vol. 14, pp. 527 – 541, Feb. 2004.
- [6] M. Lazebnik, E.L. Madsen, G.R. Frank, and S.C. Hagness, "Tissue-mimicking phantom materials for narrowband and ultrawideband microwave applications," *Phys. Med. and Biol.*, vol. 50, pp. 4245-4258, Aug. 2005.
- [7] D. Popovic *et al*, "Precision open-ended coaxial probes for in vivo and ex vivo dielectric spectroscopy of biological tissues at microwave frequencies," *IEEE Trans. Microw. Theory Tech.*, vol. 53, pp. 1713-1722, May 2005.
- [8] L. V. Wang and H. I. Wu, *Biomedical Optics: Principles and Imaging*, 2005, New Jersey, Wiley, pp. 285.